

AD-A122 901

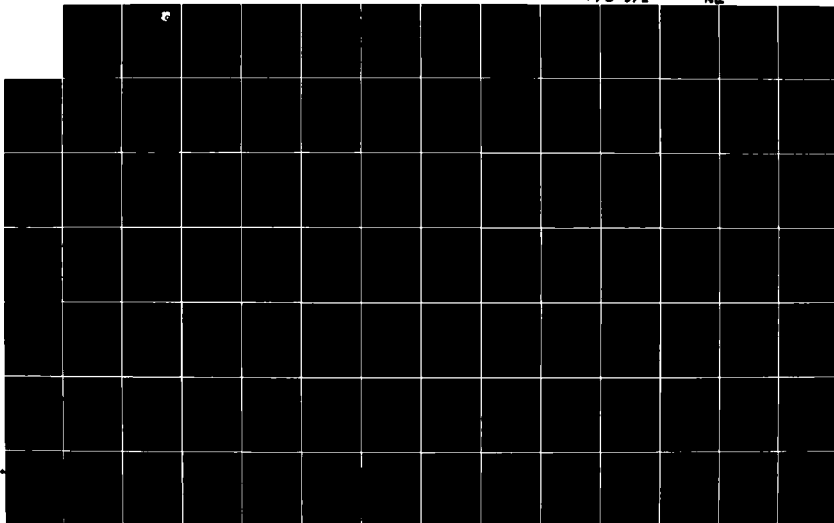
COMPUTER MODELING OF MILLIMETER-WAVE IMPATT DIODES ONE
OF A SERIES OF REP. (U) MICHIGAN UNIV ANN ARBOR
ELECTRON PHYSICS LAB R K FROELICH NOV 82 TR-158
AFWAL-TR-82-1107 F33615-81-K-1429

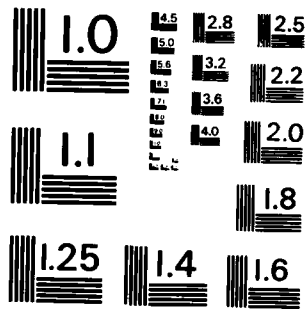
1/2

UNCLASSIFIED

F/G 9/2

NL





MICROCOPY RESOLUTION TEST CHART
NATIONAL BUREAU OF STANDARDS-1963-A

12

AD A122901

AFWAL-TR-82-1107



COMPUTER MODELING OF MILLIMETER-WAVE IMPATT DIODES

One of a series of reports on Millimeter-Wave Circuit Analysis and Synthesis

R. K. Froelich

Electron Physics Laboratory
Department of Electrical and Computer Engineering
The University of Michigan
Ann Arbor, Michigan 48109

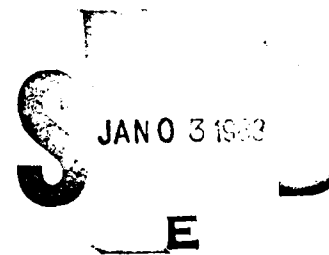
November 1982

Interim Report for Period March 1981 to May 1982

Approved for public release; distribution unlimited.

DISC FILE COPY

AVIONICS LABORATORY
AIR FORCE WRIGHT AERONAUTICAL LABORATORIES
AIR FORCE SYSTEMS COMMAND
WRIGHT-PATTERSON AIR FORCE BASE, OHIO 45433




82 01 03 024

NOTICE

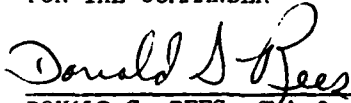
When Government drawings, specifications, or other data are used for any purpose other than in connection with a definitely related Government procurement operation, the United States Government thereby incurs no responsibility nor any obligation whatsoever; and the fact that the government may have formulated, furnished, or in any way supplied the said drawings, specifications, or other data, is not to be regarded by implication or otherwise as in any manner licensing the holder or any other person or corporation, or conveying any rights or permission to manufacture use, or sell any patented invention that may in any way be related thereto.

This report has been reviewed by the Office of Public Affairs (ASD/PA) and is releasable to the National Technical Information Service (NTIS). At NTIS, it will be available to the general public, including foreign nations.

This technical report has been reviewed and is approved for publication.


JON E. GRIGUS, CAPT, USAF
Project Engineer
Microwave Techniques &
Applications Gp

FOR THE COMMANDER


DONALD S. REES, Chief
Microwave Technology Branch
Avionics Laboratory

"If your address has changed, if you wish to be removed from our mailing list, or if the addressee is no longer employed by your organization please notify AFWAL/AADM, W-PAFB, OH 45433 to help us maintain a current mailing list."

Copies of this report should not be returned unless return is required by security considerations, contractual obligations, or notice on a specific document.

Unclassified

SECURITY CLASSIFICATION OF THIS PAGE (When Data Entered)

REPORT DOCUMENTATION PAGE		READ INSTRUCTIONS BEFORE COMPLETING FORM
1. REPORT NUMBER AFWAL-TR-82-1107	2. GOVT ACCESSION NO. AD-A122901	3. RECIPIENT'S CATALOG NUMBER
4. TITLE (and Subtitle) COMPUTER MODELING OF MILLIMETER-WAVE IMPATT DIODES	5. TYPE OF REPORT & PERIOD COVERED Interim Tech March 1981 to May 1982	
7. AUTHOR(s) Robert K. Froelich	6. PERFORMING ORG. REPORT NUMBER Tech. Report No. 158	
9. PERFORMING ORGANIZATION NAME AND ADDRESS Electron Physics Laboratory The University of Michigan Ann Arbor, MI 48109	8. CONTRACT OR GRANT NUMBER(s) F33615-81-K-1429	
11. CONTROLLING OFFICE NAME AND ADDRESS Avionics Laboratory (AFWAL/AADM-2) Air Force Wright Aeronautical Laboratories Wright-Patterson AFB, OH 45433	10. PROGRAM ELEMENT, PROJECT, TASK AREA & WORK UNIT NUMBERS 20020392	
14. MONITORING AGENCY NAME & ADDRESS (if different from Controlling Office)	12. REPORT DATE November 1982	
	13. NUMBER OF PAGES 159	
	15. SECURITY CLASS. (of this report) Unclassified	
	15a. DECLASSIFICATION/DOWNGRADING SCHEDULE N/A	
16. DISTRIBUTION STATEMENT (of this Report) Approved for public release; distribution unlimited.		
17. DISTRIBUTION STATEMENT (of the abstract entered in Block 20, if different from Report)		
18. SUPPLEMENTARY NOTES The findings in this report are not to be construed as an official Department of the Air Force position, unless so designated by other authorized documents.		
19. KEY WORDS (Continue on reverse side if necessary and identify by block number) Computer modeling Millimeter-wave IMPATT diodes Ionization rates Energy-dependent relaxation times Si diodes Submicron devices		
20. ABSTRACT (Continue on reverse side if necessary and identify by block number) A model of millimeter-wave Si IMPATTs has been developed which includes transient transport effects neglected in the conventional drift-diffusion model. The new model is based on principles of energy and momentum conservation. The model uses the first three velocity moments of the phase-space transport equation. Terms accounting for the effects of collisions incorporate energy dependent relaxation times and ionization rates. These functions of energy have been evaluated by requiring consistency with experimentally determined transport		

DD FORM 1473
1 JAN 73

Unclassified

SECURITY CLASSIFICATION OF THIS PAGE (When Data Entered)

Unclassified

SECURITY CLASSIFICATION OF THIS PAGE(When Data Entered)

20. Abstract (Contd.)

parameters. Stable, accurate and efficient finite-difference approximations to the transport equations were developed.

The simulation was used to identify and examine the influence of various transient transport phenomena, including velocity overshoot and undershoot, and the lag of energy with respect to electric field. The most important effect was found to be the energy lag. This delays carrier injection, thereby improving predicted device performance.

The results indicate that parasitics, rather than internal transport mechanisms, are dominant in determining the experimental performance attainable from millimeter-wave Si IMPATTs. The maximum frequency of operation of the IMPATT mode is subject to a fundamental limit associated with the energy relaxation time. This limit is approximately 500 GHz for Si IMPATTs.

Unclassified

SECURITY CLASSIFICATION OF THIS PAGE(When Data Entered)

FOREWORD

This report describes the simulation studies of millimeter-wave Si IMPATT devices carried out at the Electron Physics Laboratory, Department of Electrical and Computer Engineering, The University of Michigan, Ann Arbor, Michigan. The work was sponsored by the Air Force Systems Command, Avionics Laboratory, Wright-Patterson Air Force Base, Ohio under Contract No. F33615-81-K-1429.

The work reported herein was performed during the period March 1981 to May 1982 by Dr. Robert K. Froelich. The report was released by the author in May 1982.

The author wishes to thank Professor P. A. Blakey, his dissertation chairman, for his encouragement and guidance and Professor G. I. Haddad for his support and encouragement. He is also grateful to Dr. R. K. Mains, Mr. J. R. East and Dr. R. O. Grondin for their assistance in this investigation.

2025
COPY
INSPECTED

Accession For	
NTIS GRA&I	<input checked="checked" type="checkbox"/>
DTIC TAB	<input type="checkbox"/>
Unannounced	<input type="checkbox"/>
Justification	
By _____	
Distribution/ _____	
Availability Codes	
Dist	Avail and/or Special
A	

TABLE OF CONTENTS

	<u>Page</u>
CHAPTER I. INTRODUCTION	1
1.1 IMPATT Devices	1
1.1.1 Basic Operating Principles and Experimental State of the Art	1
1.1.2 Status of IMPATT Modeling	6
1.2 Models of Electron Transport in Semiconductors	7
1.2.1 A Hierarchy of Approaches	7
1.2.2 Applications to IMPATT Modeling	10
1.3 Outline of the Present Study	12
CHAPTER II. THE TRANSPORT MODEL	14
2.1 The Collisionless Transport Equations	14
2.1.1 Distribution-Independent Analysis	14
2.1.2 Dependence on the Velocity Distribution	20
2.2 Collision Terms	22
2.2.1 Physical Considerations	22
2.2.2 Forms of the Collision Terms	23
2.2.2.1 Same-Carrier Collisions	24
2.2.2.2 Opposite-Carrier Collisions	26
2.2.2.3 Electron-Hole Interactions	27
2.2.3 The Complete Transport Equations	28
2.2.4 Evaluations of Energy-Dependent Parameters	28
2.2.4.1 The Static Transport Equations	29
2.2.4.2 The Uniform Energy-Field Relationship	31
2.2.4.3 The Functions of Energy	34

	<u>Page</u>
2.3 Relationship to Other Models	34
2.3.1 The Energy Conserving Model	34
2.3.2 Energy and Momentum Balance Models	39
2.3.3 The Drift-Diffusion Limit	40
2.4 Summary and Conclusions	41
CHAPTER III. NUMERICAL METHODS FOR IMPATT DIODE SIMULATION	44
3.1 Normalizations	44
3.2 Finite-Difference Operators	47
3.2.1 Transport in the Limit of Short Time Step	50
3.2.1.1 Forward-Time, Upwind Drift Differences	50
3.2.1.2 Stability Analysis	51
3.2.1.3 Forward-Time, Centered Space Differences	55
3.2.1.4 The Lax Method	56
3.2.1.5 Three-Level Schemes	57
3.2.1.6 Other Schemes	59
3.2.2 Source and Relaxation Terms	59
3.2.2.1 Carrier Generation and Electric Field Terms	59
3.2.2.2 Relaxation Terms	60
3.2.2.3 Source and Relaxation Terms in Burstein's Method	64
3.3 Initial and Boundary Conditions	66
3.3.1 Initial Conditions	67
3.3.2 Spatial Boundary Conditions	67
3.3.3 The Device-Load Interaction	69
3.4 Conclusions	72
CHAPTER IV. SIMULATION OF MILLIMETER-WAVE IMPATT OPERATION	74
4.1 "Flat Field" Results	75
4.2 Comparisons Between Conventional and Energy and Momentum Conserving Results	85
4.3 Effects of Boundary Conditions	102
4.4 Sources of Energy Lag	104
4.5 Limitations on IMPATT Performance	123
4.6 Summary and Conclusions	127

	<u>Page</u>
CHAPTER V. SUMMARY, CONCLUSIONS, AND SUGGESTIONS FOR FURTHER RESEARCH	131
5.1 Summary and Conclusions	131
5.2 Suggestions for Further Research	135
APPENDIX A. MATERIAL PARAMETERS	139
LIST OF REFERENCES	141

LIST OF ILLUSTRATIONS

<u>Figure</u>		<u>Page</u>
1.1	Read Diode Structure, Field Distribution and Voltage and Current Waveforms. (Bauhahn ³)	3
1.2	Power and Frequency State of the Art for Various Semiconductor Devices. (Theoretical Results Parallel those of Scharfetter. ²⁹)	5
1.3	A Hierarchy of Models for Charge Transport in Semiconductors. (Blakey et al. ⁴²)	8
2.1	Electron Average Energy (Solid Curve) and Hole Average Energy (Dashed Curve) vs. Electric Field Strength Under Uniform Conditions.	35
2.2	Energy and Momentum Relaxation Times vs. Average Energy for Electrons (Solid Curves) and Holes (Dashed Curves) in Si at 500°K.	36
2.3	Ionization Rate vs. Average Energy for Electrons (Solid Curve) and Holes (Dashed Curve) in Si at 500°K.	37
2.4	Diffusion Coefficient vs. Electric Field Strength for Electrons (Solid Curve) and Holes (Dashed Curve) in Si at 500°K.	42
3.1	Numerical Error vs. Time Step Length for Various Forms of the Decay Equation. [$f(\Delta t)$: Exact; f_1 : First Order, Present Time; f_2 : Second Order, Present Time; f_3 : Advanced Time]	62
3.2	Circuit Configuration for Device-Load Interaction.	70
4.1	Doping Profiles for (a) 1 μm and (b) 0.3 μm Diodes with Spatially Constant Field.	76
4.2	Electric Field (Solid Lines) and Concentration, Current Density, Average Energy, and Average Velocity for Electrons (Minus Signs) and Holes (Plus Signs) in the 1- μm , Flat Field Diode Under Dc Conditions. ($J_{dc} = 10^4 \text{ A/cm}^2$)	77
4.3	Electric Field (Solid Lines) and Concentration, Current Density, Average Energy, and Average Velocity for Electrons (Minus Signs) and Holes (Plus Signs) in the 0.3- μm , Flat Field Diode Under Dc Conditions. ($J_{dc} = 10^4 \text{ A/cm}^2$)	78

<u>Figure</u>		<u>Page</u>
4.4	Electric Field (Solid Lines), Electron Energy (Minus Signs) and Hole Energy (Plus Signs) in the 1- μ m, Flat Field Device at Various Points in an RF Cycle. ($V_{RF} = 15$ V and $J_{dc} = 10^4$ A/cm ²)	81
4.5	Electric Field (Solid Lines), Electron Velocity (Minus Signs) and Hole Velocity (Plus Signs) in the 1- μ m, Flat Field Device at Various Points in an RF Cycle. ($V_{RF} = 15$ V and $J_{dc} = 10^4$ A/cm ²)	82
4.6	Electric Field (Solid Lines), Electron Energy (Minus Signs), Electron Velocity (Minus Signs), Hole Energy (Plus Signs) and Hole Velocity (Plus Signs) at the Center of the 1- μ m, Flat Field Device vs. RF Phase Angle. ($V_{RF} = 15$ V and $J_{dc} = 10^4$ A/cm ²)	84
4.7	Doping Profiles for (a) 1- μ m, (b) 0.5- μ m and (c) 0.3- μ m Double-Drift IMPATTs.	86
4.8	Energy and Momentum Conserving (Solid Line) and Conventional (Dashed Line) G-B Results for the 1- μ m Double-Drift Device. ($V_{RF} = 10$ V and $J_{dc} = 6 \times 10^4$ A/cm ²)	87
4.9	Energy and Momentum Conserving (Solid Line) and Conventional (Dashed Line) G-B Results for the 0.5- μ m Double-Drift Device. ($V_{RF} = 8$ V and $J_{dc} = 10^5$ A/cm ²)	88
4.10	Energy and Momentum Conserving (Solid Line) and Conventional (Dashed Line) G-B Results for the 0.3- μ m Double-Drift Device. ($V_{RF} = 6$ V and $J_{dc} = 1.5 \times 10^5$ A/cm ²)	89
4.11	Electric Field (Solid Lines), Electron Energy and Electron Velocity (Minus Signs) and Hole Energy and Hole Velocity (Plus Signs) in the 0.3- μ m Double-Drift Device Under Dc Conditions. ($J_{dc} = 1.5 \times 10^5$ A/cm ²)	92
4.12	Terminal Voltage, Injected Current, and Induced Current Waveforms for 0.3- μ m Double-Drift IMPATT. (a) Energy and Momentum Conserving Simulation and (b) Conventional Simulation. ($f = 300$ GHz, $V_{RF} = 10$ V and $J_{dc} = 1.5 \times 10^5$ A/cm ²)	94
4.13	Electric Field (Solid Lines); Electron Density, Electron Energy and Electron Velocity (Minus Signs); Hole Density, Hole Energy and Hole Velocity (Plus Signs) vs. Distance in the 0.3- μ m Double-Drift Device near Zero Degrees Phase in the RF Cycle Shown in Fig. 4.12.	95

<u>Figure</u>		<u>Page</u>
4.14	Electric Field (Solid Lines); Electron Density, Electron Energy, and Electron Velocity (Minus Signs); Hole Density, Hole Energy and Hole Velocity (Plus Signs) vs. Distance in the 0.3- μ m Double-Drift Device at 90 Degrees Phase in the RF Cycle Shown in Fig. 4.12.	96
4.15	Electric Field (Solid Lines); Electron Density, Electron Energy and Electron Velocity (Minus Signs); Hole Density, Hole Energy and Hole Velocity (Plus Signs) vs. Distance in the 0.3- μ m Double-Drift Device at 180 Degrees Phase in the RF Cycle Shown in Fig. 4.12.	97
4.16	Electric Field (Solid Lines); Electron Density, Electron Energy and Electron Velocity (Minus Signs); Hole Density, Hole Energy and Hole Velocity (Plus Signs) vs. Distance in the 0.3- μ m Double-Drift Device at 270 Degrees Phase in the RF Cycle Shown in Fig. 4.12.	98
4.17	Electric Field (Solid Lines), Electron Energy (Minus Signs), and Hole Energy (Plus Signs) vs. RF Phase Angle at Three Points Inside the 0.3- μ m Double-Drift Device. ($V_{RF} = 6$ V, $J_{dc} = 1.5 \times 10^5$ A/cm ² and $f = 200$ GHz)	100
4.18	Electric Field (Solid Lines), Electron Velocity (Minus Signs) and Hole Velocity (Plus Signs) vs. RF Phase Angle at Three Points Inside the 0.3- μ m Double-Drift Device. ($V_{RF} = 6$ V, $J_{dc} = 1.5 \times 10^5$ A/cm ² and $f = 200$ GHz)	101
4.19	Doping Profile of 0.3- μ m Double-Drift Device with Contact Regions.	103
4.20	Electric Field (Solid Lines); Electron Density, Electron Energy and Electron Velocity (Minus Signs); Hole Density, Hole Energy and Hole Velocity (Plus Signs) vs. Distance in the 0.3- μ m Double-Drift Device with Contacts at Zero Degrees Phase in the RF Cycle. ($V_{RF} = 6$ V, $J_{dc} = 1.5 \times 10^5$ A/cm ² and $f = 300$ GHz)	105
4.21	Electric Field (Solid Lines); Electron Density, Electron Energy and Electron Velocity (Minus Signs); Hole Density, Hole Energy and Hole Velocity (Plus Signs) vs. Distance in the 0.3- μ m Double-Drift Device with Contacts at 90 Degrees Phase in the RF Cycle. ($V_{RF} = 6$ V, $J_{dc} = 1.5 \times 10^5$ A/cm ² and $f = 300$ GHz)	106

<u>Figure</u>		<u>Page</u>
4.22	Electric Field (Solid Lines); Electron Density, Electron Energy and Electron Velocity (Minus Signs); Hole Density, Hole Energy and Hole Velocity (Plus Signs) vs. Distance in the 0.3- μ m Double-Drift Device with Contacts at 180 Degrees Phase in the RF Cycle. ($V_{RF} = 6$ V, $J_{dc} = 1.5 \times 10^5$ A/cm ² and $f = 300$ GHz)	107
4.23	Electric Field (Solid Lines); Electron Density, Electron Energy and Electron Velocity (Minus Signs); Hole Density, Hole Energy and Hole Velocity (Plus Signs) vs. Distance in the 0.3- μ m Double-Drift Device with Contacts at 270 Degrees Phase in the RF Cycle. ($V_{RF} = 6$ V, $J_{dc} = 1.5 \times 10^5$ A/cm ² and $f = 300$ GHz)	108
4.24	Electric Field (Solid Lines); Electron Density, Electron Energy and Electron Velocity (Minus Signs); Hole Density, Hole Energy and Hole Velocity (Plus Signs) vs. Distance in the 0.3- μ m Double-Drift Device Without Contacts at Zero Degrees Phase in the RF Cycle. ($V_{RF} = 6$ V, $J_{dc} = 1.5 \times 10^5$ A/cm ² and $f = 300$ GHz)	109
4.25	Electric Field (Solid Lines); Electron Density, Electron Energy and Electron Velocity (Minus Signs); Hole Density, Hole Energy and Hole Velocity (Plus Signs) vs. Distance in the 0.3- μ m Double-Drift Device Without Contacts at 90 Degrees Phase in the RF Cycle. ($V_{RF} = 6$ V, $J_{dc} = 1.5 \times 10^5$ A/cm ² and $f = 300$ GHz)	110
4.26	Electric Field (Solid Lines); Electron Density, Electron Energy and Electron Velocity (Minus Signs); Hole Density, Hole Energy and Hole Velocity (Plus Signs) vs. Distance in the 0.3- μ m Double-Drift Device Without Contacts at 180 Degrees Phase in the RF Cycle. ($V_{RF} = 6$ V, $J_{dc} = 1.5 \times 10^5$ A/cm ² and $f = 300$ GHz)	111
4.27	Electric Field (Solid Lines); Electron Density, Electron Energy and Electron Velocity (Minus Signs); Hole Density, Hole Energy and Hole Velocity (Plus Signs) vs. Distance in the 0.3- μ m Double-Drift Device Without Contacts at 270 Degrees Phase in the RF Cycle. ($V_{RF} = 6$ V, $J_{dc} = 1.5 \times 10^5$ A/cm ² and $f = 300$ GHz)	112

<u>Figure</u>		<u>Page</u>
4.28	Electric Field (Solid Lines), Electron Energy (Minus Signs) and Hole Energy (Plus Signs) Under "Hot" Boundary Conditions vs. Distance in the 0.3- μ m Double-Drift Device at Various Points in the RF Cycle. ($V_{RF} = 6$ V, $J_{dc} = 1.5 \times 10^5$ A/cm ² and $f = 300$ GHz)	114
4.29	Electric Field (Solid Lines), Electron Velocity (Minus Signs) and Hole Velocity (Plus Signs) Under "Hot" Boundary Conditions vs. Distance in the 0.3- μ m Double-Drift Device at Various Points in the RF Cycle. ($V_{RF} = 6$ V, $J_{dc} = 1.5 \times 10^5$ A/cm ² and $f = 300$ GHz)	115
4.30	Electric Field (Solid Lines), Electron Energy (Minus Signs) and Hole Energy (Plus Signs) Without Opposite-Carrier Cooling vs. Distance in the 0.3- μ m Double-Drift Device at Various Points in the RF Cycle. ($V_{RF} = 6$ V, $J_{dc} = 1.5 \times 10^5$ A/cm ² and $f = 300$ GHz)	117
4.31	Electric Field (Solid Lines), Electron Velocity (Minus Signs) and Hole Velocity (Plus Signs) Without Opposite-Carrier Cooling vs. Distance in the 0.3- μ m Double-Drift Device at Various Points in the RF Cycle. ($V_{RF} = 6$ V, $J_{dc} = 1.5 \times 10^5$ A/cm ² and $f = 300$ GHz)	118
4.32	G-B Characteristics for the 1- μ m, Double-Drift Device with (Solid Line) and Without (Dashed Line) Opposite-Carrier Cooling. ($V_{RF} = 10$ V and $J_{dc} = 6 \times 10^5$ A/cm ²)	119
4.33	G-B Characteristics for the 0.3- μ m Double-Drift Device with (Solid Line) and Without (Dashed Line) Opposite-Carrier Cooling. ($V_{RF} = 6$ V and $J_{dc} = 1.5 \times 10^5$ A/cm ²)	120
4.34	Normalized Amplitude and Phase of the Carrier Energy Response vs. Frequency.	125
4.35	"Intrinsic" Negative Resistance (Dashed Line) and Efficiency in the Presence of Various Values of Series Resistance (Solid Lines) vs. RF Amplitude for the 0.3- μ m Double-Drift Device. ($f = 300$ GHz and $J_{dc} = 1.5 \times 10^5$ A/cm ²)	128

LIST OF TABLES

<u>Table</u>		<u>Page</u>
3.1	Normalizations for Finite-Difference Forms of the Transport Equations.	48
4.1	Sample Results from Large-Signal Simulation.	90
A.1	Static Ionization Rates. ⁸⁴	139
A.2	Static Drift Velocity. ³	139
A.3	Other Parameters.	140

LIST OF SYMBOLS

A, B	Normalizing constants in the carrier velocity distribution function.
C	Dc blocking capacitance in the external circuit for device-load interaction, F/m^2 .
C_d	Diode depletion capacitance, F/m^2 .
c	Carrier speed in distribution function, m/s .
c_c	Carrier speed at the threshold for impact ionization, m/s .
D	Diffusion coefficient, m^2/s .
D_n	Numerical diffusion coefficient, m^2/s .
\vec{E}, E	Vector and scalar electric field, V/m .
\underline{E}	Normalized electric field.
E_o	Amplitude of sinusoidally varying electric field, V/m .
\vec{F}	Force vector, J/m .
F	Field function in carrier velocity distribution, J .
\vec{f}_j^t	Vector solution function.
\vec{f}_m	Fourier component of vector solution function.
G	Carrier generation rate, $m^{-3}s^{-1}$.
G_t	Thermal generation rate, $m^{-3}s^{-1}$.
$[G_m]$	Amplification matrix.
J	Current density, A/m^2 .
J_{dc}	Dc current density, A/m^2 .
J_n	Electron current density, A/m^2 .
J_p	Particle current density, A/m^2 .
J_{sat}	Reverse saturation current density, A/m^2 .

L	Device length, m.
L_d	Debye length, m.
M	Total number of space mesh points.
m^*	Effective mass, kg.
N	Doping density, m^{-3} .
$N(\bar{r}, \bar{v}, t)$	Velocity distribution function.
N_a	Acceptor density, m^{-3} .
N_d	Donor density, m^{-3} .
N_i	Ionized impurity density, m^{-3} .
n	Electron density, m^{-3} .
\bar{n}	Normalized electron concentration.
n_b	Boundary concentration.
$[P]$	Pressure tensor.
p	Hole concentration, m^{-3} .
\bar{p}	Normalized hole concentration.
\bar{q}	Heat flow vector.
R	Series resistance.
$[R]$	Relaxation matrix.
S	Source term in decay equation.
\bar{S}	Vector source term in Lax-Wendroff scheme.
T_c	Carrier temperature, °K.
\bar{u}, u	Normalized average velocity.
V_c	Dc blocking capacitance voltage, V.
V_d	Diode voltage, V.
V_{RF}	RF voltage amplitude, V.
\bar{v}, v	Vector and scalar velocity, m/s.
\bar{v}'	Departure from average velocity, m/s.

v_b	Boundary velocity, m/s.
v_d	Static drift velocity, m/s.
v_{sat}	Saturated drift velocity, m/s.
W	Average energy, J.
\bar{w}	Normalized average energy.
w_b	Boundary energy, J.
w_o	Thermal energy, J.
α, β	Ionization rate, s^{-1} .
α^*, β^*	Ionization rate, m^{-1} .
$\bar{\alpha}, \bar{\beta}$	Normalized ionization rate.
δ_c	Phase-space collision operator.
δ_t	Time finite-difference operator.
δ_x	Space finite-difference operator.
ϵ	Dielectric constant, F/m.
λ	Mean free path, m.
λ	Eigenvalue.
μ	Mobility, $m^2/V \cdot s$.
ξ	Numerical error.
τ	Relaxation time, s.
τ_v	Velocity relaxation time, s.
τ_w	Energy relaxation time, s.
$\bar{\Phi}$	Vector difference function in Lax-Wendroff scheme.

CHAPTER I. INTRODUCTION

The work presented in this thesis is concerned with modeling of millimeter-wave impact avalanche transit-time (IMPATT) diodes. The IMPATT is currently the most important semiconductor device for generation and amplification of power in the millimeter-wave frequency range. Difficulties arise in the modeling of these devices because of their submicron dimensions and high operating frequencies. Device models based on the well known "drift and diffusion" description of electron and hole transport are not expected to always be applicable for such small dimensions and high frequencies, so it is necessary to have more detailed models, both to establish the circumstances under which the drift and diffusion approximation fails and to model devices to which drift and diffusion based analyses cannot be applied. This thesis describes the development of a more general transport model, the development of a computer simulation based on the model, and the results obtained using the simulation.

This introductory chapter consists of three sections. The first two establish the context of the present work by providing reviews of the principles and performance capabilities of IMPATT diodes and of approaches to modeling charge transport in semiconductors. The third section describes the organization of the remainder of the thesis.

1.1 IMPATT Devices

1.1.1 Basic Operating Principles and Experimental State of the Art. The use of carrier transit-time effects to produce negative resistance in a semiconductor device was first proposed by Shockley

in 1954.¹ In 1958, Read² presented an analysis of a diode structure in which use of transit-time effects would be combined with carrier injection by impact ionization. The fundamental characteristics of Read-type device operation can be understood by considering the operation of an idealized device, whose doping and dc electric field profiles are shown in Fig. 1.1.³ The figure also shows a sinusoidal RF terminal voltage and the idealized forms of the injected and induced current wave forms which result when the magnitude of the dc bias voltage is just below that required for reverse breakdown.

The doping profile is chosen so that under reverse bias a narrow "ionization" region of high field exists near the p-n junction. At the beginning of the RF cycle, the field in this region is slightly below threshold for avalanche breakdown by impact ionization. As terminal voltage increases, the threshold is passed, and the number of carriers in the ionization region begins to increase. This continues until the midpoint of the cycle when the field in the ionization region drops once again below threshold. The electrons generated in the ionization region are injected into the lower-field "drift" region, where, if the field is strong enough, they travel at an approximately constant velocity. If the length of the drift region is such that the drift transit time is half the RF period, the motion of the electrons induces a flow of current in the diode terminals which is approximately 180 degrees out of phase with the terminal voltage, giving rise to negative resistance. As the cycle ends, the drifting electrons are collected by the right-hand contact, and the process repeats. All devices which operate by this combination of injection by impact ionization and drift across a depleted region are known as IMPATT

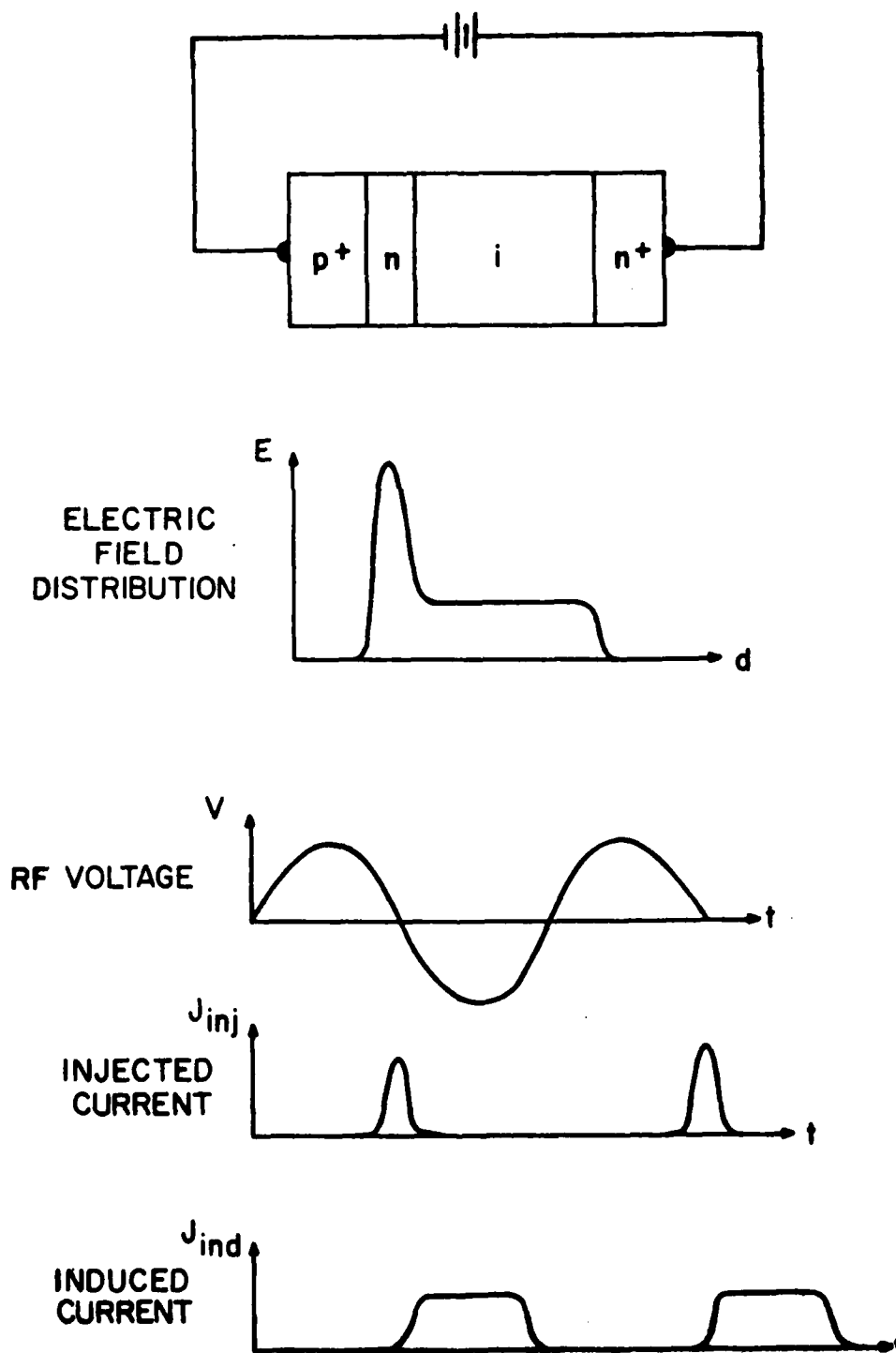


FIG. 1.1 READ DIODE STRUCTURE, FIELD DISTRIBUTION AND VOLTAGE
AND CURRENT WAVEFORMS. (BAUHAHN³)

diodes, though their structure may differ considerably from that shown in Fig. 1.1.

In the operation of a real IMPATT device, various departures from the ideal behavior summarized in Fig. 1.1 occur. The space charge of the carriers which accumulate during the first part of the RF cycle depresses the field in the ionization region so that injection occurs before the midpoint of the cycle. This reduces the lag between terminal voltage and current and degrades the device efficiency. Other effects which lower efficiency include diffusive spreading of the injected carrier pulse, impact ionization in the drift region, and carrier drift at nonsaturated velocities.

Because of difficulties with device fabrication, IMPATT mode operation was not realized until 1965, when Lee et al.⁴ succeeded in obtaining the first oscillations from a Read-type diode. About the same time, Johnson et al.⁵ obtained oscillations from a simpler p-n diode structure. IMPATT fabrication and circuit technology have developed steadily since then, and today IMPATTs are widely used as sources and amplifiers in low and medium power microwave and millimeter-wave systems. Silicon IMPATTs in particular are presently the most important solid state power source at high microwave and millimeter-wave frequencies.⁶ The experimental power and frequency state of the art for a variety of semiconductor devices is shown in Fig. 1.2.⁷⁻²⁹ This shows that Si IMPATTs are currently the highest power semiconductor devices for millimeter-wave power generation, and that their useful frequency range extends to several hundred gigahertz.

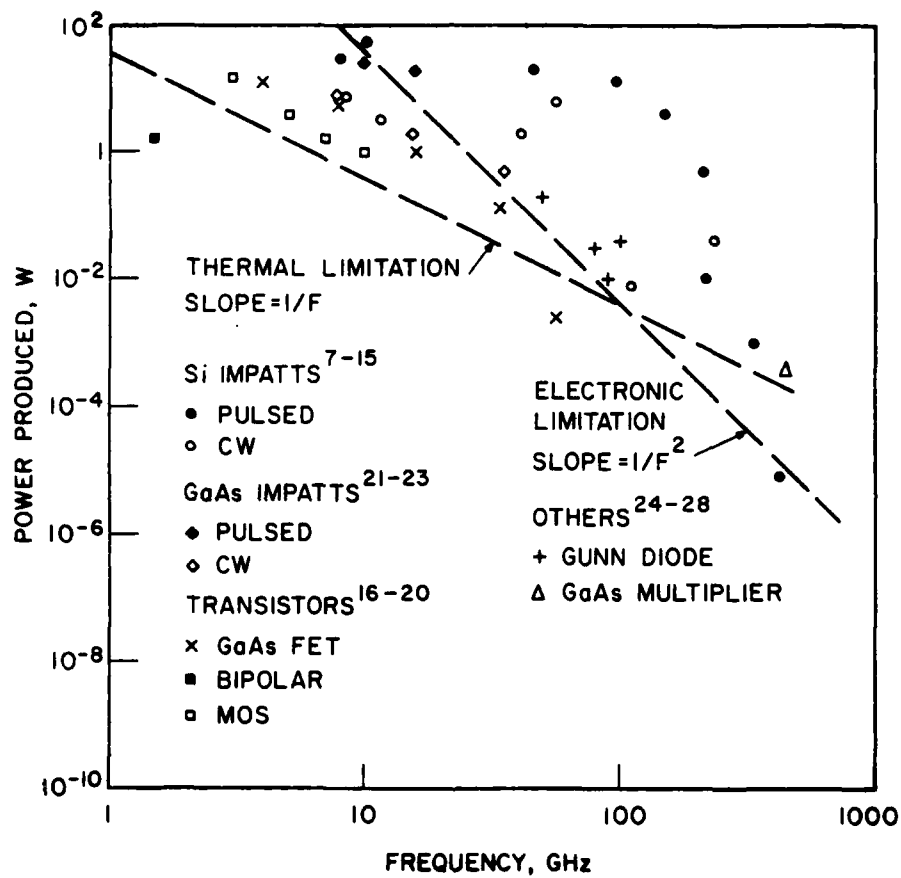


FIG. 1.2 POWER AND FREQUENCY STATE OF THE ART FOR VARIOUS SEMICONDUCTOR DEVICES. (THEORETICAL RESULTS PARALLEL THOSE OF SCHARFETTER.²⁹)

1.1.2 Status of IMPATT Modeling. IMPATT operation is inherently nonlinear, so detailed modeling of large-signal operation requires the use of numerical methods. Most IMPATT models to date have been intended for microwave devices and have been based on the conventional drift and diffusion description of carrier transport. In his original paper, Read² assumed saturated drift, with equal velocities and ionization rates for electrons and holes, and ignored diffusion. Other workers have developed small-signal models which allowed for unequal saturated velocities and ionization rates,³⁰ arbitrary doping profiles,³¹ field-dependent velocities,³² and diffusion.³³ Gilden and Hines³⁴ derived a useful small-signal equivalent circuit for Read-type IMPATTs, showing the tuning effects of the dc bias current. Evans and Haddad³⁵ developed the first closed-form expression for IMPATT large-signal impedance, using the assumption of a small phase angle associated with the drift transit time. This assumption, together with that of saturated drift, was removed in a large-signal model developed by Greiling and Haddad.³⁶ A well known finite-difference simulation based on a comparatively complete version of the drift-diffusion model was developed by Scharfetter and Gummel.³⁷ Subsequent workers have greatly improved the efficiency of finite-difference simulations based on the drift-diffusion model, and have reached a better understanding of the numerical diffusion which is associated with finite-difference schemes.^{3,38}

A few attempts have been made to develop IMPATT models which account for additional physical effects.³⁹⁻⁴¹ It will be shown that none of these represents a self-consistent treatment using a transport model better than conventional drift and diffusion.

Development of such a model is one focus of the present work, and a brief review of the spectrum of possible transport models will therefore now be given to establish a context for the work described in subsequent chapters.

1.2 Models of Electron Transport in Semiconductors

1.2.1 A Hierarchy of Approaches. The range of treatments of electron transport in semiconductors is conveniently described with reference to the hierarchy of approaches shown in Fig. 1.3.⁴² Electron transport in semiconductors is fundamentally quantum mechanical in nature (because the deBroglie wavelength of electrons is not small with respect to interatomic spacings), but can often be modeled using the quasi-free-particle (QFP) approximation shown in the center of the figure. In the QFP approximation, individual electrons are treated as classical particles with effective mass supplied by band theory. The concept of the hole is used to describe charge transport due to empty states in the valence band. The approximation is based on the assumption that collisions and acceleration due to externally applied electric fields can be treated as perturbations to the band structure description of the perfect lattice. This is generally true if the field is not so large as to invalidate the use of Bloch functions for the electron states, and if characteristic distances other than interatomic spacings are large compared to the size of an electron wave packet.⁴³ Once the band structure and scattering rates are established, QFP modeling of carrier transport can be accomplished by use of Monte Carlo or Rees iterative⁴⁴ techniques to solve the phase-space transport equation⁴⁵ with the appropriate collision term. However, such methods are generally too expensive for routine application

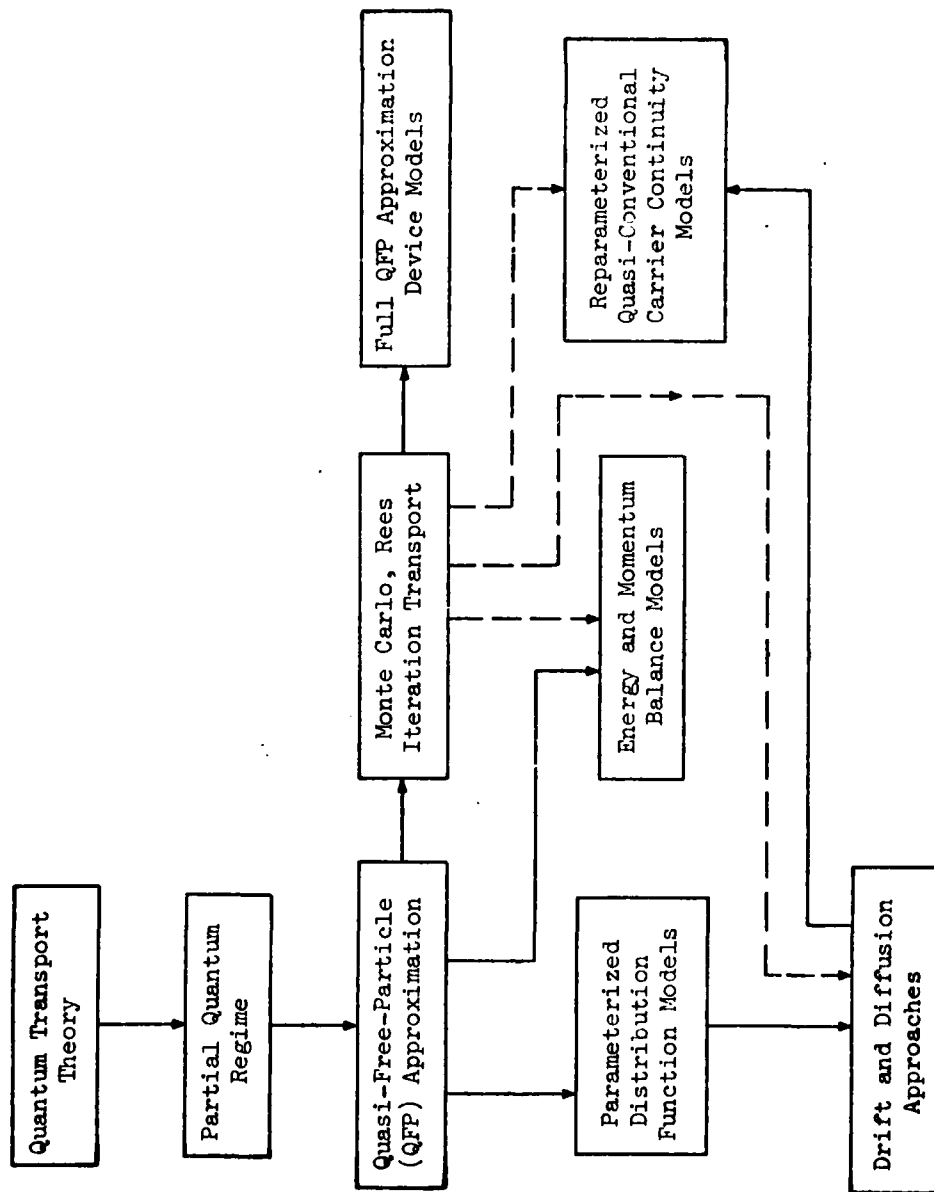


FIG. 1.3 A HIERARCHY OF MODELS FOR CHARGE TRANSPORT IN SEMICONDUCTORS. (BLAKEY ET AL.^{1,2})

to time domain simulation of devices, although they are used extensively for modeling carrier transport phenomena.

When certain simplifications are made in order to produce more economical device simulations, sub-QFP models result. Instead of working in terms of individual carriers or the exact form of the distribution function, these models use approximate descriptions of the distribution function. The distribution may be assumed to be in some parameterized form, such as displaced Maxwellian or a truncated series of Legendre polynomials, after which equations for the unknown parameters can be found from the phase-space transport equation. Alternatively, Monte Carlo data can be used to evaluate the phase-space collision term directly, and the results used in simple energy and momentum balance relations. This latter approach requires no assumptions about the form of the velocity distribution, but intuitively chosen balance relations are in fact inconsistent with the phase-space equation in spatially inhomogeneous situations.

The transport picture can be further simplified by assuming that the velocity distribution is always in equilibrium with the local electric field. These will be referred to as "static" conditions elsewhere in the thesis. The assumption is valid if the change in field strength seen by moving carriers is small during the time required to reach equilibrium. In this "static" approximation, carrier motion is commonly described using the conventional drift-diffusion equation with field-dependent drift velocity (or mobility), diffusion coefficients, and ionization rates. In some situations where the static model is almost appropriate for describing carrier transport, additional effects can be accommodated by adding extra transport parameters. A

"reparameterized" model has been used, for example, in dead space modeling of the impact ionization process.⁴⁶

Above the QFP approximation in Fig. 1.3 are the partial and full quantum regimes. In the partial quantum regime, the QFP approximation is substantially valid, but additional quantum effects, such as band-to-band tunneling or size quantization in one spatial dimension, are imposed on the basic framework. When characteristic dimension becomes extremely small, full quantum treatment of transport becomes necessary. This is still primarily the realm of the theoretical physicist.

1.2.2 Applications to IMPATT Modeling. The preceeding discussion illuminates why the applicability of the static drift-diffusion model to IMPATT modeling becomes suspect in the case of devices operating at millimeter-wave frequencies. The drift-diffusion model assumes equilibrium between the carrier velocity distributions and local electric field, but in millimeter-wave IMPATTs such equilibrium frequently may not exist because it is possible for carriers in these devices to experience significant changes in field strength during the time required to reach equilibrium. There are two main reasons why departures from equilibrium will be more significant at millimeter-wave frequencies than at microwave frequencies. First, design length decreases, and doping levels increase with frequency, so that drifting carriers travel through steeper gradients of the field strength in millimeter-wave devices than in microwave devices. This will affect even the dc behavior. Second, the maximum rate of change of terminal voltage, hence of internal field strength, tends to increase with frequency, though this tendency is offset somewhat by the decrease in RF amplitude which comes with decreasing device length.

Use of a full QFP model would give full knowledge of the carrier velocity distributions at all times. As was noted, however, such models are generally expensive when applied to simulation of devices. The reason for this is that they keep track of excessive information: the position and velocity of each individual carrier. Much of this information is not of first-order importance to a device simulation, since, for the purpose of determining device terminal currents and voltages, only the spatial distributions of carrier concentration and average velocity are required.

One attractive approach to filling the need for a nonstatic model for millimeter-wave IMPATTs is the method of conservation of energy and momentum, which falls in the sub-QFP regime of the hierarchy shown in Fig. 1.3. This method is not based on the static assumption of carrier field equilibrium and is much more economical for device simulation than full QFP methods. A presentation of the equations of energy and momentum conservation in transport in semiconductors, together with an extensive discussion of their relationship to various lower order models, has been given by Blotekjaer.⁴⁷

The nature of the energy and momentum conserving model for carrier transport can be briefly described as follows. The model consists of Poisson's equation for the electric field gradient, together with transport equations for three quantities as functions of space and time: carrier concentration, average momentum, and average energy. The first two quantities are required for determining device terminal behavior. The momentum equation keeps track of the various contributions to the momentum of the aggregate of carriers, such as gains due to acceleration by the field and losses due to

collisions. This means that the average carrier velocity is not a static function of field. The third quantity, average energy, is not required for calculating device voltages and currents, but gives the width of the velocity distribution, which affects the rate of carrier diffusion and, to a first approximation, determines the rates of collisions which affect momentum and determines the rate of impact ionization.

Concentration, average velocity, and average energy are proportional to the zeroth, first, and second moments of the velocity distribution. In the QFP approximation, the distribution is governed by the phase-space transport equation, so the carrier, momentum, and energy transport equations required under the energy and momentum conserving model can be obtained by taking the first three velocity moments of the phase-space equation. Using the resulting transport equations in the energy and momentum conserving model guarantees that it will be consistent with the phase-space equation to second order in the velocity coordinate.

1.3 Outline of the Present Study

The goals of this study are to apply the principles of energy and momentum conservation to simulation of millimeter-wave Si IMPATT diodes, to produce a computer simulation embodying the principles, to use the simulation to examine device behavior under dc and large-signal conditions, and, by comparison with results obtained using a conventional simulation, to establish the limits of applicability of drift-diffusion simulation.

The organization of the thesis is as follows. Chapter II develops energy and momentum conserving transport equations appropriate for carriers in Si. Chapter III examines numerical methods based on finite-difference approximation of the transport equations derived in Chapter II. A stable, accurate, and efficient numerical procedure for their solution is developed. Chapter IV presents results from computer simulation of millimeter-wave Si IMPATT diodes. Results from the new simulation are compared with results obtained using a conventional drift-diffusion simulation for a variety of device lengths and operating frequencies, and reasons for the observed differences are discussed. The effects of various energy boundary conditions and of realistic contact regions are also examined. Chapter V contains discussion, conclusions, and suggestions for further research.

CHAPTER II. THE TRANSPORT MODEL

This chapter describes the energy and momentum conserving transport model which has been developed to provide a better description of carrier transport in Si IMPATT diodes than that provided by the conventional drift-diffusion model. The contents of the chapter are as follows. Section 1 presents a derivation of the collisionless forms of the carrier, energy, and momentum transport equations, and discusses the physical interpretations of their various terms. In Section 2, functional forms and numerical values are obtained for terms describing the effects of collision processes. Section 3 discusses the differences between the resulting model and other nonstatic IMPATT models, and also shows how, under certain conditions, the model limits to the conventional one. Section 4 is a general discussion and summary of the chapter.

2.1 The Collisionless Transport Equations

This section develops collisionless transport equations for carriers, carrier energy and carrier momentum in Si.* The development presented here and throughout much of the remainder of this chapter is given in terms of electron transport only. The extensions to hole transport are readily apparent.

2.1.1 Distribution-Independent Analysis. The starting point for building the energy and momentum conserving transport model is the quasi-free-particle approximation described in Chapter I.

*Much of the material in this section is based on the treatment of Duderstadt and Martin.⁴⁵

The approximation allows carriers to be treated as classical particles with effective masses and collision rates determined from the energy band structure and perturbation analysis. The motion of the carriers can be followed by keeping track of their positions and velocities. It is convenient to do so by keeping track of the carrier distribution function, which gives the carrier concentration in six-dimensional (location and velocity) phase space as a function of time.

In the absence of collisions, the concentration $N(\bar{r}, \bar{v}, t)$ at the phase point (\bar{r}, \bar{v}) and time t will, according to the Liouville theorem,⁴⁸ follow its trajectory in phase space unchanged. A short time Δt later, it will reach the point $[\bar{r} + \bar{v}\Delta t, \bar{v} + (\bar{F}/m)\Delta t]$, where \bar{F} is the force acting and m the effective mass in the neighborhood of (\bar{r}, \bar{v}) . The only change in N between the two points will be due to collisions which scatter carriers into or away from the neighborhood of (\bar{r}, \bar{v}) . This can be described by writing

$$\frac{N[\bar{r} + \bar{v}\Delta t, \bar{v} + (\bar{F}/m)\Delta t, t + \Delta t] - N(\bar{r}, \bar{v}, t)}{\Delta t} = \frac{\delta_c N}{\Delta t}, \quad (2.1)$$

where $\delta_c N$ is the change due to collisions. In the limit as Δt approaches zero, Eq. 2.1 becomes

$$\frac{\partial N}{\partial t} = -\bar{v} \cdot \nabla N - \frac{\bar{F}}{m} \cdot \nabla_v N + \left(\frac{\partial N}{\partial t} \right)_c. \quad (2.2)$$

Equation 2.2 is the phase-space transport equation which describes the motion of carriers in the QFP approximation. The well known Boltzmann transport equation is similar to Eq. 2.2, with a collision term in the particular form which describes collision effects in a dilute gas.

Since N is a phase-space density, the densities of carriers, mean carrier momentum, and mean carrier energy in coordinate space can be defined in terms of the zeroth, first, and second velocity moments of N :

$$n(\bar{r}, t) = \int N(\bar{r}, \bar{v}, t) d^3v, \quad (2.3)$$

$$m^* n(\bar{r}, t) \bar{u}(\bar{r}, t) = \int m \bar{v} N(\bar{r}, \bar{v}, t) d^3v \quad (2.4)$$

and

$$n(\bar{r}, t) \bar{w}(\bar{r}, t) = \int \frac{1}{2} m |\bar{v}|^2 N(\bar{r}, \bar{v}, t) d^3v, \quad (2.5)$$

where n is the carrier concentration, \bar{u} is the average velocity, \bar{w} is the average energy, and m^* is the average over effective mass. It will be assumed that m is constant. This is reasonable so long as most of the carriers are fairly close to energy minima.

The energy and momentum conserving transport model consists of transport equations for the quantities n , \bar{u} , and \bar{w} . The equations can be derived by applying the method of moments to Eq. 2.2, the phase-space transport equation, as will now be shown. It is convenient to ignore the collision term in Eq. 2.2 for the time being; its effect on the equations to be derived here is taken up in Section 2.2.

Part of the operation of taking a velocity moment of Eq. 2.2 can be performed without regard for the form of a particular velocity moment operator. If ψ is any such operator, a general moment of Eq. 2.2 is given by

$$\int \psi \left(\frac{\partial N}{\partial t} \right) = - \bar{v} \cdot \nabla N - \frac{\bar{F}}{m} \nabla_v N \int d^3v. \quad (2.6)$$

Since ψ is a function of \bar{v} alone, Eq. 2.6 can be written as

$$\frac{\partial}{\partial t} \int N \psi d^3v = -\nabla \cdot \int \bar{v} N \psi d^3v + \frac{\bar{F}}{m} \cdot \int N \nabla_v \psi d^3v, \quad (2.7)$$

where it is assumed that N approaches zero rapidly enough at the limits of integration that the quantity $\int \nabla_v (N \psi) d^3v$ is always negligible.

The carrier concentration is the zeroth velocity moment of N . With $\psi = 1$, Eq. 2.7 becomes

$$\frac{\partial n}{\partial t} = -\nabla \cdot (n \bar{u}). \quad (2.8)$$

This is the usual carrier continuity equation, though no diffusion term appears in it explicitly. The velocity \bar{u} is the true average over the velocity distribution rather than the field-dependent "drift velocity" used in the static drift-diffusion model, so that the diffusion effects which must be treated there in a separate term are here incorporated into \bar{u} .

For velocity, ψ equals \bar{v} , and Eq. 2.7 becomes

$$\begin{aligned} \frac{\partial n \bar{u}}{\partial t} &= -\nabla \cdot \int \bar{v} N d^3v + \frac{\bar{F}}{m} \cdot \int N \left(\sum_i \hat{x}_i \frac{\partial \bar{v}}{\partial v_i} \right) d^3v \\ &= -\nabla \cdot \int \bar{v} N d^3v + \frac{\bar{F}}{m} \cdot \int N [I] d^3v, \quad (2.9) \end{aligned}$$

where $[I]$ is the identity tensor. The left-hand side of Eq. 2.9 can be expanded and rewritten using Eq. 2.8, resulting in

$$\frac{\partial \bar{u}}{\partial t} = -\frac{1}{n} \nabla \cdot \int \bar{v} N d^3v + \frac{\bar{F}}{m} + \frac{\bar{u}}{n} \nabla \cdot (n \bar{u}). \quad (2.10)$$

The remaining integral can be rewritten as

$$\begin{aligned} \frac{1}{n} \nabla \cdot \int \bar{v} N d^3v &= \frac{1}{n} \nabla \cdot \left[\int (\bar{v} - \bar{u})(\bar{v} - \bar{u}) N d^3v + \int (\bar{u}\bar{v} + \bar{v}\bar{u} - \bar{u}\bar{u}) N d^3v \right] \\ &= \frac{1}{n} \nabla \cdot \left[\frac{1}{m} [P] + \bar{u} n \right], \quad (2.11) \end{aligned}$$

where $[P]$ is a tensor defined by

$$P_{ij} = m \int N(v_i - u_i)(v_j - u_j) d^3v . \quad (2.12)$$

The remainder of the right-hand side of Eq. 2.11 can be expanded to

$$\frac{1}{n} \nabla \cdot (\overline{uun}) = \frac{1}{n} \int_i \left(\overline{u} \frac{\partial n u_i}{\partial x_i} + n u_i \frac{\partial \overline{u}}{\partial x_i} \right) = \frac{1}{n} \overline{u} \nabla \cdot (n \overline{u}) + \overline{u} \cdot \nabla \overline{u} . \quad (2.13)$$

Substituting for the integral in Eq. 2.10 results in

$$\frac{\partial \overline{u}}{\partial t} = - \overline{u} \cdot \nabla \overline{u} + \frac{\overline{F}}{m} - \frac{1}{nm} \nabla \cdot [P] . \quad (2.14)$$

Equation 2.14 describes the transport of average carrier velocity, in which the divergence of $[P]$ plays the role of a force field which contributes to acceleration. The first term on the right of Eq. 2.14 is related to the divergence of velocity flux. It is not in "conservation form,"⁴⁹ where the derivative operator acts on the entire term, as in the corresponding term in Eq. 2.8. This is because \overline{u} is not, in fact, a conserved quantity in carrier transport; it represents average, rather than total, momentum, and it is total momentum which is conserved physically.

For energy, ψ equals $m\overline{v} \cdot \overline{v}/2$. Substitution in Eq. 2.7 gives

$$\frac{\partial n\psi}{\partial t} = \frac{m}{2} \nabla \cdot \int \overline{v} N \overline{v} \cdot \overline{v} d^3v + \frac{\overline{F}}{2} \cdot \int N \nabla_v (\overline{v} \cdot \overline{v}) d^3v . \quad (2.15)$$

The second of the two integral terms in Eq. 2.15 can be simplified:

$$\begin{aligned} \frac{\overline{F}}{2} \cdot \int N \nabla_v (\overline{v} \cdot \overline{v}) d^3v &= \frac{\overline{F}}{2} \cdot \int N \sum_i \hat{x}_i \frac{\partial}{\partial v_i} (v_i^2) d^3v \\ &= \overline{F} \cdot \int N \overline{v} d^3v \\ &= n \overline{F} \cdot \overline{u} . \end{aligned} \quad (2.16)$$

Since $\int \bar{N} \bar{u} \cdot (\bar{v} - \bar{u}) d^3v$ is zero, the first of the integral terms can be written as

$$\begin{aligned}
 \frac{m}{2} \nabla \cdot \int \bar{v} \bar{N} \bar{v} \cdot \bar{v} d^3v &= \frac{m}{2} \nabla \cdot \left[\int (\bar{v} \cdot \bar{v} - \bar{u} \cdot \bar{u}) (\bar{v} - \bar{u}) \bar{N} d^3v + \int \bar{u} \bar{v} \cdot \bar{v} \bar{N} d^3v \right] \\
 &= \frac{m}{2} \nabla \cdot \left\{ \int [(\bar{v} - \bar{u}) \cdot (\bar{v} - \bar{u}) + 2\bar{u} \cdot (\bar{v} - \bar{u})] (\bar{v} - \bar{u}) \bar{N} d^3v \right. \\
 &\quad \left. + \frac{2}{m} \bar{w} \bar{n} \bar{u} \right\} \\
 &= \nabla \cdot (\bar{u} \cdot [\bar{P}] + \bar{q}) + \bar{n} \bar{u} \cdot \nabla \bar{w} + \bar{w} \nabla \cdot (\bar{n} \bar{u}) , \quad (2.17)
 \end{aligned}$$

where the vector \bar{q} is defined by

$$q_i = \int \frac{m}{2} N (v_i - u_i) (\bar{v} - \bar{u}) \cdot (\bar{v} - \bar{u}) d^3v . \quad (2.18)$$

With the use of Eqs. 2.8, 2.16 and 2.17, Eq. 2.15 becomes

$$\frac{\partial \bar{w}}{\partial t} = - \bar{u} \cdot \nabla \bar{w} + \bar{F} \cdot \bar{u} - \frac{1}{n} \nabla \cdot (\bar{u} \cdot [\bar{P}] + \bar{q}) . \quad (2.19)$$

Equation 2.19 describes the transport of average energy \bar{w} . Here again, as in Eq. 2.14, the flux divergence term $\bar{u} \cdot \nabla \bar{w}$ is in nonconservative form because average energy is not conserved physically. The vector \bar{q} is known in fluid mechanics as the heat flow vector.

2.1.2 Dependence on the Velocity Distribution. Equations 2.8, 2.14, and 2.19 describe the transport of velocity-averaged quantities, but their solution requires knowledge of the form of the velocity distribution N , which appears in the definitions of $[P]$ and \bar{q} . Some form of the velocity distribution must be assumed for the purpose of evaluating $[P]$ and \bar{q} . It should contain n , \bar{u} , and w as parameters, so that $[P]$ and \bar{q} will be consistent with these. At the same time, specifying the distribution beyond its second velocity moment is impractical, since the energy and momentum conserving model gives no information as to how the higher moments change with time. For the purpose of finding $[P]$ and \bar{q} , it will be assumed that the velocity distribution is displaced Maxwellian in form, which makes the integrations in Eqs. 2.12 and 2.18 particularly simple. The displaced Maxwellian form whose first three moments are consistent with n , \bar{u} , and w is

$$N = n \left(\frac{m}{2\pi k_b T_c} \right)^{3/2} \exp \left(- \frac{m |\bar{v} - \bar{u}|^2}{2k_b T_c} \right), \quad (2.20)$$

where k_b is Boltzmann's constant, and T_c is the carrier temperature, defined by

$$\begin{aligned} \frac{3}{2} k_b T_c &= \frac{1}{n} \int \frac{m}{2} |\bar{v} - \bar{u}|^2 N d^3v \\ &= \frac{1}{n} \int \frac{m}{2} (\bar{v} \cdot \bar{v} + \bar{u} \cdot \bar{u} - 2\bar{u} \cdot \bar{v}) N d^3v \\ &= w - \frac{m}{2} \bar{u} \cdot \bar{u}. \end{aligned} \quad (2.21)$$

Thus, the thermal component of w is $3k_b T_c/2$, in keeping with the usual idea of temperature.

Changing variables to $\bar{v}' = \bar{v} - \bar{u}$ simplifies the integrations in Eqs. 2.12 and 2.18. Since N is even in \bar{v}' , integration over all \bar{v}' of a product of N with a function that is odd in any component of \bar{v}' will give zero. Equations 2.12 and 2.18 then become

$$\begin{aligned} P_{ij} &= \int N v'_i v'_j m d^3 v' \\ &= 0, \quad i \neq j \\ &= nk_B T_c, \quad i = j \end{aligned} \quad (2.22)$$

and

$$\begin{aligned} q_i &= \int \frac{m}{2} N v'_i \sum_j v_j'^2 d^3 v' \\ &= 0, \quad \text{all } i. \end{aligned} \quad (2.23)$$

Then Eqs. 2.14 and 2.19 become

$$\frac{\partial \bar{u}}{\partial t} = -\bar{u} \cdot \nabla \bar{u} + \frac{q \bar{E}}{m} - \frac{2}{3nm} \nabla \left[n \left(w - \frac{1}{2} m \bar{u} \cdot \bar{u} \right) \right] \quad (2.24)$$

and

$$\frac{\partial w}{\partial t} = -\bar{u} \cdot \nabla w + q \bar{E} \cdot \bar{u} - \frac{2}{3n} \nabla \left[n \bar{u} \left(w - \frac{1}{2} m \bar{u} \cdot \bar{u} \right) \right], \quad (2.25)$$

where q is the electronic charge and \bar{E} is the electric field.

The forms in Eqs. 2.8, 2.24, and 2.25 of the collisionless transport equations are equivalent to the forms of the equations of hydrodynamics describing the motion of an inviscid, compressible fluid.⁵⁰ The terms arising from $[P]$ will be referred to as pressure terms because the diagonal entries in $[P]$ are just the pressure of an ideal gas with concentration n at temperature T_c . The pressure terms account for the momentum and energy imparted to carriers traveling down a pressure gradient in the carrier "gas."

The energy and momentum conserving transport model is not exact in the QFP approximation because it is in terms of only the first three velocity moments of N , rather than the exact form of N . It should be noted that \bar{q} has been eliminated going from Eqs. 2.19 to 2.24 because the assumed displaced Maxwellian distribution is symmetrical about \bar{u} . Blotekjaer⁴⁷ has suggested that the model can be improved by retaining nonzero \bar{q} in the energy transport equation. However, Bosch and Thim⁵¹ used an energy and momentum conserving model to simulate transferred electron devices and found that the inclusion of nonzero \bar{q} had little effect on predicted device behavior. It will be assumed here that the transport model will be sufficiently accurate for use in device modeling without the inclusion of \bar{q} in Eq. 2.25. It will also be assumed that carrier transport in IMPATTS is one-dimensional, so that henceforward the transport equations can be written in scalar form.

2.2 Collision Terms

This section develops terms for inclusion in the carrier, energy, and momentum transport equations which take into account the effects of the phase-space collision term. The procedure followed in the previous section was to find velocity moments of the collisionless phase-space equation. The collision terms will be found using a different procedure, for reasons which will be discussed.

2.2.1 Physical Considerations. The modifications which are to be made to the carrier, momentum, and energy transport equations, Eqs. 2.8, 2.24, and 2.25, must account for the rates at which carrier concentration, mean velocity and mean energy are changing because of

collision processes. These rates of change depend in reality on the exact form of the distribution function, but this is not known under the energy and momentum conserving model. The problem becomes one of accurately approximating the rates of change with functions of n , u , and w .

An obvious way of doing so is to find the first three velocity moments of the phase-space collision term and include them at the appropriate points in the analysis presented in the previous section. This is difficult to do, however, because the phase-space term can seldom be known with much accuracy. It contains the distribution function and functions describing the average rates and effects of the various collision types; e.g., phonon emission and absorption, impact ionization, impurity and defect scattering, and none of these is always known exactly. The rate function for impact ionization is very difficult to determine,⁵²⁻⁵⁴ and while functions are known for a number of other collision processes,⁵⁵ these contain adjustable parameters, whose values are in practice chosen to make theoretical predictions agree with experimental measurements.

In effect, measured data are what determine numerical values of the phase-space collision term. This suggests a more direct way of arriving at the carrier, energy, and momentum collision terms: that they be evaluated directly from this same data. This is the procedure that will be followed here.

2.2.2 Forms of the Collision Terms. Before the collision terms can be evaluated, the forms of their dependencies on the variables n , u , and w of the transport model must be established. The collision types to be accounted for (considered here in terms of their effects

on electrons) can be divided into three categories according to the types of carriers (electrons and/or holes) they involve:

1. Collisions undergone by electrons which change the concentration, energy, or momentum of electrons.
2. Collisions undergone by holes which change the concentration, energy, or momentum of electrons.
3. Electron-hole interactions which change the concentration, energy or momentum of electrons.

Electron-electron interactions are not considered because they have no effect on electron concentration, average energy, or average momentum. The effect of electron-electron scattering is in any case to make the distribution more nearly a displaced Maxwellian.⁵⁵

It will be assumed that all types of collisions which fit in categories (1) or (2) above involve single carriers, and that their per carrier rates are functions only of average carrier energy. Blotekjaer and Lunde⁵⁶ have shown that the latter assumption is reasonable in the case of a displaced Maxwellian distribution. They derived formulae for the energy and momentum relaxation times (defined below) by taking moments of the phase-space collision term. Their results, when written in terms of w , are independent of u to second order in u .

2.2.2.1 Same-Carrier Collisions. Category (1) above includes all lattice collisions undergone by electrons. Of these, the carrier concentration is affected by impact ionization, which contributes a generation rate to the carrier transport equation:

$$\left(\frac{\partial n}{\partial t}\right)_{c_1} = \alpha n, \quad (2.26)$$

where α is the average per electron ionization rate and is taken to be

a function of w . Its dimensions are inverse time, so it is different from the conventional electron ionization rate employed in the static model. The latter has dimensions of inverse length, as a carryover from studies of gas discharges.⁵⁷ In fact, the probability that an individual carrier will cause ionization in unit time is dependent upon its position in the energy band structure, a position which is, in the nonstatic case, largely independent of its velocity. The average of the probability over a group of carriers is therefore, in general, almost independent of their average velocity, so the per-unit-time ionization rate α as defined in Eq. 2.26 is more fundamental than the conventional, per-unit-distance rate.

Average momentum tends to be reduced by collision processes in Category (1), since they tend to randomize the velocity distribution. While the per-carrier rates of the processes are functions of energy, the resulting rate of loss of velocity cannot be a function of energy alone. This can be seen if two situations of equal energy and concentration are considered, one in which u is large and one in which u is zero. If the collision rates are functions only of energy, exactly the same number and types of collisions will be taking place in both situations. In the first, u is decreasing comparatively rapidly because of the randomizing effect of collisions. In the second, u is not changing at all, since it is already zero. The rate of change of velocity due to collisions is very different from one situation to the other.

The velocity and energy dependence of momentum loss in collisions belonging to the first category will be accounted for by writing

$$\left(\frac{\partial u}{\partial t}\right)_{c_1} = -\frac{u}{\tau_v}, \quad (2.27)$$

where τ_v is an energy-dependent, effective momentum relaxation time.

While the rate of loss of average energy to these collisions is a function of energy alone, it is convenient for the purposes of the finite-difference approximations to the transport equations developed in Chapter III to model the energy loss rate in terms of an energy relaxation time. The minimum energy, instead of being zero, is the thermal energy w_o associated with the temperature of the lattice, so the rate of energy loss will be written as

$$\left(\frac{\partial w}{\partial t}\right)_{c_1} = -\frac{(w - w_o)}{\tau_w}, \quad (2.28)$$

where τ_w is an energy dependent, effective energy relaxation time. The use of effective relaxation times in Eqs. 2.27 and 2.28 is in accordance with the forms of the energy and momentum transport equations given by Blotekjaer.⁴⁷

2.2.2.2 Opposite-Carrier Collisions. The second collision category consists (from the point of view of electrons) of impact ionization by holes. These contribute to the carrier generation rate,

$$\left(\frac{\partial n}{\partial t}\right)_{c_2} = \beta p, \quad (2.29)$$

where β is the per-unit-time hole ionization rate and depends on hole energy. Hole ionizations also affect electron average velocity and energy. If it is assumed that the electrons created by hole ionizations have random velocities, their contribution to the total electron momentum is zero:

$$\left(\frac{\partial nu}{\partial t}\right)_{c_2} = u \left(\frac{\partial n}{\partial t}\right)_{c_2} + n \left(\frac{\partial u}{\partial t}\right)_{c_2} = 0 . \quad (2.30)$$

Then, combining Eqs. 2.29 and 2.30 results in

$$\left(\frac{\partial u}{\partial t}\right)_{c_2} = - \frac{\beta p}{n} u . \quad (2.31)$$

The increase in the number of electrons dilutes the momentum and increases the rate at which momentum relaxes toward zero. Similarly, if the newly created electrons have average energy equal to w_0 , then

$$\left(\frac{\partial w}{\partial t}\right)_{c_2} = - \frac{\beta p}{n} (w - w_0) . \quad (2.32)$$

2.2.2.3 Electron-Hole Interactions. The third collision category includes Auger recombination and direct exchange of energy and momentum between electrons and holes. Sze⁵⁸ gives an estimate for the Auger recombination lifetime which is large compared to a millimeter-wave period of oscillation under any circumstances which might normally occur in an operating IMPATT. Blotekjaer and Lunde⁵⁶ have estimated the rates of energy and momentum transfer between electrons and holes under the assumption of a displaced Maxwellian distribution. Under ordinary conditions, their estimates are small in comparison to the rates of energy and momentum loss which result from the numerical values of the energy and momentum relaxation times as determined in the remainder of this section. These processes are apparently of minor importance in comparison to those in the first two collision categories and are ignored in the present study, although their inclusion offers no difficulty in principle.

2.2.3 The Complete Transport Equations. Adding the collision terms whose forms have now been determined to the carrier, velocity, and energy transport equations results in

$$\frac{\partial n}{\partial t} = - \frac{\partial nu}{\partial x} + \alpha n + \beta p , \quad (2.33)$$

$$\frac{\partial u}{\partial t} = - u \frac{\partial u}{\partial x} + \frac{qE}{m} - \frac{2}{3mn} \frac{\partial}{\partial x} \left[n \left(w - \frac{1}{2} mu^2 \right) \right] - \left(\frac{1}{\tau_v} + \frac{\beta p}{n} \right) u \quad (2.34)$$

and

$$\frac{\partial w}{\partial t} = - u \frac{\partial w}{\partial x} + quE - \frac{2}{3n} \frac{\partial}{\partial x} \left[nu \left(w - \frac{1}{2} mu^2 \right) \right] - \left(\frac{1}{\tau_w} + \frac{\beta p}{n} \right) (w - w_o) . \quad (2.35)$$

The complete energy and momentum conserving transport model consists of seven equations, the electron and hole versions of Eqs. 2.33 through 2.35 together with Poisson's equation for the electric field,

$$\frac{\partial E}{\partial x} = \frac{q}{\epsilon} (N_i - n + p) , \quad (2.36)$$

where N_i is the net density of ionized impurities.

2.2.4 Evaluations of Energy-Dependent Parameters. The collision terms in Eqs. 2.33 through 2.35 contain ionization rates and relaxation times which are as yet unknown functions of carrier energy. These functions must be given numerical values before the energy and momentum conserving transport model can be applied to device simulation, although the form of the model is independent of the particular procedure used to obtain numerical values. The method of evaluation which will be used here will be to determine the functions using values of drift velocity and ionization rate which are known

experimentally as functions of dc electric field. A mapping of the desired quantities onto the dc field is obtained by writing simplified versions of the transport equations applicable to the conditions under which experimental measurements are made and substituting in the known functions of field. A theoretically determined relationship between energy and dc field is used to complete the mapping onto energy. The resulting relationships between ionization rates, relaxation times, and energy will be assumed to hold under all conditions.

This procedure for evaluating the functions of energy is not the only possible one, but it has several advantages. It makes use of comparatively simple equations involving experimentally measured values of ionization rate and drift velocity, and guarantees that results of the model will agree with experiment in the static limit. It predicts forms for the energy and momentum relaxation times which are in accordance with physical expectations, such as both relaxation times becoming decreasing functions of energy in the energy range where impact ionization becomes significant. Finally, although the procedure makes use of certain assumptions about the forms the transport equations can take in the presence of spatially uniform dc electric fields, these are all confirmed by simulation results presented in Chapter IV.

2.2.4.1 The Static Transport Equations. It will be assumed that the circumstances to which experimentally measured values of electron drift velocity and ionization rate are appropriate include those of spatially uniform, dc electric field and negligible hole concentration. Under these conditions, all time derivatives and hole ionization terms drop out of the transport equations. The spatial derivatives of u and w will be neglected. (Simulation results for the

case of spatially uniform, dc field presented in Chapter IV support the use of this assumption.) The stated conditions of zero time variation and zero spatial variation of E , u , and w will be referred to as "uniform" conditions, under which the transport equations become

$$u \frac{\partial n}{\partial x} = \alpha n, \quad (2.37)$$

$$u = \frac{qE\tau_v}{m} - \frac{2\tau_v}{3mn} \left(w - \frac{1}{2} mu^2 \right) \frac{\partial n}{\partial x} \quad (2.38)$$

and

$$w - w_0 = quE\tau_w - \frac{2u\tau_w}{3n} \left(w - \frac{1}{2} mu^2 \right) \frac{\partial n}{\partial x}. \quad (2.39)$$

The two terms on the right-hand side of Eq. 2.38 can be identified with field-driven drift and diffusion down the carrier concentration gradient. Equating the first of these with the conventional drift velocity v_d yields

$$\tau_v = \frac{mv_d}{qE}. \quad (2.40)$$

Since v_d is known as a function of the uniform electric field, Eq. 2.40 relates τ_v to the field under the assumed static conditions.

The right-hand side of Eq. 2.37 expresses the same quantity as the conventional generation rate due to ionization by electrons. Equating the two gives

$$\alpha n = \frac{1}{q} J_n \alpha^*, \quad (2.41)$$

where J_n is the electron current density, and the conventional field-dependent ionization rate has been labeled with an asterisk. Since u is the average electron velocity and is a function of the uniform

field, Eq. 2.41 is equivalent to

$$\alpha = u\alpha^* . \quad (2.42)$$

This maps α onto E under uniform conditons. With the use of Eqs. 2.40 and 2.42, Eqs. 2.37 through 2.39 become

$$u = v_d - \frac{2v_d}{3qE} \left(w - \frac{1}{2} \mu u^2 \right) \alpha^* \quad (2.43)$$

and

$$w - w_0 = quE\tau_w - \frac{2u\tau_w}{3} \left(w - \frac{1}{2} \mu u^2 \right) \alpha^* . \quad (2.44)$$

Given the strength of the electric field, v_d and α^* are known in Eqs. 2.43 and 2.44. But the two equations are still in terms of three unknowns, u , w , and τ_w , so there is not enough information to map τ_v , τ_w , and α onto the energy w . Equations 2.43 and 2.44 with any mapping between energy and field will, however, guarantee that in the limit of slow changes of the electric field in time and space, results from the energy and momentum conserving model will agree with those from experiment. The next step is to find a physically reasonable mapping between the field and the corresponding mean energy for momentum distributions in equilibrium with the field. Several calculations of this mapping have been performed in the course of development of theories for the field dependence of the ionization rates.^{57,59,60}

2.2.4.2 The Uniform Energy-Field Relationship. The estimate for the distribution function which has been used in the present work was developed by Wolff⁵⁷ and has

$$\begin{aligned} N(c,E) &= A e^{-mc^2/2F} + B e^{-mc^2/2F} Ei(mc^2/2F) , \quad 0 < c < c_c \\ &= 0 , \quad c \geq c_c , \end{aligned} \quad (2.45)$$

where A and B are normalizing constants, c is the carrier speed, c_c is the speed at the energy threshold for impact ionization, and Ei is the exponential integral function. F is a function of the field defined by

$$F = \frac{(qE\lambda)^2}{3\hbar\omega} , \quad (2.46)$$

where λ is the mean free path for optical phonon emission and $\hbar\omega$ is the optical phonon energy. λ and the ionization threshold energy are chosen so that the ionization rates predicted by Wolff's theory are in reasonable agreement with measured values. Wolff assumed that ionization takes place relatively quickly once a carrier climbs above the energy threshold, so that negligibly few carriers are above threshold at any one time.

Wolff's distribution cannot apply at low values of field because it makes no allowance for equilibration between the carrier and lattice temperatures as the field approaches zero. It will be assumed that the distribution does apply when the field is at least 300 kV/cm, a value at which the static ionization rate has begun to be appreciable. In this range, the desired static w-E relation is just the second moment of Wolff's distribution:

$$w(E) = \int_0^c \frac{1}{2} mc^2 N(c, E) c^2 dc , \quad (2.47)$$

where the differential volume is a spherical shell in velocity space. The integration in Eq. 2.47 must be performed numerically because of the presence of the Ei function in the integrand.

For uniform fields of less than 300 kV/cm, it will be assumed that τ_w is given by a polynomial in the field. Knowledge of τ_w and

$\partial\tau_w/\partial E$ at the boundaries of the interval is sufficient to determine the coefficients of a third-order polynomial. τ_w and $\partial\tau_w/\partial E$ at 300 kV/cm can be inferred from Eqs. 2.43, 2.44, and 2.47. The remaining two boundary conditions are provided by examination of w when the field is close to zero. Since w is a minimum at zero field, it must be a function of even powers of field in the neighborhood of zero. It will be assumed that the carrier distribution is not significantly heated at low fields so that

$$w = w_0 + \frac{1}{2} \mu^2 \quad (2.48)$$

for fields close to zero. Since the impact ionization rate is negligible at low fields, Eq. 2.44 gives

$$w = quE\tau_w + w_0 \quad (2.49)$$

under this condition. Combining Eqs. 2.48 and 2.49 results in

$$\tau_w \Big|_{E=0} = \frac{m\mu}{2q} \quad , \quad (2.50)$$

where μ is the low-field mobility. The fact that w is even in E , together with Eq. 2.48, implies that

$$\frac{\partial\tau_w}{\partial E} \Big|_{E=0} = 0 \quad . \quad (2.51)$$

Though it is not important for the energy-field relation, it is interesting to note that a similar analysis involving Eq. 2.43 leads to

$$\tau_v \Big|_{E=0} = \frac{m\mu}{q} \quad . \quad (2.52)$$

This can also be seen directly from Eq. 2.40.

With $\tau_w(E)$ determined for $0 \leq E < 300$ kV/cm, the w-E relationship on this same range can be determined from Eqs. 2.43 and 2.44. It would be more direct to assume that w itself is a polynomial in E on this range, but this could result in w not monotonically increasing with E, which is nonphysical.

2.2.4.3 The Functions of Energy. Given the full range E-w relationship, the relaxation times and ionization rate can be found as functions of w. The parameters used in this process are shown in the Appendix for both electrons and holes. They include phonon energy and creation mean free path, ionization threshold energy, low-field mobility, effective mass, and parameters for the phenomenological relationships between drift velocity, conventional ionization rate, and static field. The lattice temperature is taken to be 500°K. The effective mass values used are those which apply at the energy minima, though they could be changed without affecting the form of the transport model. Figure 2.1 shows the static E-w relationships for electrons and holes, while Figs. 2.2 and 2.3 give the relaxation times and ionization rates as functions of energy.

2.3 Relationship to Other Models

In Chapter I, it was mentioned that other nonstatic IMPATT models have been attempted. These will now be assessed. The conditions under which the energy and momentum conserving model limits to the conventional drift-diffusion model are also described.

2.3.1 The Energy Conserving Model. Kafka and Hess⁴¹ developed an IMPATT model which includes energy conservation and energy-dependent ionization rates, together with conventional field-dependent velocities. Their energy transport equation is similar to Eq. 2.35, although

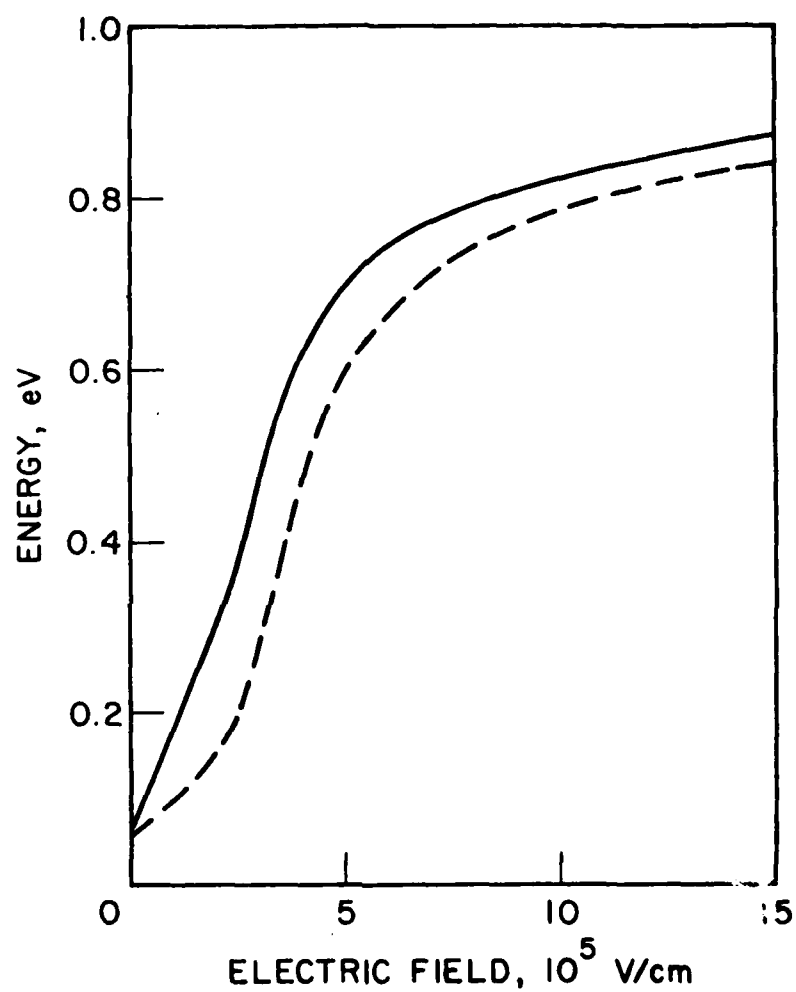


FIG. 2.1 ELECTRON AVERAGE ENERGY (SOLID CURVE) AND HOLE AVERAGE ENERGY (DASHED CURVE) VS. ELECTRIC FIELD STRENGTH UNDER UNIFORM CONDITIONS.

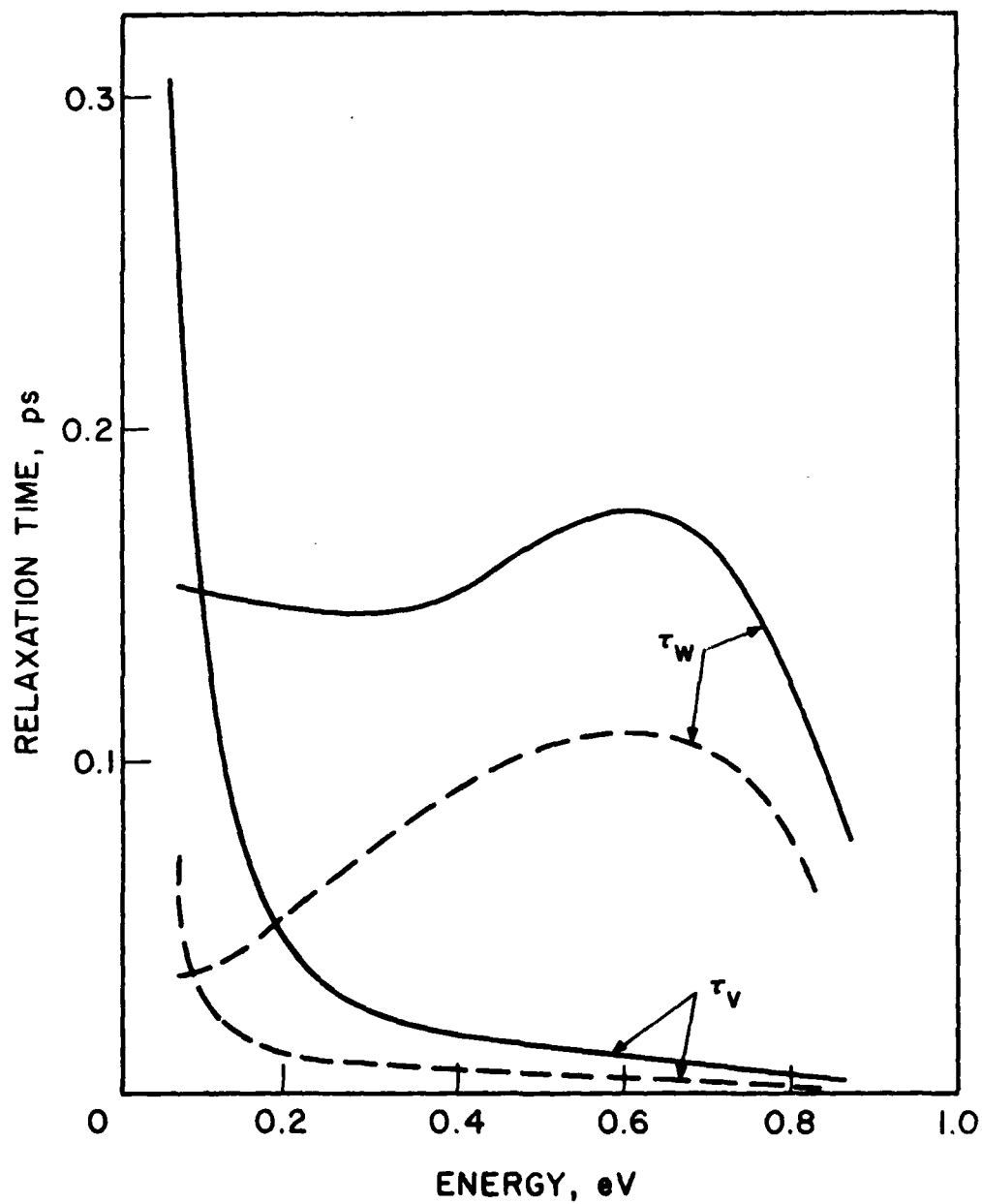


FIG. 2.2 ENERGY AND MOMENTUM RELAXATION TIMES VS. AVERAGE ENERGY FOR ELECTRONS (SOLID CURVES) AND HOLES (DASHED CURVES) IN SI AT 500°K.

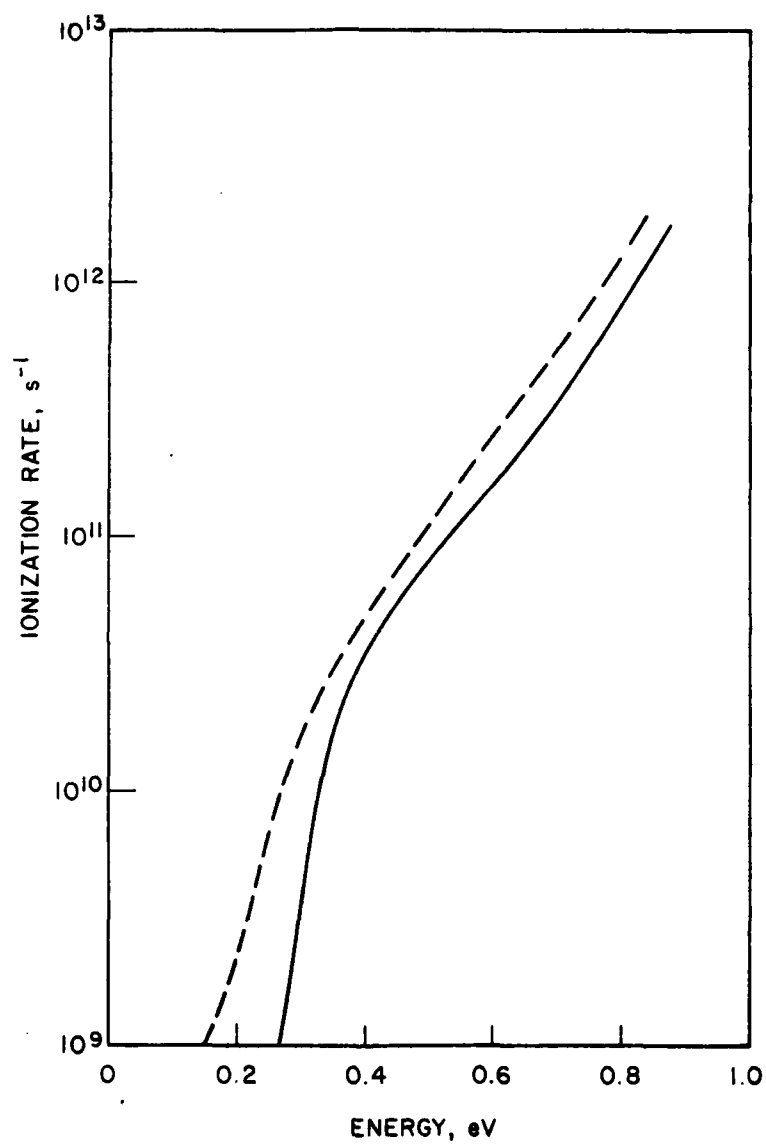


FIG. 2.3 IONIZATION RATE VS. AVERAGE ENERGY FOR ELECTRONS (SOLID CURVE) AND HOLES (DASHED CURVE) IN Si AT 500°K.

it includes a nonzero heat flow vector, but it is written in terms of the total energy of electrons and holes together, so that the model does not treat the electron and hole energies independently. Kafka and Hess assert that their model becomes equivalent to the conventional one when the flux divergence, pressure, and heat flow terms are dropped from the energy transport equation. Since they saw significant differences in their simulation results depending upon whether these terms were dropped, they concluded that the terms represent effects not allowed for by the conventional model which are important factors in the operation of millimeter-wave IMPATTs.

Unfortunately, the reduced form of the Kafka and Hess transport model is inconsistent. The pressure term in the energy transport equation does not drop out unless the carrier concentration gradient is zero, but a nonzero gradient must in fact exist when impact ionization is present. Instead of disappearing, the pressure term in the energy transport equation of the reduced model should take the form which appears in Eq. 2.39.

It is not certain that this oversight affected the results obtained by Kafka and Hess, but it may have done so. Under static* conditions, all the terms in the energy transport equation become small, except those which appear in Eq. 2.39. These remaining terms determine a relationship between energy and field, hence, also between energy-dependent ionization rates and field. In the reduced

*The term "static" is used here in the sense as defined in Chapter I, where it refers to conditions of sufficiently slow space and time variation of the electric field to allow the carrier momentum distribution to reach equilibrium with the field.

version of the model, one of the terms in Eq. 2.39 is missing, and a different relationship between ionization rate and field results.

What Kafka and Hess may in effect have done was to perform two essentially static simulations with different sets of ionization rates. This possibility is consistent with the facts that they were able to make their results from the two models agree by adjusting the ionization rates, and that their plot of the carrier temperature profile shows relatively constant temperature and field across the ionization region of their device, indicating that the carrier momentum distribution did reach equilibrium with the field in precisely the region where impact ionization was taking place.

2.3.2 Energy and Momentum Balance Models. Constant and co-workers^{39,40} have developed two Read-type IMPATT models based on energy and momentum balance relationships. Their first model applied these relationships to the IMPATT drift region while treating the ionization region in the conventional manner.³⁹ The second applied the energy balance relationship, with energy-dependent ionization rates, to the ionization region, while assuming saturated drift throughout the device.⁴⁰ (This was done partly in an effort to confirm the effects of avalanche delay due to energy conservation which had been reported previously in connection with certain results from the present work.^{61,62}) Neither of the energy and momentum balance models treats the entire device in a unified way.

The balance relationships used by Constant and Salmer are similar to those proposed by Shur⁶³ and are equivalent to

$$\frac{du}{dt} = \frac{qE}{m} - \frac{u}{\tau_v} \quad (2.53)$$

and

$$\frac{dw}{dt} = quE - \frac{w - w_0}{\tau_w}, \quad (2.54)$$

where τ_w is assumed to be constant. These relationships are just approximate versions of Eqs. 2.34 and 2.35. They omit the effects of momentum and energy flux divergence, of the pressure terms, and of the spatial dependence of u , w , and E . The balance models make allowances for nonequilibrium between the carrier velocity distribution and the electric field but tend to overestimate its effects, since they assume that nonequilibrium extends uniformly over the entire drift or ionization width, ignoring the fact that carriers will tend to approach equilibrium with the field as they traverse a region of uniform field. It should also be noted that diffusion effects, which are included in even the conventional static model, are not allowed for in Eqs. 2.53 and 2.54.

2.3.3 The Drift-Diffusion Limit. If the difference between the energy and momentum conserving model and the conventional drift-diffusion model lies in whether nonequilibrium conditions are allowed for, then the two models should be equivalent once equilibrium is reached. This is indeed the case. When the field changes slowly in time and space, the velocity transport equation reduces to Eq. 2.38. Substituting Eq. 2.38 for u in Eq. 2.33 gives

$$\begin{aligned} \frac{\partial n}{\partial t} &= - \frac{\partial}{\partial x} \left(\frac{nq\tau_v E}{m} \right) + \frac{\partial}{\partial x} \left(\frac{\tau_v k_b T}{m} \frac{\partial n}{\partial x} \right) + G \\ &= - \frac{\partial}{\partial x} (n\mu E) + \frac{\partial}{\partial x} \left(D \frac{\partial n}{\partial x} \right) + G, \end{aligned} \quad (2.55)$$

where

$$\mu = \frac{q\tau_v}{m}, \quad (2.56)$$

$$D = \frac{\tau_v k_b T_c}{m}, \quad (2.57)$$

and G is the carrier generation rate. Equation 2.55 is just the standard drift-diffusion equation for electrons with mobility μ and diffusion coefficient D . D and μ satisfy the Einstein relation in terms of T_c . D can be calculated as a function of field from Eq. 2.57 using the static relationships between field, energy, and relaxation time found previously. Results are shown in Fig. 2.4. This static $D(E)$ relation is a consequence of the assumed static $w(E)$; one mapping implies the other. It would be possible to assume $D(E)$ and derive $w(E)$, but comparatively little is known about the physical situation in Si from which to perform ab initio construction of $D(E)$, especially at high field strengths. An apparently reasonable choice of $D(E)$ can easily lead to an unreasonable $w(E)$, such as one where w is not monotonically increasing with E or where w reaches values well in excess of the ionization threshold. The latter would, in fact, result from the $D(E)$ assumed in at least one IMPATT simulation study based on the drift-diffusion model.⁶⁴

2.4 Summary and Conclusions

An energy and momentum conserving transport model for carriers in Si has been developed. The model consists of transport equations which are velocity moments of the phase-space transport equation. The collision terms are evaluated by requiring that under conditions of slow time and space variation of electric field the results of the

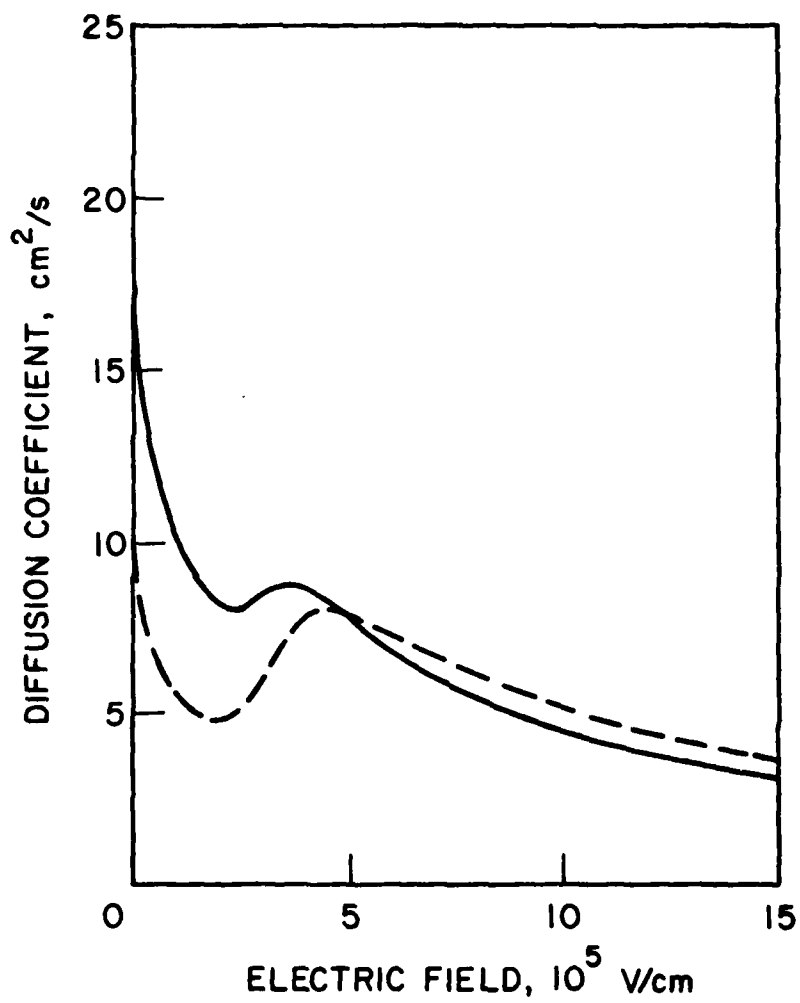


FIG. 2.4 DIFFUSION COEFFICIENT VS. ELECTRIC FIELD STRENGTH
FOR ELECTRONS (SOLID CURVE) AND HOLES (DASHED CURVE)
IN Si AT 500°K.

model must be consistent with experimentally measured carrier velocities and ionization rates.

The model is free of the chief limitation of the conventional drift-diffusion model in that it does not assume equilibrium between the carrier velocity distribution and local electric field. It is also more general and self-consistent than all previous attempts to produce nonstatic transport models applicable to IMPATTs.

CHAPTER III.

NUMERICAL METHODS FOR IMPATT DIODE SIMULATION

This chapter describes the numerical implementation of the energy and momentum conserving transport model which has been used to simulate the operation of Si IMPATT diodes. The organization of the chapter is as follows. In Section 3.1 a set of normalizations for finite-difference approximations to the transport equations is developed. Section 3.2 considers the stability and accuracy of various finite-difference forms and describes the form which has been chosen for the simulation program. Section 3.3 explains how the program applies spatial and temporal boundary conditions to the finite-difference equations, and Section 3.4 describes the findings and conclusions of this chapter.

3.1 Normalizations

There are a number of constants, such as time and space step length, which appear repeatedly in finite-difference approximations to the transport equations developed in Chapter II. If the finite-difference equations are normalized with regard to these constants, the equations are simplified, and efficiency is greatly increased. This section describes the set of normalizations which has been used in the present study.

The transport equations are repeated here for convenience:

$$\frac{\partial n}{\partial t} = - \frac{\partial nu}{\partial x} + \alpha n + \beta p , \quad (3.1)$$

$$\frac{\partial u}{\partial t} = -u \frac{\partial u}{\partial x} + \frac{qE}{m} - \frac{2}{3mn} \frac{\partial}{\partial x} \left[n \left(w - \frac{1}{2} mu^2 \right) \right] - u \left(\frac{1}{\tau_v} + \frac{p}{n} \beta \right) \quad (3.2)$$

and

$$\frac{\partial w}{\partial t} = -u \frac{\partial w}{\partial x} + quE - \frac{2}{3n} \frac{\partial}{\partial x} \left[nu \left(w - \frac{1}{2} mu^2 \right) \right] - (w - w_o) \left(\frac{1}{\tau_w} + \frac{p}{n} \beta \right) \quad (3.3)$$

Their general finite-difference approximations are given by

$$\frac{\delta_t n}{\Delta t} = - \frac{\delta_x}{\Delta x} (nu) + \alpha n + \beta p \quad , \quad (3.4)$$

$$\frac{\delta_t u}{\Delta t} = -u \frac{\delta_x}{\Delta x} u + \frac{qE}{m} - \frac{2}{3mn} \frac{\delta_x}{\Delta x} \left[n \left(w - \frac{1}{2} mu^2 \right) \right] - u \left(\frac{1}{\tau_v} + \frac{p}{n} \beta \right) \quad (3.5)$$

and

$$\frac{\delta_t w}{\Delta t} = -u \frac{\delta_x w}{\Delta x} + quE - \frac{2}{3n} \frac{\delta_x}{\Delta x} \left[nu \left(w - \frac{1}{2} mu^2 \right) \right] - (w - w_o) \left(\frac{1}{\tau_w} + \frac{p}{n} \beta \right) \quad , \quad (3.6)$$

where δ_t represents any finite-difference in time, δ_x is any finite-difference operator in space, and Δ is an incremental operator.

(Only constant Δt and Δx will be considered.) When the same notation is used, the finite-difference approximation to Poisson's equation is

$$\frac{\delta_x E}{\Delta x} = \frac{q}{\epsilon} (N_d - N_a + p - n) \quad . \quad (3.7)$$

In Eq. 3.4, use of a normalized velocity

$$\underline{u} = u \frac{\Delta t}{\Delta x} \quad (3.8)$$

and normalized generation rates

$$\underline{\alpha}, \underline{\beta} = \alpha \Delta t, \beta \Delta t \quad (3.9)$$

gives

$$\delta_t n = \delta_x (\underline{n}u) + \underline{\alpha}n + \underline{\beta}p, \quad (3.10)$$

where an underscore denotes a normalized quantity. As the normalized form of Eq 3.4, Eq. 3.10 contains neither Δx nor Δt . If Eq. 3.5 is multiplied by $\Delta t^2/\Delta x$, the result is

$$\delta_t \underline{u} = -\underline{u} \delta_x \underline{u} + \frac{qE}{m} \frac{\Delta t^2}{\Delta x} - \frac{2}{3n} \delta_x \left[n \left(\frac{w}{m} \frac{\Delta t^2}{\Delta x^2} - \frac{1}{2} \underline{u}^2 \right) \right] - \underline{u} \left(\frac{\Delta t}{\tau_v} + \frac{p}{n} \underline{\beta} \right). \quad (3.11)$$

This suggests that energy, relaxation time, and electric field be normalized as

$$\underline{w} = w \frac{\Delta t^2}{m \Delta x^2}, \quad (3.12)$$

$$\underline{\tau} = \frac{\tau}{\Delta t} \quad (3.13)$$

and

$$\underline{E} = \frac{qE\Delta t^2}{\Delta x}. \quad (3.14)$$

The normalizations given by Eqs. 3.8, 3.9, and 3.12 through 3.14 eliminate Δx and Δt from Eqs. 3.5 and 3.6. The electric field is not normalized with respect to effective mass because the field appears in both the electron and the hole transport equations, where two different values of effective mass apply.

Using the normalized field in Eq. 3.7 gives

$$\delta_x \underline{E} = \frac{q^2 \Delta t^2}{\epsilon} (N_d - N_a + p - n), \quad (3.15)$$

so that it is convenient to define a normalization for carrier and doping concentration by

$$\underline{n} = \frac{q^2 \Delta t^2}{\epsilon} n \quad . \quad (3.16)$$

Normalization of the carrier concentrations has no effect on Eqs. 3.4 through 3.6.

Along with Eq. 3.10, the normalized versions of Eqs. 3.4 through 3.7 are

$$\delta_t \underline{u} = - \underline{u} \delta_x \underline{u} + \frac{\underline{E}}{\underline{m}} - \frac{2}{3\underline{n}} \delta_x \left[\underline{n} \left(\underline{w} - \frac{1}{2} \underline{u}^2 \right) \right] - \underline{u} \left(\frac{1}{\underline{\tau}_v} + \frac{\underline{p}}{\underline{n}} \underline{\beta} \right) \quad , \quad (3.17)$$

$$\delta_t \underline{w} = - \underline{u} \delta_x \underline{w} + \frac{\underline{uE}}{\underline{m}} - \frac{2}{3\underline{n}} \delta_x \left[\underline{n} \underline{u} \left(\underline{w} - \frac{1}{2} \underline{u}^2 \right) \right] - (\underline{w} - \underline{w}_0) \left(\frac{1}{\underline{\tau}_w} + \frac{\underline{p}}{\underline{n}} \underline{\beta} \right) \quad (3.18)$$

and

$$\delta_x \underline{E} = (\underline{N}_d - \underline{N}_a + \underline{p} - \underline{n}) \quad . \quad (3.19)$$

Table 3.1 summarizes the normalizations. Henceforth, the underscore notation for normalized quantities will be omitted, and when it is not apparent from context whether the quantities referred to are normalized or not, this will be stated specifically.

3.2 Finite-Difference Operators

There are many possible forms for Eqs. 3.10, 3.17, and 3.18, corresponding to different forms of the operators δ_x and δ_t , and to different choices of time levels at which the various spatial difference terms are evaluated. An optimum finite-difference form will be one which is both accurate and efficient, but the goals of maximum

Table 3.1
Normalizations for Finite-Difference Forms
of the Transport Equations

<u>Quantity</u>	<u>Symbol</u>	<u>Normalized Quantity</u>
Average velocity	u	$\underline{u} = u(\Delta t/\Delta x)$
Average energy	w	$\underline{w} = (w/m)(\Delta t/\Delta x)^2$
Particle concentration	n	$\underline{n} = n[(q^2\Delta t^2)/\epsilon]$
Electric field	E	$\underline{E} = (qE\Delta t^2)/(\Delta x)$
Relaxation time	τ	$\underline{\tau} = \tau/\Delta t$
Ionization rate	α, β	$\underline{\alpha}, \underline{\beta} = \alpha\Delta t, \beta\Delta t$

accuracy and maximum efficiency are incompatible. This section shows how a compromise between the two has been reached.

It will be assumed that the ratio $\Delta x/\Delta t$ will have some minimum value which will be given by the form of the Courant-Friedrichs-Lewy condition which applies to whatever particular numerical form is chosen for the transport equations. If this ratio is always given its minimum value, the normalized drift and pressure terms in Eqs. 3.10, 3.17 and 3.18 become independent of Δx and Δt , while the normalized source (carrier generation and field) and relaxation terms become proportional to Δt .

In order to resolve events which take long enough in relation to the RF period to be of importance to device operation, Δt itself must be sufficiently small. The time step will become smaller as frequency increases, and vice versa. In the limit of very small Δt , the drift and pressure terms will dominate the normalized finite-difference equations, and in the limit of large Δt , the field, generation, and relaxation terms will dominate. This is reflective of the shift from static to nonstatic transport as device speed increases and the characteristic time scale becomes shorter. In a comparatively slow device, static equilibrium between the field and relaxation terms adequately describes the transport of carriers. In a faster device, the nonstatic effects of drift and pressure on the momentum and energy become important.

It is convenient to begin a discussion of finite-difference approximations to Eqs. 3.1 through 3.3 at the limit of very short time scale and small Δt , when the normalized source and relaxation terms can be neglected. If it is to be useful in general, any

approximation must be useful in this limit. Therefore, the first part of this section is concerned with the sourceless and collisionless version of the finite-difference model, and the second part with the further considerations which arise when the source and collision terms are restored to the finite-difference equations.

3.2.1 Transport in the Limit of Short Time Step. The sourceless and collisionless forms of Eqs. 3.10, 3.17, and 3.18 are

$$\delta_t n = -\delta_x (nu) , \quad (3.20)$$

$$\delta_t u = -u\delta_x u - \frac{2}{3n} \delta_x \left[n \left(w - \frac{1}{2} u^2 \right) \right] \quad (3.21)$$

and

$$\delta_t w = -u\delta_x w - \frac{2}{3n} \delta_x \left[nu \left(w - \frac{1}{2} u^2 \right) \right] . \quad (3.22)$$

Various forms of the difference operators will now be considered.

3.2.1.1 Forward-Time, Upwind Drift Differences. Using forward-time differences in Eqs. 3.20 through 3.22 requires less storage than centered differences, and it is simplest to evaluate all the spatial difference terms at present time. Upwind differencing tends to preserve the "transportive"* property of drift, while centered differencing of the pressure term in Eq. 3.21 will reflect the fact that acceleration due to pressure differences acts in both the upstream and downstream directions. The pressure terms in Eq. 3.22 can be interpreted as keeping track of the work done by carriers in drifting through the pressure field, so upwind differencing is appropriate.⁴⁹ A reasonable form for Eqs. 3.20 through 3.22 would

*The term "transportive" is applied here as it is defined in Reference 49, p. 67.

therefore appear to be

$$n_j^{t+\Delta t} = n_j^t - n_j^t(u_j^t - u_{j-1}^t) - u_j^t(n_j^t - n_{j-1}^t) , \quad (3.23)$$

$$u_j^{t+\Delta t} = u_j^t - u_j^t(u_j^t - u_{j-1}^t) - \frac{1}{3n_j^t} \left([w_j^t - \frac{1}{2}(u_j^t)^2](n_{j+1}^t - n_{j-1}^t) \right. \\ \left. + n_j^t[w_{j+1}^t - w_{j-1}^t - u_j^t(u_{j+1}^t - u_{j-1}^t)] \right) \quad (3.24)$$

and

$$w_j^{t+\Delta t} = w_j^t - u_j^t(w_j^t - w_{j-1}^t) - \frac{2}{3n_j^t} \left([w_j^t - \frac{1}{2}(u_j^t)^2][(n_j^t - n_{j-1}^t)u_j^t \right. \\ \left. + (u_j^t - u_{j-1}^t)n_j^t] + u_j^t n_j^t [w_j^t - w_{j-1}^t - u_j^t(u_j^t - u_{j-1}^t)] \right) , \quad (3.25)$$

where subscripts denote position in the space mesh and superscripts position in time.

3.2.1.2 Stability Analysis. The stability of Eqs.

3.23 through 3.25 can be examined by extending the usual Fourier stability analysis to three variables in the way outlined by

Potter.⁵⁰ The solution to Eqs. 3.23 through 3.25 at a point in time is a vector function on the points of the space mesh. This function has a Fourier decomposition which can be denoted by

$$\begin{bmatrix} n_j^t \\ u_j^t \\ w_j^t \end{bmatrix} = \vec{f}_j^t = \sum_{m=-M}^M \vec{f}_m^t e^{ij\beta_m} , \quad (3.26)$$

where

$$\beta_m = m\pi/M, \quad (3.27)$$

i is the square root of -1 , and M is the number of points in the mesh.

The numerical error ξ present in the solution has a similar decomposition. When the error is small, it changes linearly across a time step, and the change in each of its Fourier components can be expressed in terms of an amplification matrix $[G]$:

$$\xi_m^{t+\Delta t} = ([I] + [G_m])\xi_m^t. \quad (3.28)$$

The identity matrix in Eq. 3.28 accounts for the effect of the forward time operator used in each of Eqs. 3.23 through 3.25. The particular form of $[G_m]$ corresponding to these equations can be found by substituting the Fourier series for ξ_j^t into Eqs. 3.23 through 3.25, resulting in $2M + 1$ component equations similar to Eq. 3.28. Linear change in the error means that the variable coefficients of the spatial differences can be treated as constants across each time step, so $[G_m]$ is given by

$$[G_m] = \begin{bmatrix} -u(1 - e^{-i\beta_m}) & -n(1 - e^{-i\beta_m}) & 0 \\ -\frac{2i}{3n}(w - \frac{1}{2}u^2) \sin \beta_m & -u(1 - e^{-i\beta_m}) + \frac{2iu}{3} \sin \beta_m & -\frac{2i}{3} \sin \beta_m \\ -\frac{2u}{3n}(w - \frac{1}{2}u^2)(1 - e^{-i\beta_m}) & -\frac{2}{3}(w - \frac{3}{2}u^2)(1 - e^{-i\beta_m}) & -\frac{5}{3}u(1 - e^{-i\beta_m}) \end{bmatrix}. \quad (3.29)$$

Stability of Eqs. 3.23 through 3.25 requires that no component of the error be able to grow in magnitude across a time step. Equation 3.28 implies that this will be true if, for all $-\pi < \beta_m \leq \pi$, all the eigenvalues λ of $[G_m]$ satisfy

$$|1 + \lambda|^2 \leq 1 . \quad (3.30)$$

It is tedious to solve the characteristic equation of $[G_m]$ directly, but there is a simpler way of getting the same information. The upper-left entry in $[G_m]$, which results from the upwind drift operator, repeats in the other two entries on the diagonal, so $[G_m]$ is the sum of two simpler matrices:

$$[G_m] = -u(1 - e^{-i\beta_m})[I] + [G'_m] , \quad (3.31)$$

where

$$[G'_m] = \begin{bmatrix} 0 & -n(1 - e^{-i\beta_m}) & 0 \\ -\frac{2i}{3n}(w - \frac{1}{2}u^2) \sin \beta_m & \frac{2iu}{3} \sin \beta_m & -\frac{2i}{3} \sin \beta_m \\ -\frac{2u}{3n}(w - \frac{1}{2}u^2)(1 - e^{-i\beta_m}) & -\frac{2}{3}(w - \frac{3}{2}u^2)(1 - e^{-i\beta_m}) & -\frac{2u}{3}(1 - e^{-i\beta_m}) \end{bmatrix} . \quad (3.32)$$

Any eigenvector of $[G'_m]$ is an eigenvector of $[G_m]$, and when λ' is an eigenvalue of $[G'_m]$, the corresponding eigenvalue of $[G_m]$ is given by

$$\lambda = \lambda' - u(1 - e^{-i\beta_m}) . \quad (3.33)$$

The characteristic equation of $[G'_m]$ is

$$\lambda' [\lambda'^2 + \frac{2u}{3} \lambda' (1 - e^{-i\beta_m} - i \sin \beta_m) - \frac{4i}{9} (w - \frac{1}{2} u^2) (1 - e^{-i\beta_m}) \sin \beta_m] - \frac{2i\lambda'}{3} (w - \frac{1}{2} u^2) (1 - e^{-i\beta_m}) \sin \beta_m = 0, \quad (3.34)$$

which results in $\lambda'_1 = 0$ and

$$\lambda'_{2,3} = -\frac{u}{3} (1 - 3 e^{-i\beta_m} - i \sin \beta_m) \pm \frac{1}{3} [(1 - e^{-i\beta_m} - i \sin \beta_m)^2 + 10i (w - \frac{1}{2} u^2) \sin \beta_m (1 - e^{-i\beta_m})]^{\frac{1}{2}}. \quad (3.35)$$

λ_1 corresponding to λ'_1 satisfies Eq. 3.30 for any value of β_m . λ'_2 and λ'_3 are somewhat complicated functions of β_m , but they can be simplified by noting that w is nearly always large in comparison to u^2 . The magnitudes of λ'_2 and λ'_3 are largest when $\beta_m = \pi/2$, when the two eigenvalues are given approximately by

$$\lambda'_{2,3} \approx -\frac{u}{3} \pm [\frac{10}{9} w (i - 1)]^{\frac{1}{2}}. \quad (3.36)$$

When the plus sign is used, Eq. 3.30 becomes approximately

$$|1 - 1.33u + 0.48\sqrt{w} + 1.2i\sqrt{w}|^2 \leq 1. \quad (3.37)$$

Equation 3.37 is seldom if ever satisfied under the conditions which occur in an operating IMPATT. This means that the numerical method given by Eqs. 3.23 through 3.25 is unstable in the limit of small Δt . It will be shown, however, that when Δt is sufficiently large, the method can be stabilized by proper treatment of the relaxation terms, so that it has been possible to use the method as

shown in Eqs. 3.23 through 3.25 in much of the diode simulation work performed in the course of this study.

3.2.1.3 Forward-Time, Centered Space Differences. In order to develop a stable method, it is useful to examine another form of Eqs. 3.20 through 3.22. The reason for the instability of Eqs. 3.23 through 3.25 is that \sqrt{w} appears in the real part of λ , where it adds in Eq. 3.37 to the number one which appears from the forward-time operator. The presence of the quantity $1 - e^{-i\beta_m}$ in $[G'_m]$ is what causes this. If all the upwind differences which contribute $1 - e^{-i\beta_m}$ are changed to centered differences, they will instead contribute $i \sin \beta_m$, and $[G'_m]$ will become

$$[G'_m] = \begin{bmatrix} 0 & -i \sin \beta_m & 0 \\ -\frac{2i}{3n}(w - \frac{1}{2}u^2) \sin \beta_m & \frac{2iu}{3} \sin \beta_m & -\frac{2i}{3} \sin \beta_m \\ -\frac{2iu}{3n}(w - \frac{1}{2}u^2) \sin \beta_m & -\frac{2i}{3}(w - \frac{3}{2}u^2) \sin \beta_m & -\frac{2iu}{3} \sin \beta_m \end{bmatrix} \quad (3.38)$$

The eigenvalues of $[G'_m]$ are now

$$\lambda'_1 = 0$$

and

$$\lambda'_{2,3} = \pm i \sin \beta_m \left[\frac{10}{9}(w - \frac{1}{2}u^2) \right]^{\frac{1}{2}} \quad (3.39)$$

But now when $\beta_m = \pi/2$, Eq. 3.30 becomes

$$|1 \pm i[\frac{10}{9}(w - \frac{1}{2}u^2)]^{\frac{1}{2}}|^2 \leq 1 \quad (3.40)$$

Equation 3.40 can never be satisfied, so the modified version of Eqs. 3.23 through 3.25 is no more stable than the original.

3.2.1.4 The Lax Method. There is a stable form of Eqs. 3.20 through 3.22 which is explicit and involves just two time levels. It is based on a numerical form developed by Lax⁶⁵ for the usual equations of hydrodynamics, which are similar to Eqs. 3.20 through 3.22. This form uses centered differencing for all differences in space but differs from the one just described in that it uses a modified forward-time operator:

$$\delta_t x_j = x_j^{t+\Delta t} - \frac{1}{2}(x_{j+1}^t + x_{j-1}^t) \quad (3.41)$$

where x is any of the normalized transport variables. The new time operator changes Eq. 3.30 to

$$|\cos \beta_m + \lambda|^2 \leq 1 \quad (3.42)$$

and centered drift changes Eq. 3.33 to

$$\lambda = -iu \sin \beta_m + \lambda' \quad (3.43)$$

For the Lax method, $[G'_m]$ and its eigenvalues remain as in Eqs. 3.38 through 3.39, so Eq. 3.42 requires

$$|u| + [\frac{10}{9}(w - \frac{1}{2}u^2)]^{\frac{1}{2}} \leq 1 \quad (3.44)$$

In terms of unnormalized quantities, Eq. 3.44 requires

$$\frac{\Delta x}{\Delta t} \geq |u| + [\frac{10}{9}(\frac{w}{m} - \frac{1}{2}u^2)]^{\frac{1}{2}} \quad (3.45)$$

Equation 3.45 is a statement of the Courant-Friedrichs-Lewy condition as it applies to Eqs. 3.20 through 3.22. The right-hand side is the sum of the advection speed $|u|$ and the speed at which a pressure disturbance can propagate.⁵⁰ The latter is analogous to the speed of sound in a fluid. This speed is often several times larger than $|u|$ when carriers in a semiconductor are considered, so Eq. 3.45 restricts Δt to be several times smaller in relation to Δx than does the least restrictive condition which may apply to simulations using the drift-diffusion model, i.e.,³⁸

$$\frac{\Delta x}{\Delta t} \geq v_d, \quad (3.46)$$

where v_d is the static drift velocity. (The form of Eq. 3.45 also illustrates the usefulness of having the same $\Delta x/\Delta t$ in all simulations, since the stability of numerical methods tends to depend on this ratio.)

The stability of the Lax method is achieved at the price of a comparatively large amount of numerical diffusion. The method introduces a spurious diffusion term into each transport equation, with a diffusion coefficient given by⁴⁹

$$D_n = \frac{\Delta x^2}{2\Delta t} \left(1 - u^2 \frac{\Delta t^2}{\Delta x^2} \right), \quad (3.47)$$

where u is the unnormalized drift velocity. Since Eq. 3.45 usually requires that $\Delta x/\Delta t$ be at least 5×10^7 cm/s, D_n can easily exceed the effective diffusion coefficients derived in Chapter II.

3.2.1.5 Three-Level Schemes. Numerical diffusion can be substantially eliminated by the use of a three-time-level scheme. A number of such schemes have been developed for the

hydrodynamic equations and are generally considered to be variations on a scheme originally presented by Lax and Wendroff.⁶⁶ Each of these schemes is subject to the same stability limitation, as given by Eq. 3.45, as the Lax method.⁴⁹ The original Lax-Wendroff scheme is two level, but is somewhat complicated. Richtmyer⁶⁷ proposed an equivalent but simpler two-step, three-level scheme. Richtmyer's method gives a useable solution only at alternate points on the space mesh and only on alternate time steps, so a variation developed by Burstein⁶⁸ has been chosen for use in the simulation program. In this method, the transport equations are considered as a single-vector partial-differential equation:

$$\frac{\partial \bar{f}}{\partial t} = - \frac{\partial \bar{\Phi}}{\partial x} . \quad (3.48)$$

Equations 3.20 through 3.22 can be considered to be in the form of Eq. 3.48 if the variable coefficients of the space derivatives in Eqs. 3.21 and 3.22 are treated as constants across each time step.

The first step in Burstein's method uses the Lax method to find a trial solution at the half time and half space step:

$$\bar{f}_{j+\frac{1}{2}}^{t+\Delta t/2} = \frac{1}{2}(\bar{f}_{j+1}^t + \bar{f}_j^t) - \frac{\Delta t}{2\Delta x}(\bar{\Phi}_{j+1}^t - \bar{\Phi}_j^t) . \quad (3.49)$$

The second step uses these centered values to evaluate $\bar{\Phi}$ and advance the solution across a full time step:

$$\bar{f}_j^{t+\Delta t} = \bar{f}_j^t - \frac{\Delta t}{\Delta x}(\bar{\Phi}_{j+\frac{1}{2}}^{t+\Delta t/2} - \bar{\Phi}_{j-\frac{1}{2}}^{t+\Delta t/2}) . \quad (3.50)$$

Burstein's method is stable provided Eq. 3.45 is satisfied, and it introduces little spurious diffusion. Its usefulness is obtained

at the cost of sacrificing the transportive property of upwind drift and of increased computational effort in comparison to a one-step scheme. Space centered differencing does give some advantage in terms of program simplicity because it requires no special treatment of velocity reversals.

3.2.1.6 Other Schemes. It should be noted that methods other than the Lax and Lax-Wendroff types may be applicable to Eqs. 3.20 through 3.22. Richtmyer⁶⁹ describes a two time level scheme for the hydrodynamic equations which advances u in time before it does n and w, but he gives an apparently erroneous stability analysis. It is unclear whether this scheme would adapt successfully to the transport equations used in this work. No implicit scheme has achieved any significant degree of acceptance among fluids simulators,⁴⁹ though a workable one has been developed by Polezhaev.⁷⁰ This scheme is unfortunately only applicable to "supersonic" flow, in which u is greater than the square-root quantity in Eq. 3.45. Several other implicit schemes have been tried on the computer in the course of the present work. None was found to be reasonably accurate and to have greater stability than the Burstein method.

3.2.2 Source and Relaxation Terms.

3.2.2.1 Carrier Generation and Electric Field Terms. The impact ionization term represents exponential growth of the carrier concentration, with growth rate α or β (unnormalized). In the simulation of millimeter-wave devices, the product of growth rate and time step is much less than one, so a first-order approximation of the exponential growth is sufficiently accurate:

$$G^t = \alpha n^t + \beta p^t . \quad (3.51)$$

In the simulation of microwave devices, the time step can become large enough that a second-order treatment of generation is required,³⁸ but this will ordinarily occur only in situations where the static transport model is adequate for describing device behavior.

The terms containing the electric field in the energy and momentum transport equations are evaluated at present time. The coupling of the field terms to space-charge density through Poisson's equation introduces restrictions concerning the dielectric relaxation time and the Debye length. Preventing numerical overshoot of the charge concentration in low-field regions requires that Δt be shorter than the dielectric relaxation time,³⁸ but this is usually less restrictive than Eq. 3.45 when Δx is chosen for reasonable spatial resolution in a millimeter-wave device. The device boundaries are not described with precision when Δx is greater than the Debye length, which can be on the order of 10^{-7} cm in contact regions, but, as shown by results given in Chapter IV, little is gained in the description of overall device behavior by making Δx so small.

3.2.2.2 Relaxation Terms. The relaxation terms represent exponential decay of u and w . Both the energy and momentum equations have the form

$$\frac{\partial f}{\partial t} = S - \frac{f}{\tau} , \quad (3.52)$$

where S is a "source" term representing the influences of the field and space derivative terms. The exact solution of Eq. 3.52 is

$$f(t + \Delta t) = [f(t) - S\tau] e^{-\Delta t/\tau} + S\tau . \quad (3.53)$$

The simplest finite-difference approximation to Eq. 3.52 is first order in time, having the decay term evaluated at time t , giving

$$f_1^{t+\Delta t} = f_1^t + S\Delta t - \frac{f_1^t}{\tau} \Delta t . \quad (3.54)$$

Bosch and Thim⁵¹ used an energy and momentum conserving model to simulate the operation of transferred electron devices. They used a second-order, present-time form of the decay term, which gives

$$f_2^{t+\Delta t} = (f_2^t - S\tau) \left[1 - \frac{\Delta t}{\tau} + \frac{1}{2} \left(\frac{\Delta t}{\tau} \right)^2 \right] + S\tau . \quad (3.55)$$

Another possibility is to perform first-order evaluation of the decay term at advanced time, which still gives an explicit solution. The first-order, advanced-time approximation to Eq. 3.52 is

$$f_3^{t+\Delta t} = f_3^t + S\Delta t - \frac{f_3^{t+\Delta t}}{\tau} \Delta t = \frac{f_3^t + S\Delta t}{1 + (\Delta t/\tau)} . \quad (3.56)$$

Setting S to zero in Eqs. 3.53 through 3.56 gives the behavior in each of any numerical error which may be present at the beginning of the time interval. Error is plotted in Fig. 3.1 as a function of $\Delta t/\tau$ for each of the forms in Eqs. 3.53 through 3.56. The figure shows that stability of f_1 and f_2 requires Δt be less than twice the relaxation time because the magnitude of error in these two approximations grows if this limit is exceeded. This would be a severe restriction on Δt in actual simulations, since the momentum relaxation time in Si can be less than a hundredth of a picosecond. No such time-step restriction applies to f_3 , so it has been chosen for use in the diode simulation program. f_3 has the additional advantage of being in agreement with $f(t)$ as given by Eq. 3.53 in the limit of large Δt . This is not true of f_1 or f_2 .

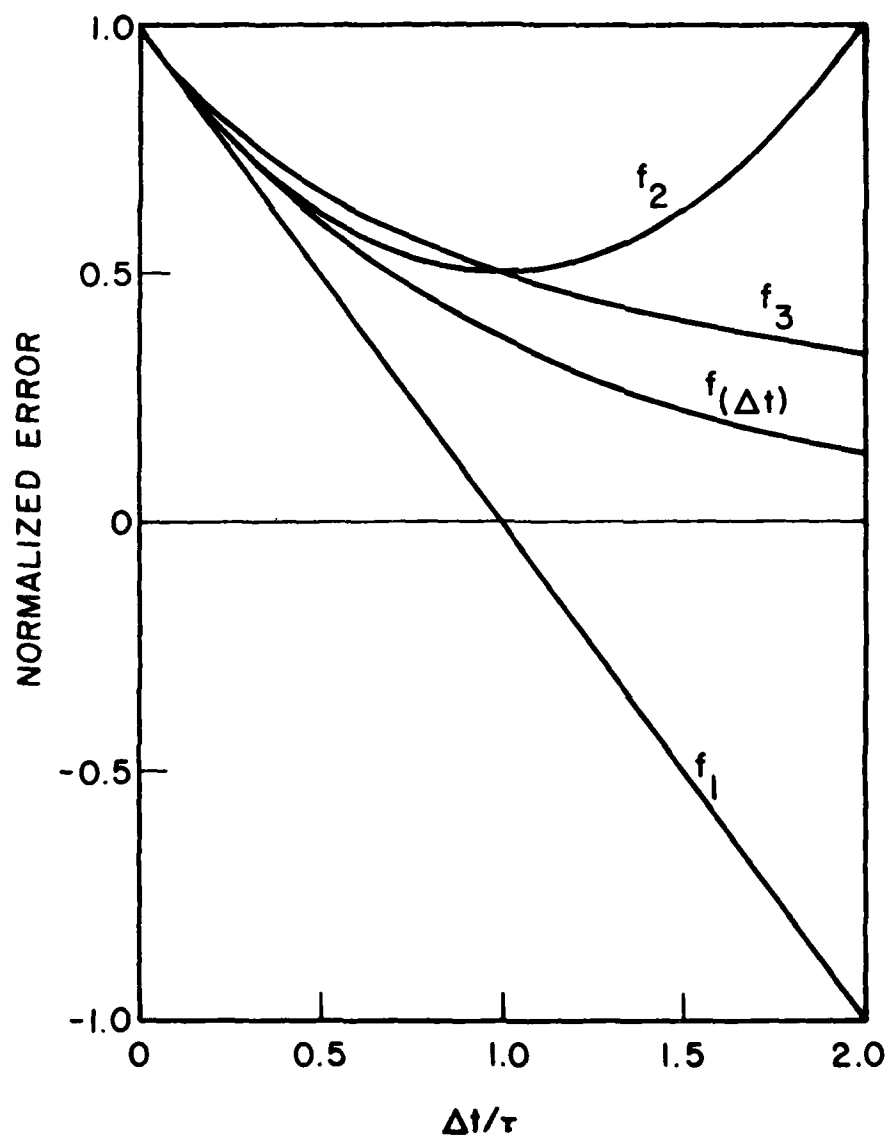


FIG. 3.1 NUMERICAL ERROR VS. TIME STEP LENGTH FOR VARIOUS FORMS OF THE DECAY EQUATION. [$f(\Delta t)$: EXACT; f_1 : FIRST ORDER, PRESENT TIME; f_2 : SECOND ORDER, PRESENT TIME; f_3 : ADVANCED TIME]

Advanced-time relaxation can also improve the stability which is associated with a numerical form of the spatial derivative terms. This can be seen by examining its effect on the amplification matrix. With the inclusion of source terms and advanced-time relaxation in the transport equations, Eq. 3.28 becomes

$$\bar{\epsilon}_m^{t+\Delta t} = [R]([I] + [G_m])\bar{\epsilon}_m^t, \quad (3.57)$$

where R is a relaxation matrix given by

$$[R] = \begin{bmatrix} 1 & 0 & 0 \\ 0 & [1 + (1/\tau_v) + \beta(p/n)]^{-1} & 0 \\ 0 & 0 & [1 + (1/\tau_w) + \beta(p/n)]^{-1} \end{bmatrix}. \quad (3.58)$$

Since the diagonal elements of [R] are less than or equal to one, the magnitudes of the eigenvalues of the right-hand side of Eq. 3.58 are smaller than the magnitudes of the eigenvalues of [I] + [G_m] alone. If the latter are not significantly greater than one, use of advanced-time relaxation can stabilize a method which is otherwise unstable.

Equation 3.37 for the eigenvalues associated with the numerical method given by Eqs. 3.23 through 3.25 indicates that keeping the eigenvalue magnitudes close to one requires that normalized u and w be sufficiently small. This in turn requires that $\Delta x/\Delta t$ be small, so that the stability requirement for the method in Eqs. 3.23 through 3.25 with advanced-time relaxation amounts to a Courant-Friedrichs-Lewy condition. In practice, it has been found that the method is stable if $\Delta x/\Delta t$ is greater than approximately 5×10^7 cm/s and Δt is greater than approximately 0.02 ps.

3.2.2.3 Source and Relaxation Terms in Burstein's Method.

If requirements for spatial resolution dictate that Δx be extremely small, the CFL condition can require that Δt be so small that the normalized diagonal terms in the matrix $[R]$ in Eq. 3.58 approach one. If this happens, advanced-time relaxation will no longer provide numerical stabilization, and a Lax-Wendroff-type scheme for the spatial derivative terms in the transport equations must be used. Such schemes advance across a time step in two stages, so the question arises as to whether the source and relaxation terms should appear in both stages or whether the effects of these terms over a time step should be lumped into the second stage only. The latter approach has been followed in the present work. Conceptually, this treats the influences of the pressure and drift terms, and those of the source and relaxation terms, as acting in parallel across a time step, just as in a one-step scheme. The approach has been chosen for two reasons. First, the time-centered intermediate result obtained in the first step of a Lax-Wendroff scheme is not a "true" solution, but only an estimate upon which to base the second step. Evaluation of the source and relaxation terms should be done in terms of the genuine solution, which is not available as a time-centered quantity. Second, incorporation of source and relaxation terms only in the second step simplifies the method somewhat.

Burstein's method with source and relaxation terms in the second step can be represented as follows. The first step remains exactly as in Eq. 3.49, while the second step becomes

$$\bar{f}_j^{t+\Delta t} = [R](\bar{f}_j^t - \frac{\bar{f}_j^{t+\Delta t/2} - \bar{f}_{j+1}^{t+\Delta t/2}}{\Delta x} + \frac{\bar{f}_j^{t+\Delta t/2} - \bar{f}_{j-1}^{t+\Delta t/2}}{\Delta x} + \bar{S}) \quad , \quad (3.59)$$

where \bar{f} and $\bar{\Phi}$ are defined by Eq. 3.48, $[R]$ is the relaxation matrix given by Eq. 3.58, and \bar{S} is a vector representing the contribution of carrier generation and the electric field.

It has been found that the presence of source terms in Burstein's method can cause overshoot in the solution to occur near inflow boundaries. The overshoot can be eliminated by using an appropriate form of the two-step method. The sourceless carrier transport equation can be written in two numerical forms arising out of the compact and expanded forms of the spatial derivative term:

$$\frac{\partial n}{\partial t} = - \frac{\partial nu}{\partial x} \quad (3.60a)$$

and

$$\frac{\partial n}{\partial t} = - n \frac{\partial u}{\partial x} - u \frac{\partial n}{\partial x} \quad (3.60b)$$

In the continuum, there is no difference between Eqs. 3.60a and 3.60b. If their forms are carried through to the numerical method, they give rise to the following first steps in the method,

$$n_{j+\frac{1}{2}}^{t+\Delta t/2} = \frac{1}{2}(n_j^t + n_{j+1}^t) - \frac{1}{2}(n_{j+1}^t u_{j+1}^t - n_j^t u_j^t) \quad (3.61a)$$

and

$$\begin{aligned} n_{j+\frac{1}{2}}^{t+\Delta t/2} = & \frac{1}{2}(n_j^t + n_{j+1}^t) - \frac{1}{4}(n_j^t + n_{j+1}^t)(u_{j+1}^t - u_j^t) \\ & - \frac{1}{4}(u_j^t + u_{j+1}^t)(n_{j+1}^t - n_j^t) \quad (3.61b) \end{aligned}$$

and the following second steps,

$$n_j^{t+\Delta t} = n_j^t - n_{j+\frac{1}{2}}^{t+\Delta t/2} u_{j+\frac{1}{2}}^{t+\Delta t/2} + n_{j-\frac{1}{2}}^{t+\Delta t/2} u_{j-\frac{1}{2}}^{t+\Delta t/2} \quad (3.62a)$$

and

$$n_j^{t+\Delta t} = n_j^t - n_j^t(u_{j+\frac{1}{2}}^{t+\Delta t/2} - u_{j-\frac{1}{2}}^{t+\Delta t/2}) - u_j^t(n_{j+\frac{1}{2}}^{t+\Delta t/2} - n_{j-\frac{1}{2}}^{t+\Delta t/2}) \quad (3.62b)$$

In Eq. 3.21b the coefficients n and u of the space derivatives are centered at the half space step.

Equations 3.61a and 3.61b are numerically equivalent, but there is a difference between Eqs. 3.62a and 3.62b which gives rise to different overshoot properties. At the inflow boundary in an IMPATT, carrier concentration and velocity can both change rapidly in space because carriers enter the diode from a low-field region where they are minority carriers. Once inside, they accelerate and undergo impact ionization, and the resulting changes in n and u can be so rapid as to cause the right-hand side of Eq. 3.62a to be negative near the boundary, so that the carrier concentration overshoots past zero. Equation 3.62b contains cross products between n and u at different points in space, so the tendency to overshoot is much reduced.

3.3 Initial and Boundary Conditions

The transport equations determine their solution to within three sets of conditions: the initial conditions on the simulation variables throughout the space mesh, the boundary conditions on the simulation variables (usually defined at the edges of the mesh), and the relationship between terminal current and voltage which is determined by the interaction between the diode and its external circuit. This section discusses the forms and methods of application of these conditions in the simulation program.

3.3.1 Initial Conditions. The IMPATT simulation program is "stand alone" in the sense that it need not start from initial conditions provided by a dc solution to the transport equations. The program can either set up initial conditions following guidelines provided by the user, or it can start from the solution obtained at the last time step of a previous simulation run.

The use of an arbitrary starting condition which might never arise in the course of actual device operation might appear to be in contradiction to the transport equations, but any starting condition which does not overspecify the initial solution is mathematically possible. Experience with the simulation program has never turned up a situation in which an arbitrary set of starting conditions did not evolve rapidly toward a physically realistic solution as the simulation progressed. Care must only be taken to set the initial conditions so that the starting transient does not cause unrealistically large values of u or w to occur momentarily, since this can violate the condition of Eq. 3.45.

3.3.2 Spatial Boundary Conditions. Even though the transport equations are first order, centered differencing requires that boundary conditions be supplied at both ends of the space mesh. For this purpose a psuedo mesh point is established outside each end of the space mesh, and it is at these two points that the boundary conditions are applied. While many sets of boundary conditions are possible, one has been chosen for the majority of the present work which combines simplicity with a reasonable correspondence to the limited knowledge which exists concerning the conditions in the contact regions of an IMPATT under large-signal operation. At an inflow

boundary, a Dirichlet condition is applied to each unknown while at the outflow, a Neumann condition with constant slope is applied. The outflow condition is chosen to maximize the accuracy of the finite-difference scheme.⁴⁹ The Dirichlet inflow conditions are

$$n_b = \frac{n_i^2}{N_b}, \quad (3.63)$$

$$v_b = 0 \quad (3.64)$$

and

$$w_b = w_0, \quad (3.65)$$

where N_b is the doping concentration in the contact region. The inflow conditions describe the state of minority carriers in a region with zero electric field. They might seem to imply that no minority current can enter the device, but it is possible for a finite amount of minority current to cross the device boundary, which is located halfway between the pseudo point and the first actual mesh point. This current is small, and the bulk of the reverse saturation current is provided for by assuming a uniform rate of thermal generation throughout the device:

$$G_t = \frac{J_{sat}}{qL}, \quad (3.66)$$

where J_{sat} is the reverse saturation current density, and L is the device length. Some results with boundary conditions differing from Eqs. 3.63 through 3.65 are presented in Chapter IV.

3.3.3 The Device-Load Interaction. Updating the electric field at each time step requires that some relation between the terminal voltage and current be supplied. One way of doing this is to convolve the past values of current with the impulse response of an external circuit after every time step.⁷¹ This has the obvious drawback of requiring that many convolution integrals be evaluated in the course of a simulation. A simple way of centering the current in the upcoming time step using present terminal voltage exists,³⁸ but it does not allow the use of simple capacitive branches (such as an RF source with dc block) in the external circuit. Bauhahn and Haddad⁶⁴ imposed a sinusoidal RF voltage at the device terminals. While their method requires no circuit tuning or source adjustment in order to obtain a desired RF terminal voltage amplitude, it does require iteration on the dc voltage in order to obtain a desired dc current, and it does not allow the simulation of genuine transients in connection with realistic external circuits. A state space approach⁷² to the device-circuit interaction has been found to be the most useful in the present work.

The load routine used in the simulation program is designed to impose a sinusoidal RF voltage on the device terminals in a self-consistent manner. The circuit model used by the routine is shown in Fig. 3.2. The diode is represented by a particle current source J_p in parallel with the diode depletion capacitance C_d (normalized to unit area). The external circuit consists of a dc current source in parallel with an RF voltage source V_{RF} , series resistance R , and blocking capacitor C . The strength of J_p at any point in time can be found from

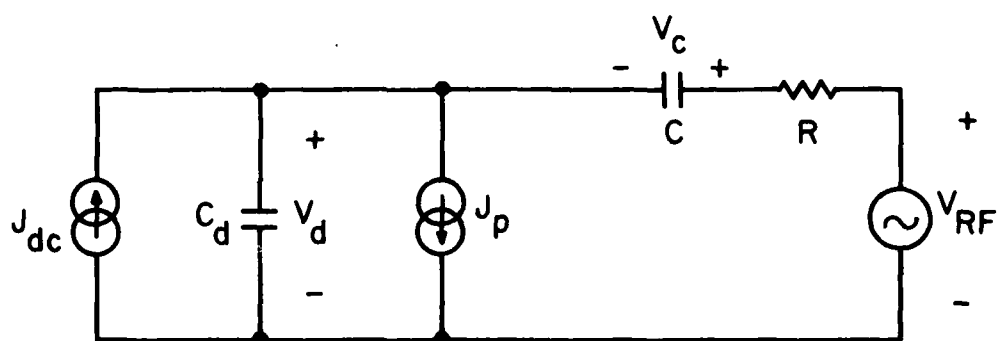


FIG. 3.2 CIRCUIT CONFIGURATION FOR DEVICE-LOAD INTERACTION.

$$J_p = \frac{1}{L} \int_0^L q(u_n n + u_p p) dx, \quad (3.67)$$

where L is the device length.

The time evolution of the blocking capacitor voltage V_c and the diode voltage V_d are given by

$$\frac{dV_c}{dt} = \frac{J}{C} \quad (3.68)$$

and

$$\frac{dV_d}{dt} = \frac{1}{C_d} (J + J_{dc} - J_p), \quad (3.69)$$

where

$$J = \frac{1}{R} (V_{RF} - V_c - V_d). \quad (3.70)$$

Integrating Eq. 3.68 and 3.69 across a time step using the trapezoidal rule gives an equation for V_c and V_d at the end of the time step:

$$\begin{bmatrix} 1 + \frac{\Delta t}{2RC} & \frac{\Delta t}{2RC} \\ \frac{\Delta t}{2RC_d} & 1 + \frac{\Delta t}{2RC_d} \end{bmatrix} \begin{bmatrix} V_c^{t+\Delta t} \\ V_d^{t+\Delta t} \end{bmatrix} = \begin{bmatrix} 1 - \frac{\Delta t}{2RC} & -\frac{\Delta t}{2RC} \\ -\frac{\Delta t}{2RC_d} & 1 - \frac{\Delta t}{2RC_d} \end{bmatrix} \begin{bmatrix} V_c^t \\ V_d^t \end{bmatrix} + \frac{\Delta t}{2} \begin{bmatrix} \frac{1}{RC} (V_{RF}^{t+\Delta t} + V_{RF}^t) \\ \frac{1}{RC_d} (V_{RF}^{t+\Delta t} + V_{RF}^t) + \frac{1}{C_d} (2J_{dc} - J_p^{t+\Delta t} - J_p^t) \end{bmatrix}. \quad (3.71)$$

In Eq. 3.71, $J_p^{t+\Delta t}$ is known from Eq. 3.67.

If the external series resistance R is chosen to be zero, the time evolution of the diode voltage is given by Eq. 3.69, with

$$J = C \frac{d}{dt} (V_{RF} - V_d) . \quad (3.72)$$

With the use of trapezoidal rule, Eqs. 3.69 and 3.72 give

$$V_d^{t+\Delta t} = V_d^t + \left[\frac{\Delta t}{2} (2J_{dc} - J_p^t - J_p^{t+\Delta t}) + C(V_{RF}^{t+\Delta t} + V_{RF}^t) \right] / (C + C_d) \quad (3.73)$$

when the series resistance is zero.

The form of the circuit in Fig. 3.2 is such as to suppress unwanted harmonic components of the terminal voltage. Bias oscillations⁷³ and subharmonic instabilities⁷² can usually be prevented by choosing an appropriate ratio between C and C_d . The series resistance serves to damp out transients more quickly than they would otherwise decay. Usually, a particular steady-state RF voltage amplitude is desired at the device terminals. The terminal amplitude will differ somewhat from that of the RF voltage source, but can be brought to the desired value by adjustment of the source amplitude.

3.4 Conclusions

Development of an IMPATT simulation program based on finite-difference approximations to the energy and momentum conserving transport equations requires careful choice of the numerical methods used. The methods described in this chapter are efficient and accurate solutions to the numerical problems associated with various parts of the transport equations.

Explicit finite-difference schemes incorporating forward-time differences are likely to be unstable in the limit of very

short time steps. The Lax method has a well-defined stability requirement which is acceptable from the point of view of efficiency, but the method introduces an undesirably large amount of numerical diffusion. This diffusion can be substantially eliminated, without sacrificing stability, by the use of a scheme of the Lax-Wendroff type.

Both the first- and second-order present-time forms of the relaxation terms impose a severe stability restriction on the time step. The first-order advanced-time form imposes no such restriction, and its asymptotic behavior is the same as that of the exponential decay process which has been used to model the effects of collisions.

The simulation program makes use of initial and boundary conditions which are simple, stable, and consistent with reasonable assumptions about the conditions which occur in an actual device.

CHAPTER IV. SIMULATION OF MILLIMETER-WAVE IMPATT OPERATION

This chapter presents results of several series of investigations which have been performed using the simulation program described in the preceeding chapter. The first section presents dc and large-signal results for situations of electric field with very small spatial variation. These results permit clear identification of certain overshoot and relaxation phenomena which are present, but less clearly identifiable, in simulations of more realistic IMPATT structures. The results also demonstrate the appropriateness of certain assumptions made in Chapter II. In Section 4.2 results obtained using the energy and momentum conserving simulation are compared with results obtained using conventional drift-diffusion simulation for the same situations. Systematic differences are observed and discussed.

Sections 4.3 and 4.4 are concerned with numerical experiments to establish the importance of particular physical mechanisms to overall device behavior. Section 4.3 is concerned with carrier-inflow boundary conditions and considers the effects of highly doped contact regions and injection of "hot" carriers at boundaries. Section 4.4 examines the effects of the cooling of each carrier distribution due to impact ionization initiated by the other carrier type.

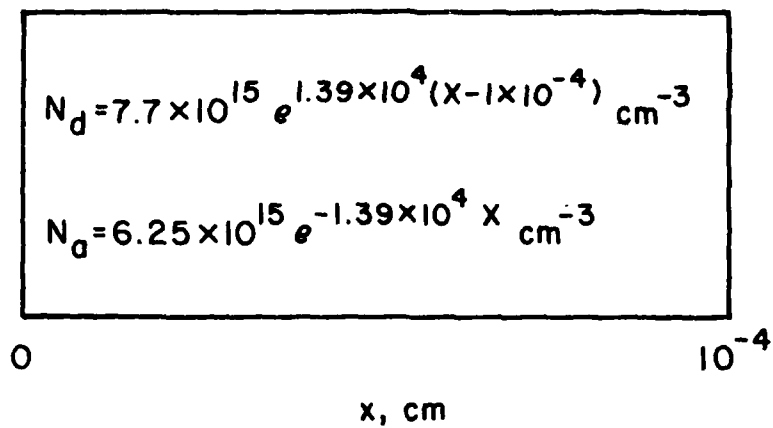
Section 4.5 is concerned with the implications of the present study for the potential performance of millimeter-wave Si IMPATTs.

Performance limitations due to nonstatic carrier transport phenomena and to parasitics external to the active diode are discussed. A criterion for estimating the upper frequency limit for useful operation of the IMPATT mode in any material is explained; this upper limit is estimated to be approximately 500 GHz for Si IMPATTs.

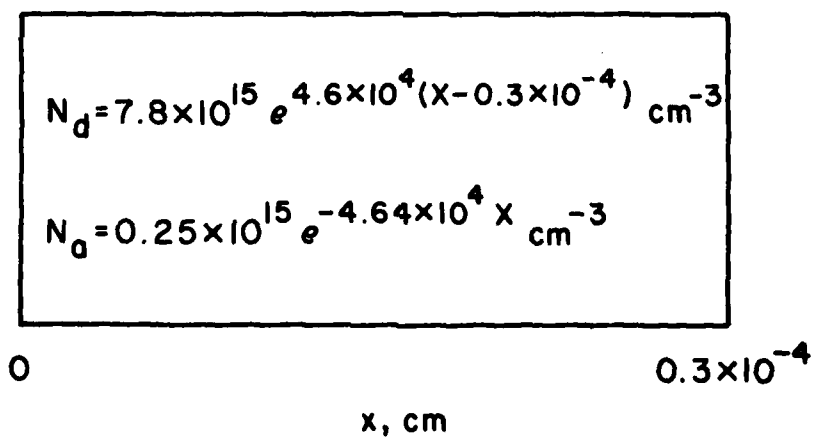
4.1 "Flat Field" Results

Simulation of pn junction devices with spatially uniform electric field in avalanche breakdown is useful for gaining an understanding of the behavior of the solution of the energy and momentum transport equations in the presence of time and space variations of the electric field. With flat fields a dc solution shows the behavior of the transport quantities near a spatial field step (present at each spatial boundary) in the absence of temporal variations. A large-signal solution shows the behavior, away from the spatial boundaries, of the transport quantities under time-varying, spatially uniform conditions. The responses to spatial and temporal variation of the field can thus be observed separately.

Simulation results have been obtained for flat-field situations in devices 1 and 0.3 μm long, the doping profiles of which are shown in Fig. 4.1. The doping densities are chosen to approximately compensate the space charge of mobile carriers at a dc bias current density of 10^4 A/cm^2 . Figures 4.2 and 4.3 show dc carrier concentration, current density, average velocity, average energy, and electric field profiles for the two devices. The conventions used in the figures are used in all results presented in this chapter: positive electric field and hole velocity are taken from right to left, and positive electron velocity from left to right. Electrons



(a)



(b)

FIG. 4.1 DOPING PROFILES FOR (a) 1 μm AND (b) 0.3 μm
DIODES WITH SPATIALLY CONSTANT FIELD.

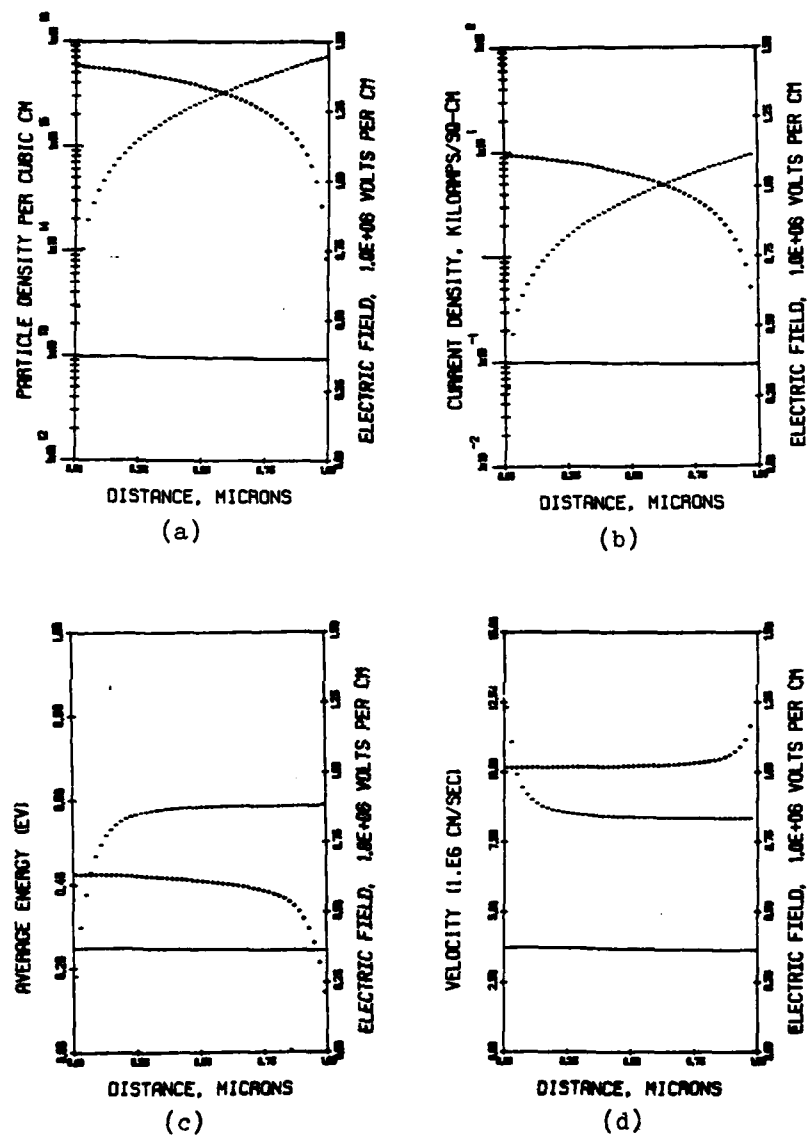


FIG. 4.2 ELECTRIC FIELD (SOLID LINES) AND CONCENTRATION, CURRENT DENSITY, AVERAGE ENERGY, AND AVERAGE VELOCITY FOR ELECTRONS (MINUS SIGNS) AND HOLES (PLUS SIGNS) IN THE 1- μ m, FLAT FIELD DIODE UNDER DC CONDITIONS. ($J_{dc} = 10^4$ A/cm²)

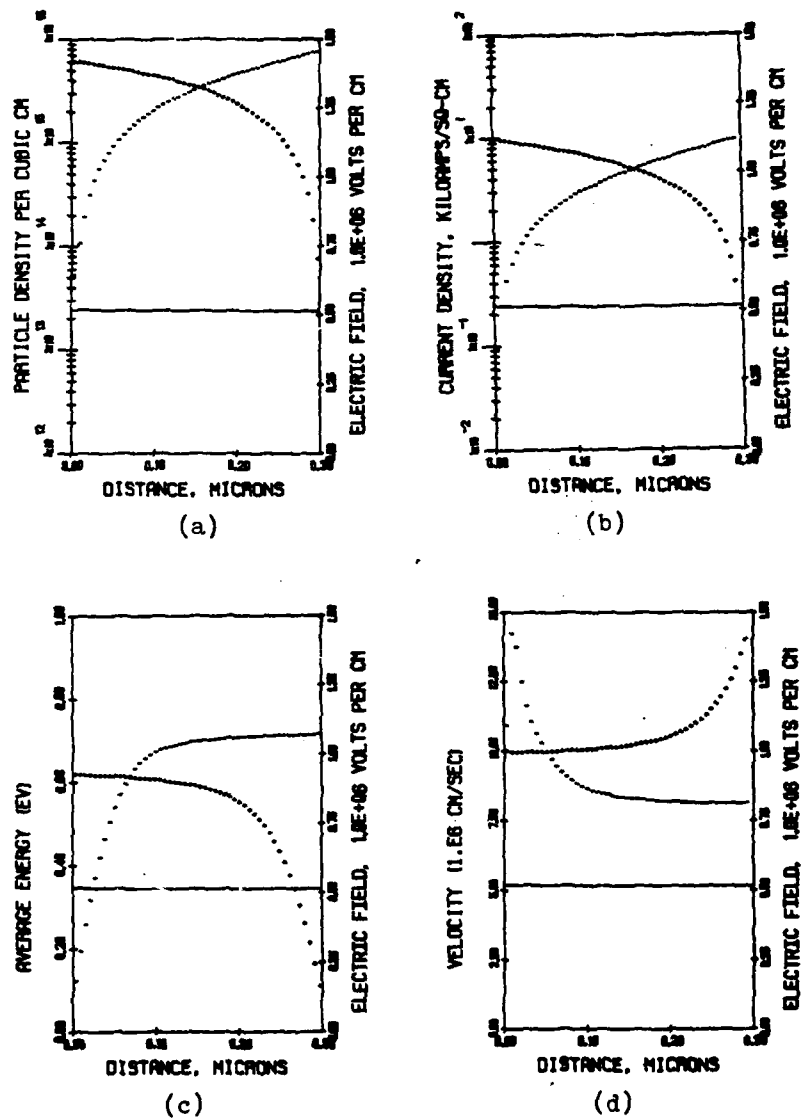


FIG. 4.3 ELECTRIC FIELD (SOLID LINES) AND CONCENTRATION, CURRENT DENSITY, AVERAGE ENERGY, AND AVERAGE VELOCITY FOR ELECTRONS (MINUS SIGNS) AND HOLES (PLUS SIGNS) IN THE 0.3- μ m, FLAT FIELD DIODE UNDER DC CONDITIONS. ($J_{dc} = 10^4$ A/cm 2)

enter each device from the left-hand boundary with concentration, average velocity, and average energy as described in Chapter III; holes enter from the right.

The electron and hole concentrations in the figures increase monotonically as the carriers traverse each device. This is the usual situation in a pn junction under reverse breakdown. The velocity profiles show that the velocities overshoot their conventional "saturated" values as carriers enter each device, approaching the conventional values only after the carriers have traveled some distance past the inflow boundary. These velocity overshoots are opposed rather than assisted by diffusion down the carrier concentration gradients. Carrier energy is low at inflow boundaries and substantially "catches up" to the field over the velocity overshoot distance. Once they have reached equilibrium with the field, velocity and energy do not change through the remainder of the device length, even though there is a concentration gradient present. This is in accordance with the assumption of "uniform" conditions which was made in Chapter II.

Velocity overshoots similar to those shown in Figs. 4.2 and 4.3 will be present in all of the energy and momentum conserving results presented in this chapter. The overshoots occur when carriers enter the depletion region of a reverse-biased diode. In doing so, they pass through an abrupt step in field strength, since the inflow boundary conditions approximate conditions in a low-field region. Immediately downstream of the step in field, the carriers have lower average energy than they would have in equilibrium with the field. At lower energy the electron and hole relaxation times are

AD-A122 901

COMPUTER MODELING OF MILLIMETER-WAVE IMPATT DIODES ONE
OF A SERIES OF REP. (U) MICHIGAN UNIV ANN ARBOR
ELECTRON PHYSICS LAB R K FROELICH NOV 82 TR-158
AFWAL-TR-82-1107 F33619-81-K-1429

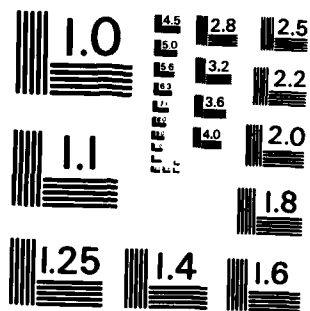
2/2

UNCLASSIFIED

P/O 9/2

NL

END
DATE
FILMED
2 83
DTIC



MICROCOPY RESOLUTION TEST CHART
NATIONAL BUREAU OF STANDARDS - 1963 - A

longer, so the relaxation terms in the velocity transport equations become smaller, and velocity overshoot results.

The figures suggest that the carrier velocities respond much more quickly to changes in the field than do the carrier energies. Each energy can be seen to require some distance over which to build up in response to the inflow field step. In contrast, the corresponding velocity overshoots almost immediately, and the distance over which the overshoot extends corresponds to that over which the energy is increasing. This indicates that velocity transients are due primarily to the energy dependence of the velocity relaxation times. The situation of low energy and velocity overshoot which occurs at each inflow boundary in Figs. 4.2 and 4.3 will be referred to as spatial lag, i.e., the lagging of energy behind a spatial variation in the electric field.

Figures 4.4 and 4.5 show profiles of electric field, average energy, and average velocity in the 1- μ m flat-field device at various points in a large-signal RF cycle. The RF terminal voltage is sinusoidal with a frequency of 300 GHz and an amplitude of 15 V, which is just under half the dc bias voltage of 32 V. The figures show conditions inside the device at 0-, 90-, 180- and 270-degree phase in the RF cycle, the phase angles at which the RF terminal voltage or its time derivative reaches an extremum. These figures show evidence of spatial lag near the contacts, just as did Figs. 4.2 and 4.3, but now the region of interest is the center of the device, where the energies and velocities can be seen to be spatially constant.

The carrier energies in Fig. 4.4 rise and fall under the influence of the electric field. Figure 4.5 shows that the velocities

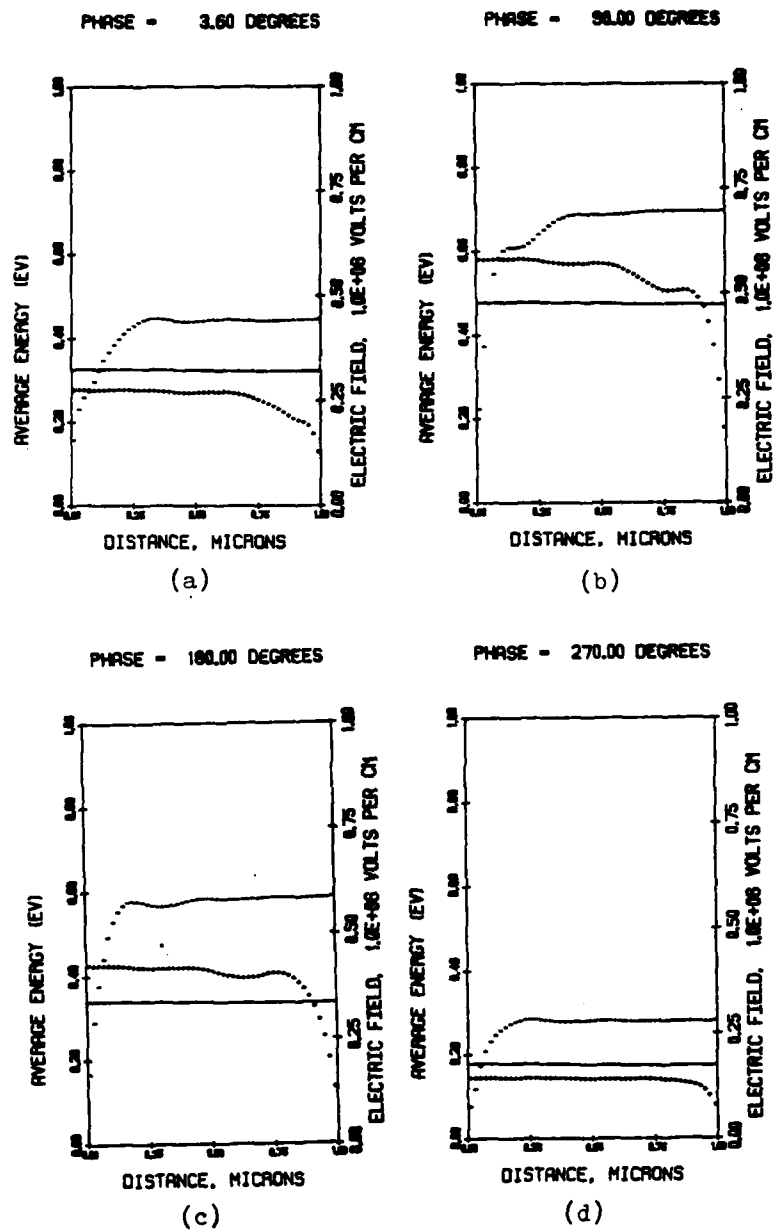


FIG. 4.4 ELECTRIC FIELD (SOLID LINES), ELECTRON ENERGY (MINUS SIGNS) AND HOLE ENERGY (PLUS SIGNS) IN THE 1-μm, FLAT FIELD DEVICE AT VARIOUS POINTS IN AN RF CYCLE. ($V_{RF} = 15$ V AND $J_{dc} = 10^4$ A/cm²)

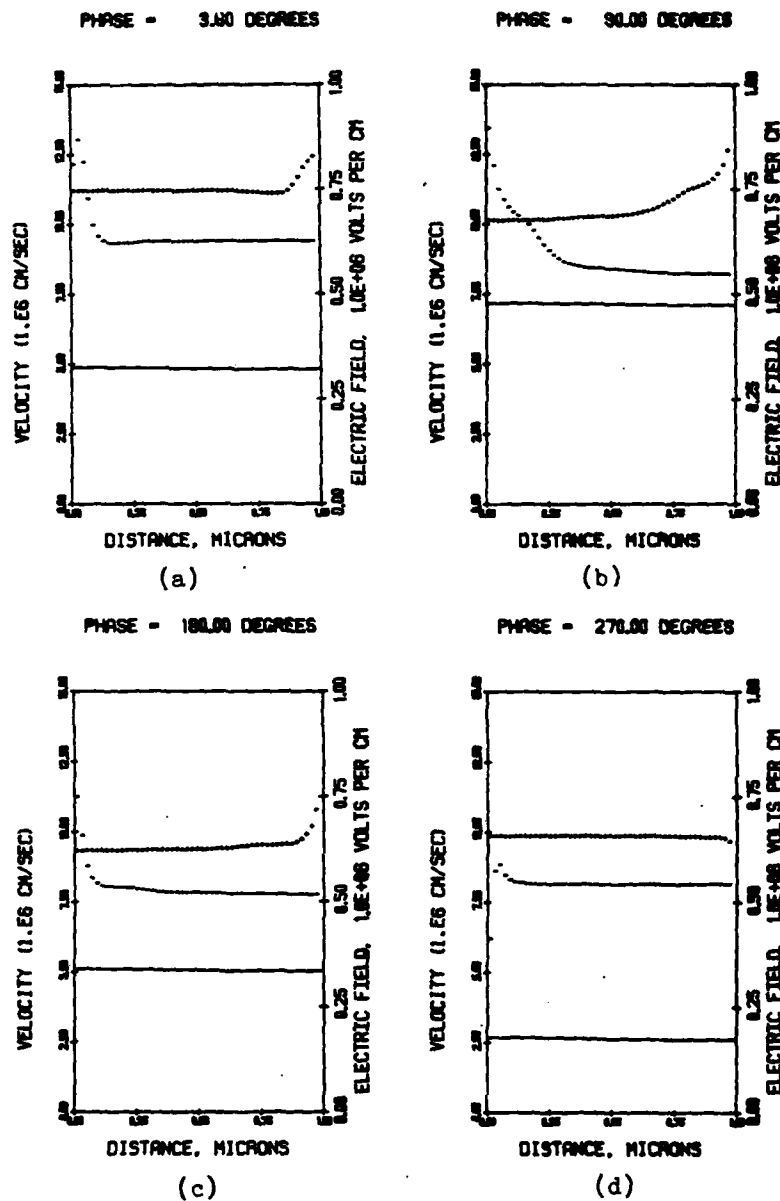


FIG. 4.5 ELECTRIC FIELD (SOLID LINES), ELECTRON VELOCITY (MINUS SIGNS) AND HOLE VELOCITY (PLUS SIGNS) IN THE 1-μm, FLAT FIELD DEVICE AT VARIOUS POINTS IN AN RF CYCLE. ($V_{RF} = 15$ V AND $J_{dc} = 10^4$ A/cm²)

depart from their saturated values of 10^7 cm/s and 8.5×10^6 cm/s for holes and electrons, respectively. The departures occur because of time lag between the local carrier energy and electric field. At the beginning of the cycle, field strength is increasing with time, so as energies lag behind the field the velocities overshoot for the reasons discussed in connection with Figs. 4.2 and 4.3. At 180 degrees, an inverse process takes place. The field strength at this point is decreasing with time, so the carrier energies, which lag behind, are larger than those which would occur in carrier-field equilibrium. At larger energies the momentum relaxation times are shorter, so the velocities undershoot their conventional saturated values. At 90 and 270 degrees the velocities return to their saturated values because the energies substantially "catch up" to the slowly changing field strength.

Further evidence for time lag between field strength and carrier energy is given by Fig. 4.6. This shows the carrier energies, carrier velocities, and field strength at the center of the 1- μ m flat-field device as functions of phase over one RF cycle. Time lag between the extrema of field and energy is apparent in the figure, as are the velocity overshoots and undershoots which occur in times of increasing or decreasing field strength. The time between an extremum in field and the corresponding one in energy is approximately 1 ps. The lag between carrier energy and temporal variation of the electric field will be referred to as temporal lag.

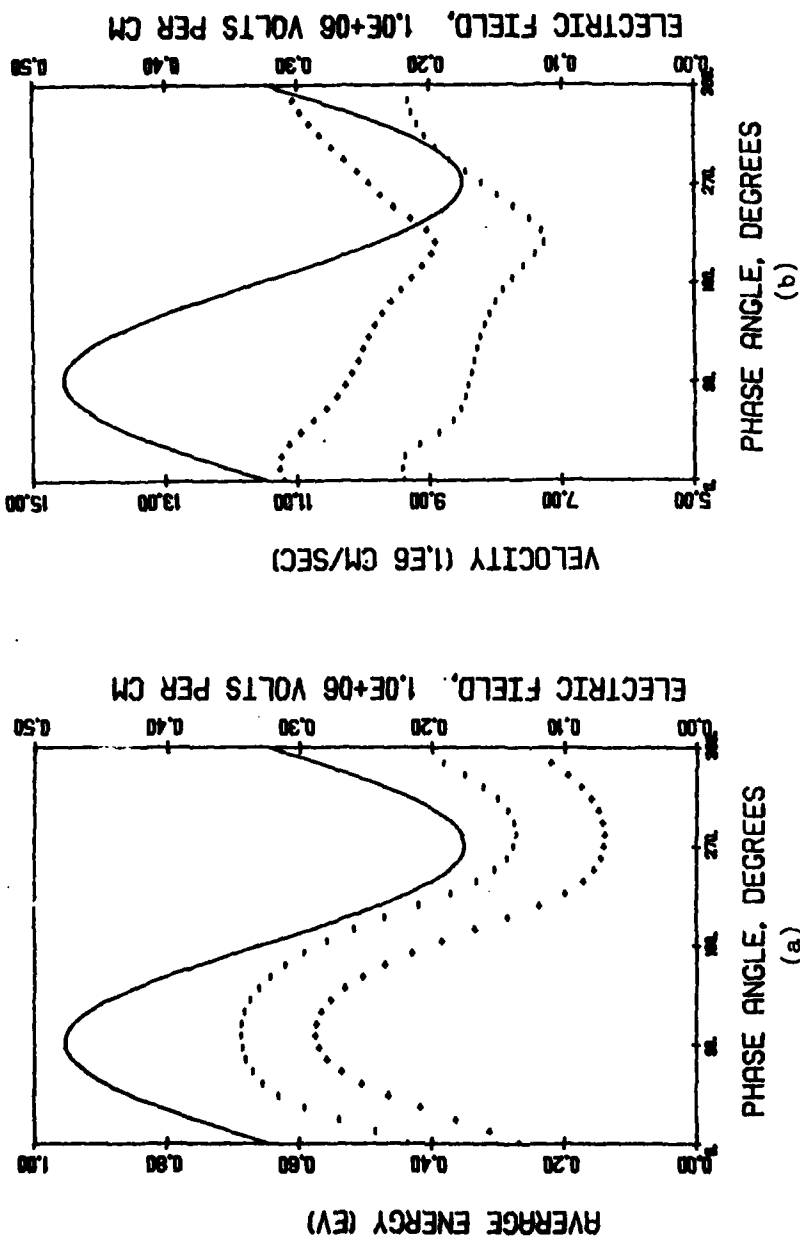


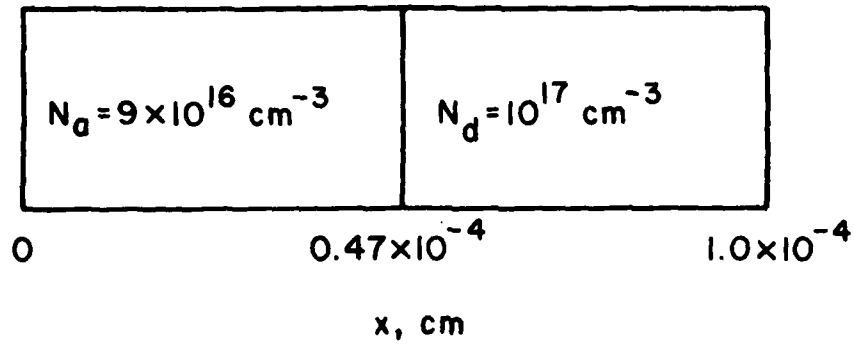
FIG. 4.6 ELECTRIC FIELD (SOLID LINES), ELECTRON ENERGY (MINUS SIGNS), ELECTRON VELOCITY (MINUS SIGNS), HOLE ENERGY (PLUS SIGNS) AND HOLE VELOCITY (PLUS SIGNS) AT THE CENTER OF THE 1- μ m, FLAT FIELD DEVICE VS. RF PHASE ANGLE. ($V_{RF} = 15$ V AND $J_{dc} = 10^{-4}$ A/cm²)

4.2 Comparisons Between Conventional and Energy and Momentum

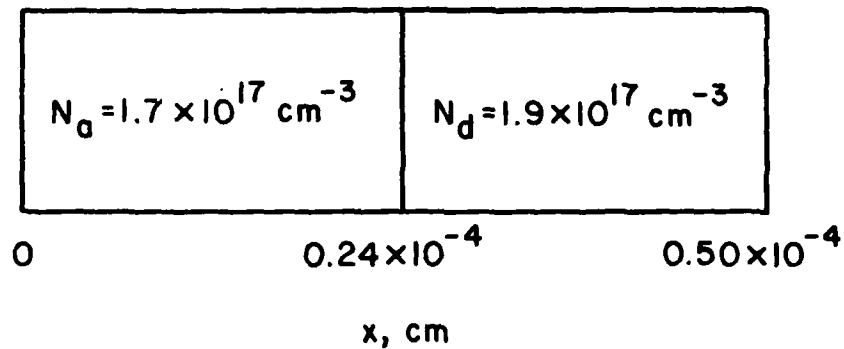
Conserving Results

The results described in the preceeding section indicate that spatial and temporal lag between carrier energy and electric field strength occur in results from simulation based on the energy and momentum conserving transport model. This lag is not accounted for in conventional simulation based on drift and diffusion, so the nature and degree of its effect on IMPATT operation can be determined by comparing results from conventional simulation⁶⁴ with those from energy and momentum conserving simulation. Comparisons have been made for three double-drift IMPATT structures with lengths of 1, 0.5, and 0.3 μm . The three doping profiles are shown in Fig. 4.7. They were chosen so that the devices will be strongly punched through at breakdown, and so that the electron and hole drift transit times will be approximately equal in each device. The conventional drift velocities, ionization rates, and diffusion coefficients used are given in Appendix A and Fig. 2.4.

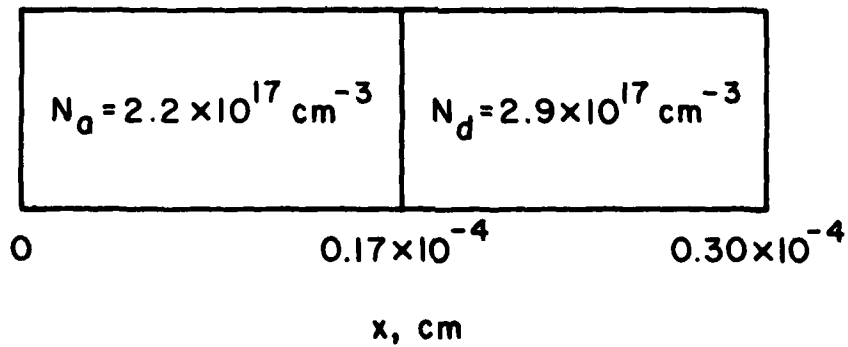
Figures 4.8, 4.9, and 4.10 show large-signal admittance results from the two types of simulation for the 1-, 0.5- and 0.3- μm structures, respectively. Table 4.1 lists a number of representative operating characteristics. There is very little difference between the sets of data for the 1- μm structure. A consistent difference between corresponding admittance data points can be seen in the case of the 0.5- μm structure; and in the case of the shortest structure, this difference is more pronounced. Apparently the extra physical effects allowed for in the energy and momentum conserving transport model have a significant effect on the operation of



(a)



(b)



(c)

FIG. 4.7 DOPING PROFILES FOR (a) 1- μm , (b) 0.5- μm
AND (c) 0.3- μm DOUBLE-DRIFT IMPATTS.

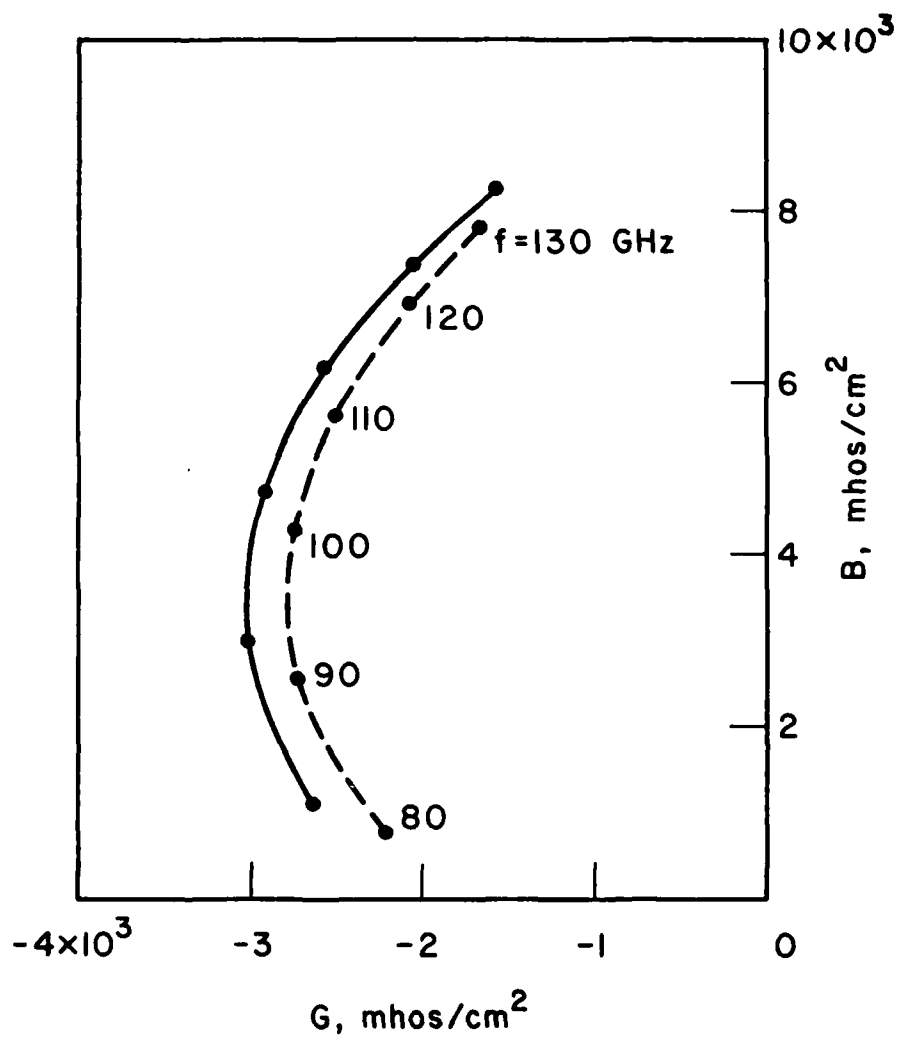


FIG. 4.8 ENERGY AND MOMENTUM CONSERVING (SOLID LINE) AND CONVENTIONAL (DASHED LINE) G-B RESULTS FOR THE $1\text{-}\mu\text{m}$ DOUBLE-DRIFT DEVICE. ($V_{\text{RF}} = 10 \text{ V}$ AND $J_{\text{dc}} = 6 \times 10^4 \text{ A}/\text{cm}^2$)

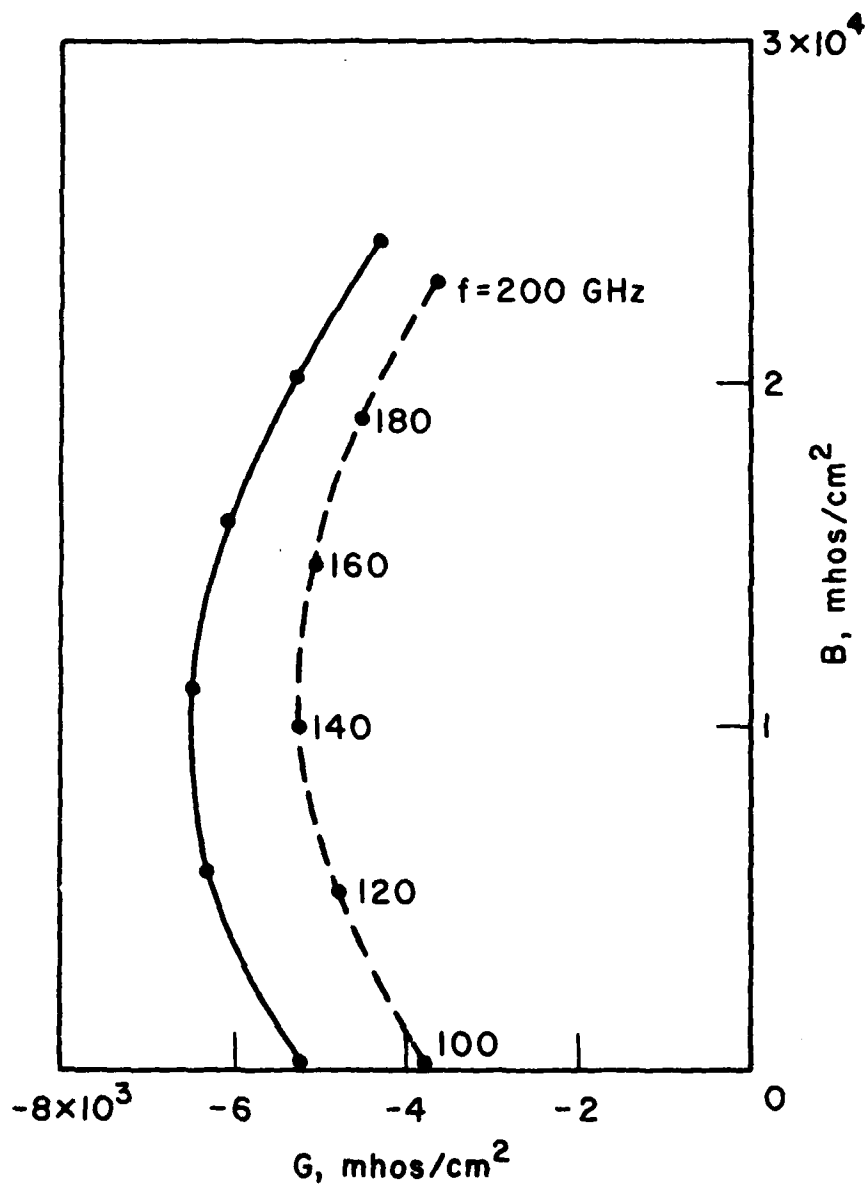


FIG. 4.9 ENERGY AND MOMENTUM CONSERVING (SOLID LINE)
AND CONVENTIONAL (DASHED LINE) G-B RESULTS
FOR THE $0.5\text{-}\mu\text{m}$ DOUBLE-DRIFT DEVICE.

($V_{RF} = 8 \text{ V}$ AND $J_{dc} = 10^5 \text{ A}/\text{cm}^2$)

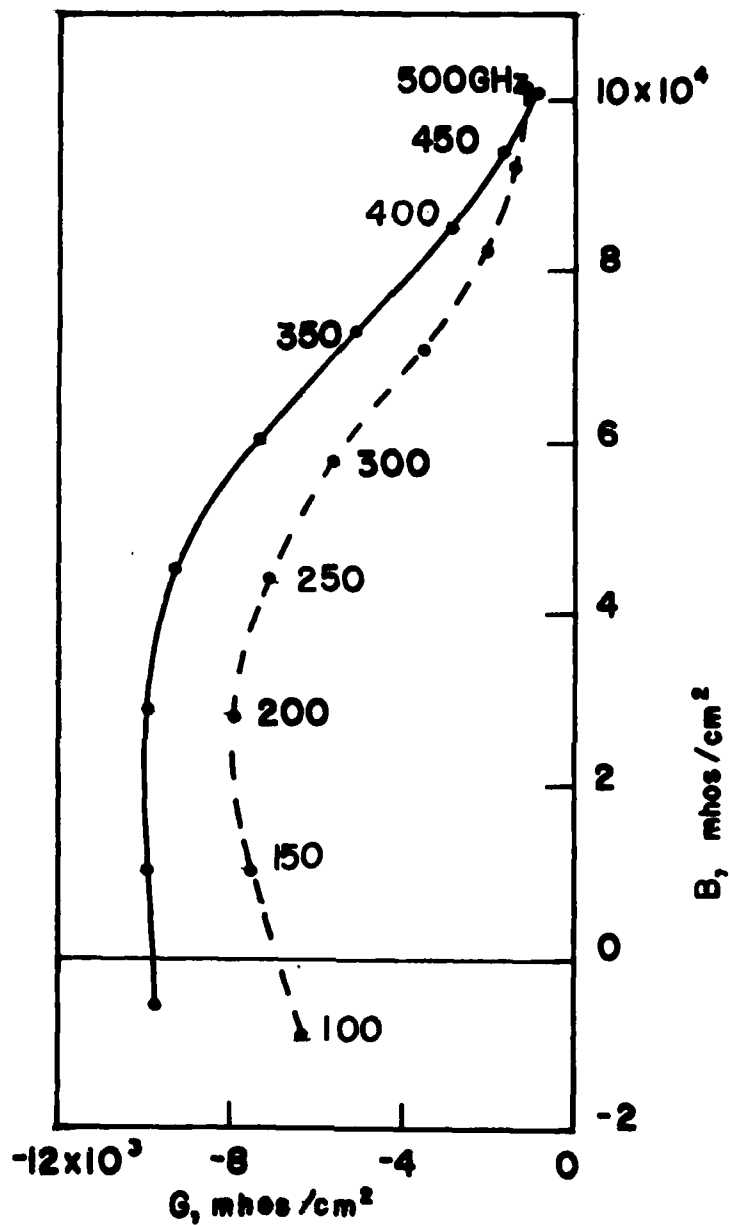


FIG. 4.10 ENERGY AND MOMENTUM CONSERVING (SOLID LINE) AND CONVENTIONAL (DASHED LINE) G-B RESULTS FOR THE $0.3\text{-}\mu\text{m}$ DOUBLE-DRIFT DEVICE. ($V_{\text{RF}} = 6 \text{ V}$ AND $J_{\text{dc}} = 1.5 \times 10^5 \text{ A}/\text{cm}^2$)

Table 4.1

Sample Results from Large-Signal Simulation

Device (μm)	J_{dc} (A/cm^2)	Frequency (GHz)	V_{RF} (V)	G (mhos/cm^2)	η (percent)	V_{dc}
1	6×10^4	100	10	$- 2.9 \times 10^3$ ($- 2.7 \times 10^3$)*	8.2 (7.8)*	30 (29.9)*
0.5	1×10^5	140	8	$- 6.5 \times 10^3$ ($- 5.3 \times 10^3$)	10.4 (8.4)	20.3 (19.9)
0.3	1.5×10^5	200	6	1.1×10^4 (8.1×10^3)	8.6 (6.3)	15.6 (15.0)

*Results from conventional simulations are shown in parenthesis.

double-drift Si IMPATTs for device lengths of approximately 0.5 μm or less.

The results in Table 4.1 show that the energy and momentum conserving simulation generally predicts larger dc voltage at a given operating point than does the conventional simulation. This is probably an effect of spatial lag. In the energy and momentum conserving simulation, the low energies at inflow boundaries result in lower rates of impact ionization than would be predicted by the conventional transport model. Lower rates near the boundaries must be compensated for by larger rates in the center of a device, requiring an increase in field strength and dc terminal voltage. The occurrence of spatial lag in a double-drift device is shown by Fig. 4.11, which gives energy, velocity, and field profiles in the 0.3- μm double-drift device under dc conditions. Carriers entering the device can be seen to undergo velocity overshoot.

The way in which the admittance results in Figs. 4.9 and 4.10 differ is initially surprising if one intuitively expects that the inclusion of higher order transport effects in an IMPATT model will result in poorer device performance. Where the results differ significantly, the energy and momentum conserving simulation consistently predicts larger negative conductance, though somewhat lower optimum frequency, than does the conventional simulation. There are several mechanisms which may tend to increase negative conductance. One of these is delay in the impact ionization process due to energy lag. This would cause carrier injection to occur later in the RF cycle. Another mechanism is velocity overshoot and undershoot on the part of drifting carriers. This might contribute to negative

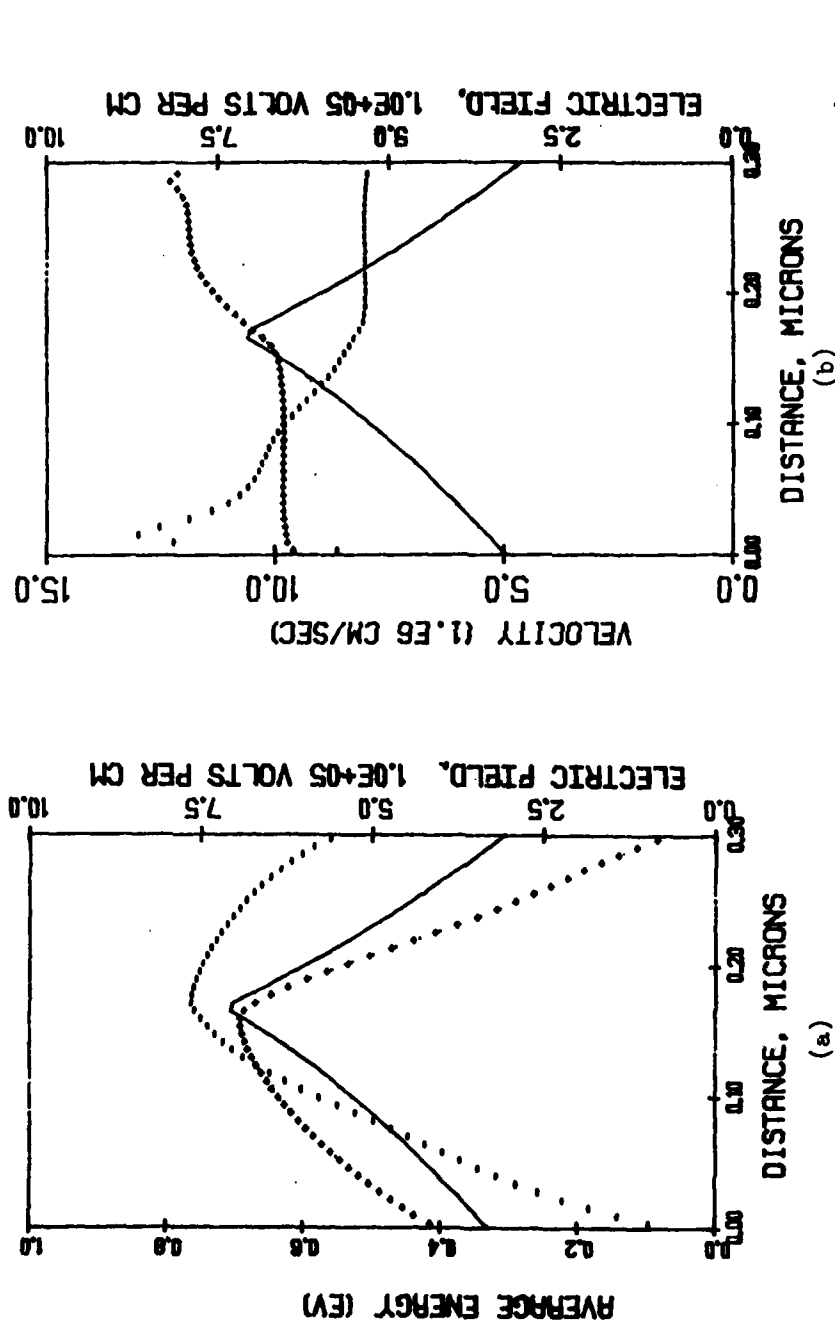


FIG. 4.11 ELECTRIC FIELD (SOLID LINES), ELECTRON ENERGY AND ELECTRON VELOCITY (MINUS SIGNS) AND HOLE ENERGY AND HOLE VELOCITY (PLUS SIGNS) IN THE 0.3- μ m DOUBLE-DRIFT DEVICE UNDER DC CONDITIONS. ($J_{dc} = 1.5 \times 10^5$ A/cm²)

conductance by giving the induced current waveform a more favorable shape, provided overshoot and undershoot were to occur at the proper points in the cycle. Changes in velocity might also affect the amount of time that carriers spend in the ionization region, thereby affecting the shape of the injected pulse.

Figures 4.12 through 4.16 provide insight into the mechanisms which cause increased negative conductance in the energy and momentum conserving results. The figures present simulation results from the 0.3- μm device operating at a frequency of 300 GHz with an RF amplitude of 10 V. Figure 4.12 is a set of plots of injected and induced current waveforms resulting from the two types of simulation. The sinusoidal terminal voltage is shown for phase reference. The injected current depicted in the figure is the integral over the device length of the instantaneous electron and hole generation rates, taken at each time step. The induced current is the component of terminal current which flows because of carrier motion in the interior of the device.

Figure 4.12 shows that the injected current waveforms are very similar in shape, but the injected current in the energy and momentum conserving result is delayed by approximately 10 degrees (or 0.1 ps) in comparison to the conventional result. A similar delay also appears in the plot of the terminal currents, along with some difference in shape. Injection delay tends to increase negative conductance and, by shortening the optimum transit angle, tends to lower the optimum IMPATT operating frequency. Figures 4.13 and 4.16 show profiles of carrier concentration, electric field, average velocity and average energy at four points in the RF

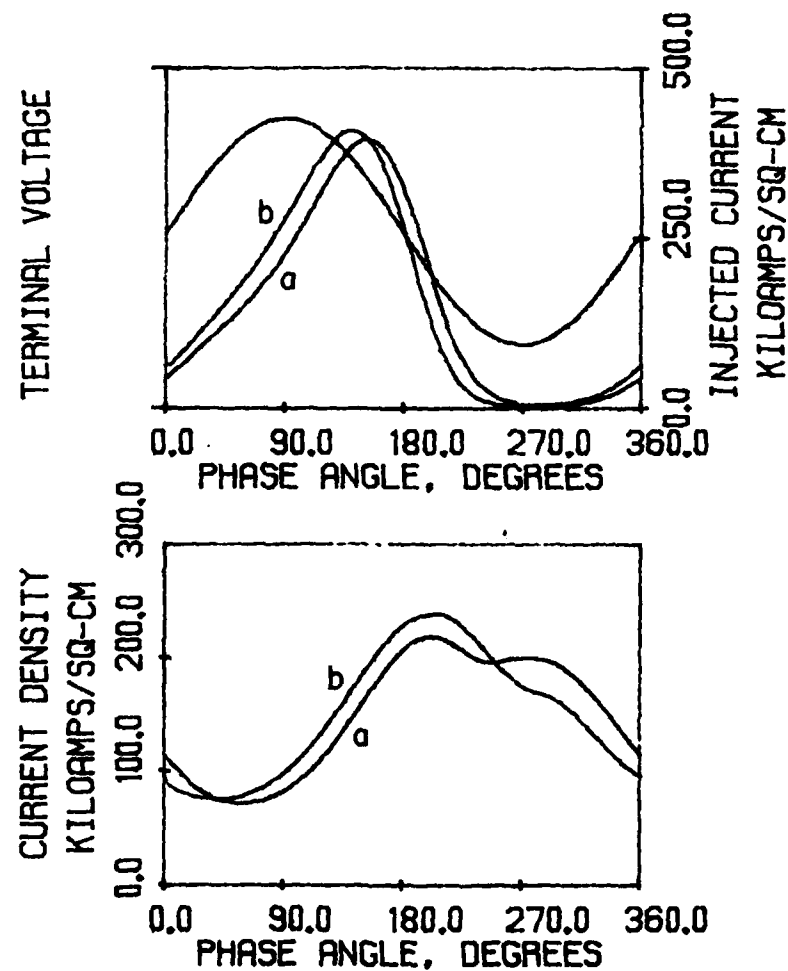


FIG. 4.12 TERMINAL VOLTAGE, INJECTED CURRENT, AND
INDUCED CURRENT WAVEFORMS FOR 0.3- μm
DOUBLE-DRIFT IMPATT. (a) ENERGY AND
MOMENTUM CONSERVING SIMULATION AND
(b) CONVENTIONAL SIMULATION. ($f = 300 \text{ GHz}$,
 $V_{\text{RF}} = 10 \text{ V}$ AND $J_{\text{dc}} = 1.5 \times 10^5 \text{ A/cm}^2$)

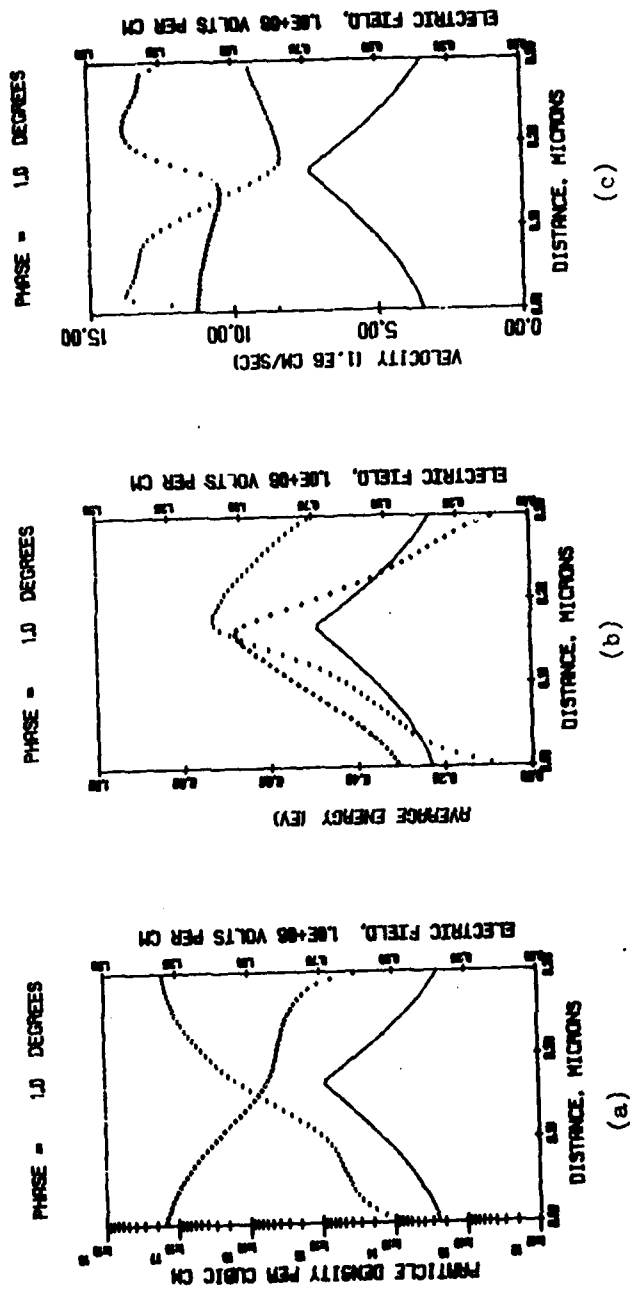
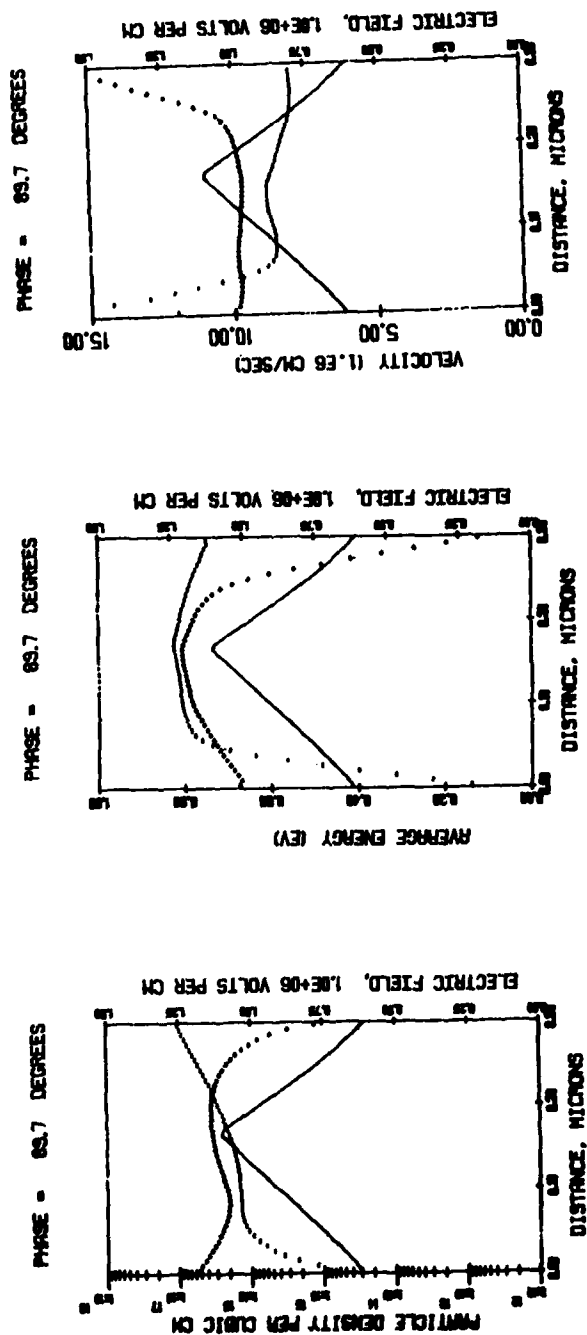


FIG. 4.13 ELECTRIC FIELD (SOLID LINES); ELECTRON DENSITY, ELECTRON ENERGY AND ELECTRON VELOCITY (MINUS SIGNS); HOLE DENSITY, HOLE ENERGY AND HOLE VELOCITY (PLUS SIGNS) VS. DISTANCE IN THE 0.3- μ m DOUBLE-DRIFT DEVICE NEAR ZERO DEGREES PHASE IN THE RF CYCLE SHOWN IN FIG. 4.12.



(a)

(b)

(c)

FIG. 4.14 ELECTRIC FIELD (SOLID LINES); ELECTRON DENSITY, ELECTRON ENERGY, AND ELECTRON VELOCITY (MINUS SIGNS); HOLE DENSITY, HOLE ENERGY AND HOLE VELOCITY (PLUS SIGNS) VS. DISTANCE

IN THE 0.3- μ m DOUBLE-DRIFT DEVICE AT 90 DEGREES PHASE IN THE RF CYCLE SHOWN IN FIG. 4.12.

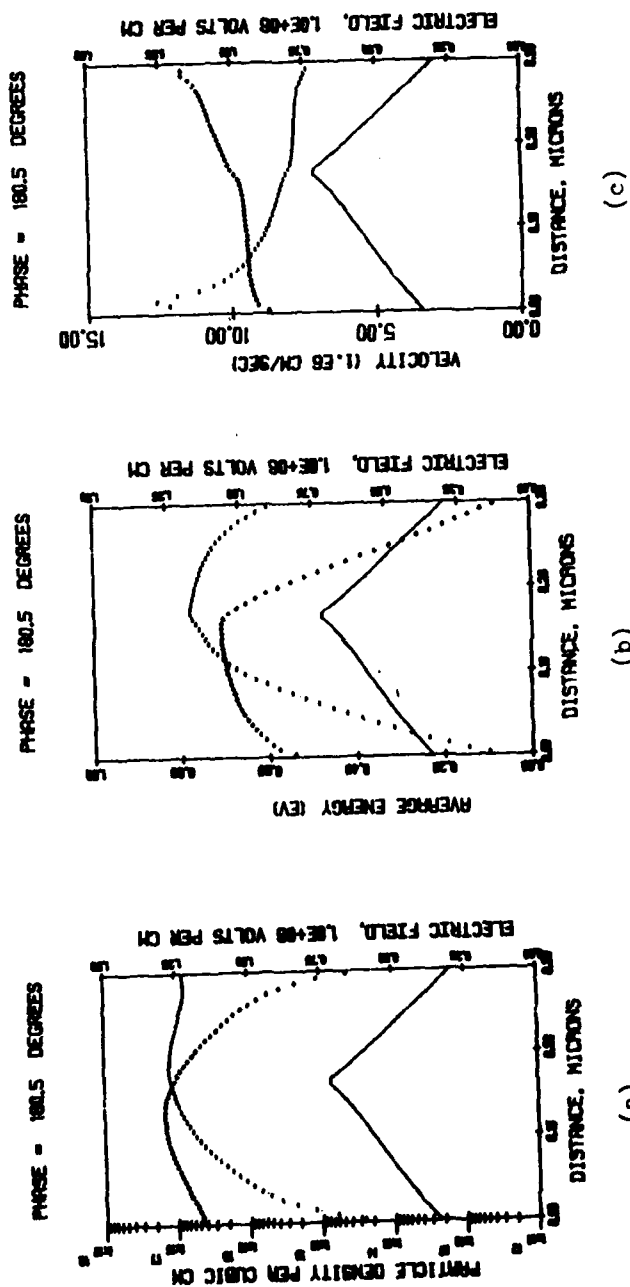


FIG. 4.15 ELECTRIC FIELD (SOLID LINES); ELECTRON DENSITY, ELECTRON ENERGY AND ELECTRON VELOCITY (MINUS SIGNS); HOLE DENSITY, HOLE ENERGY AND HOLE VELOCITY (PLUS SIGNS) VS. DISTANCE

IN THE 0.3- μ m DOUBLE-DRIFT DEVICE AT 180 DEGREES PHASE IN THE HF CYCLE SHOWN IN FIG. 4.12.

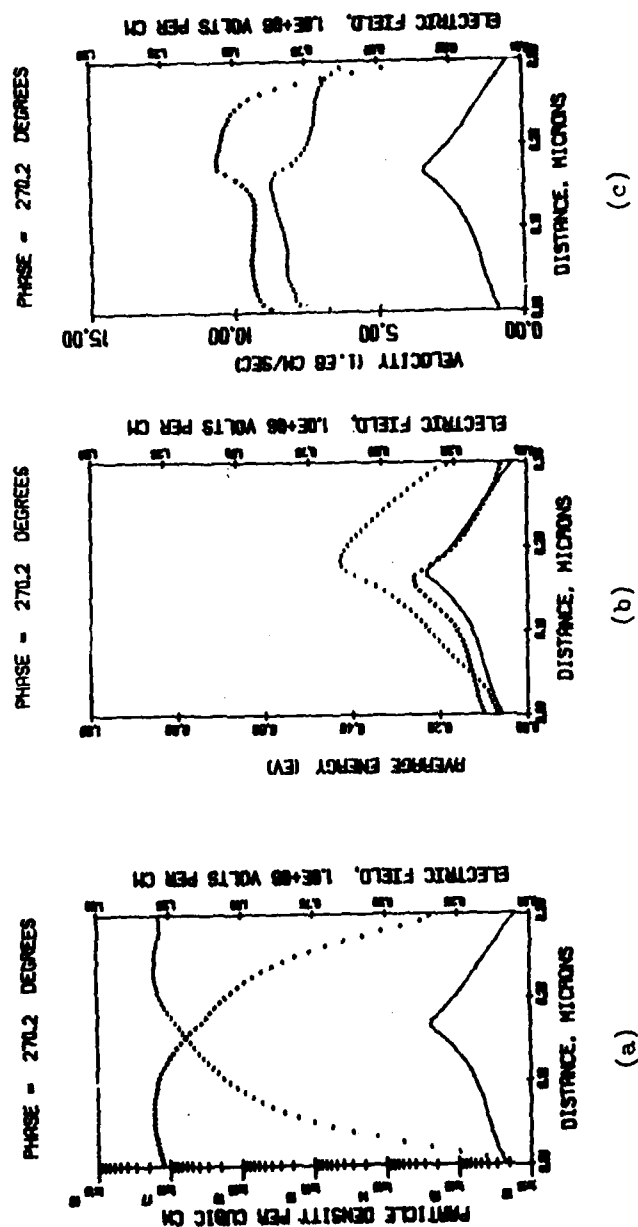


FIG. 4.16 ELECTRIC FIELD (SOLID LINES); ELECTRON DENSITY, ELECTRON ENERGY AND ELECTRON VELOCITY (MINUS SIGNS); HOLE DENSITY, HOLE ENERGY AND HOLE VELOCITY (PLUS SIGNS) VS. DISTANCE IN THE 0.3- μm DOUBLE-DRIFT DEVICE AT 270 DEGREES PHASE IN THE RF CYCLE SHOWN IN FIG. 4.12.

cycle which is shown in Fig. 4.12. The figures show the occurrence of spatial lag similar to the lag seen in Fig. 4.11.

Figures 4.17 and 4.18 show the time variation over one RF cycle of electric field, average energy, and average velocity at fixed points inside the device. The locations of the points are shown by their distances, given in the figures, from the left-hand contact. One point is located near each of the two contacts, and a third near the metallurgical junction. The energy profiles show temporal lag of approximately 20 degrees between the peak in field and the peak in majority carrier energy at the points near the device boundaries. Near the junction, the lag is somewhat less. The velocity profiles from near the boundaries show undershoot in majority carrier velocity between approximately 200- and 270-degree phase, and overshoot between approximately 300- and 30-degree phase. Similar effects occur near the center of the device, but to a lesser degree.

The phases of the velocity overshoots and undershoots in Fig. 4.18 correspond to the phases at which the induced current waveforms in Fig. 4.12 differ in shape. It appears that the shape difference in the induced currents is due to undershoots and overshoots in velocity, while the lag between the injected and the induced current waveforms is due to injection delay caused by energy lag. The shape difference is roughly symmetrical about a 270-degree phase, so it probably does not affect negative conductance strongly. Evidently the increased negative conductance seen in energy and momentum conserving results is primarily due to injection delay caused by energy lag.

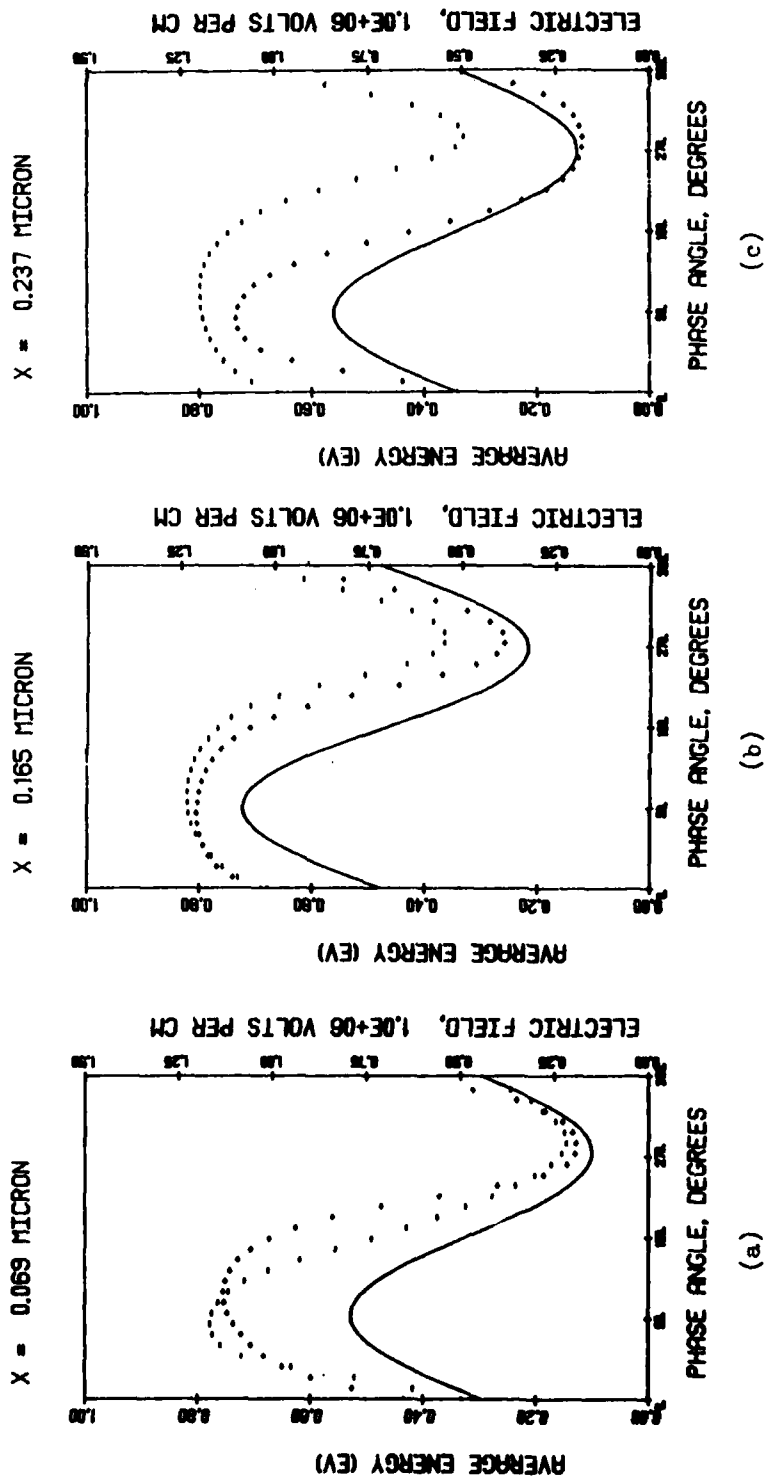


FIG. 4.17 ELECTRIC FIELD (SOLID LINES), ELECTRON ENERGY (MINUS SIGNS), AND HOLE ENERGY (PLUS SIGNS) VS. RF PHASE ANGLE AT THREE POINTS INSIDE THE 0.3- μm DOUBLE-DRIFT DEVICE.

$$(V_{RF} = 6 \text{ V}, J_{dc} = 1.5 \times 10^5 \text{ A/cm}^2 \text{ AND } f = 200 \text{ GHz})$$

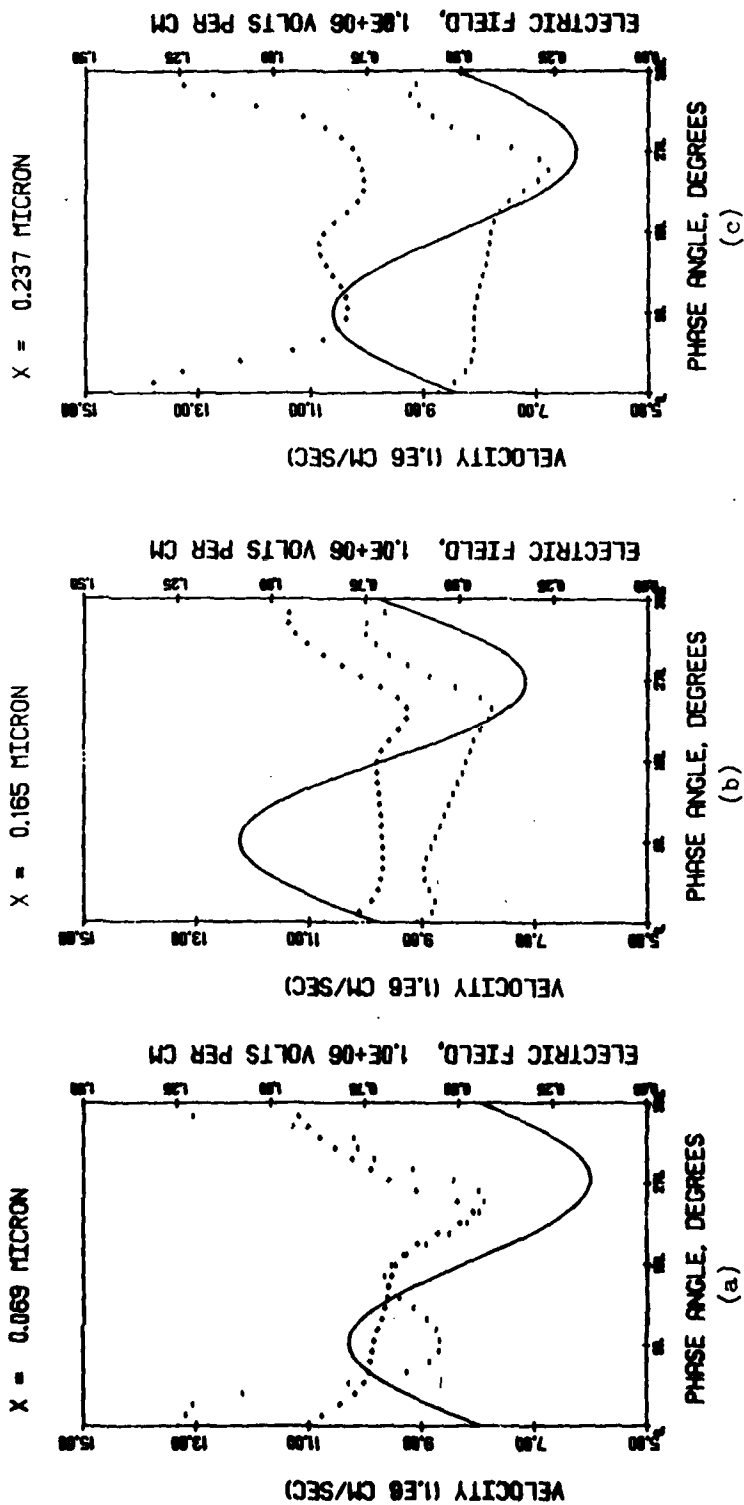


FIG. 4.18 ELECTRIC FIELD (SOLID LINES), ELECTRON VELOCITY (MINUS SIGNS) AND HOLE VELOCITY (PLUS SIGNS) VS. RF PHASE ANGLE AT THREE POINTS INSIDE THE 0.3- μ m DOUBLE-DRIFT DEVICE.

($V_{RF} = 6$ V, $J_{dc} = 1.5 \times 10^5$ A/cm² AND $f = 200$ GHz).

4.3 Effects of Boundary Conditions

Energy and momentum conserving simulation involves the setting of more boundary conditions than does conventional simulation, so it is difficult to be certain when conditions used in the two types of simulation can be considered equivalent. The boundary conditions used in obtaining the energy and momentum conserving simulation results presented thus far were those described in Chapter III. Since the inflow boundary conditions may influence spatial and temporal lag, thereby affecting device admittance results, it is important that their influence be assessed.

One way of setting realistic boundary conditions of the active region of a device is to add a highly doped contact region to each end. This allows the energy and velocity of inflowing carriers to adjust to the field strength in the contacts before the carriers enter the active region. This procedure is expensive in terms of computer time. In order that the contact regions be described realistically, the space step must be made smaller than the Debye length in the contacts. Numerical stability requires that Δt be reduced in proportion to Δx , so that the cost of simulation goes roughly as the square of the number of space steps.

Some simulation of the 0.3- μm device with contacts added has been performed. The doping profile with contacts is shown in Fig. 4.19. The Debye length was calculated using⁷⁴

$$L_d = \left(\frac{\epsilon k_B T}{q^2 N_c} \right)^{1/2}, \quad (4.1)$$

where N_c is the doping density in the contacts. At a temperature of

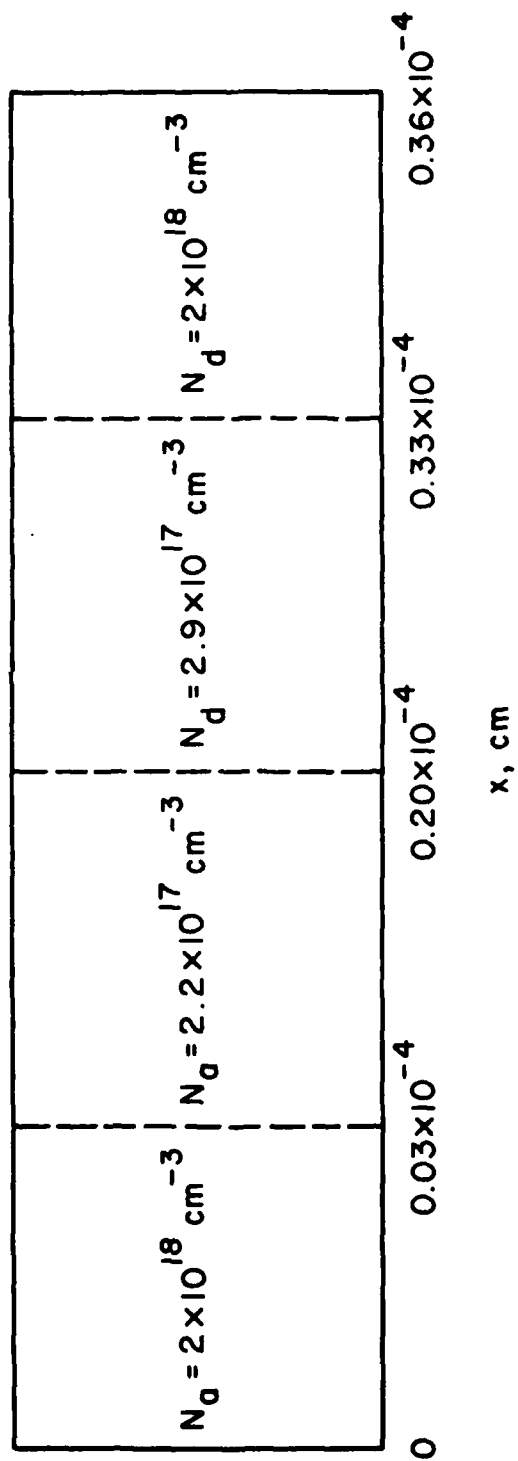


FIG. 4.19 DOPING PROFILE OF 0.3- μm DOUBLE-DRIFT DEVICE WITH CONTACT REGIONS.

500°K, the Debye length in the contact regions shown in Fig. 4.19 is approximately 37 Å. The space steps and time steps for simulation of the device with contacts were chosen to be 26 Å and 0.004 ps, respectively. This time-step length is short enough to require use of a Lax-Wendroff type finite-difference scheme, for the reasons discussed in Chapter III. Overall, adding the contacts shown to the 0.3-μm device increases the cost of simulation by more than a factor of ten.

Figures 4.20 through 4.23 show profiles of electric field, carrier concentration, average energy, and average velocity at four points in the RF cycle when the 0.3-μm device is operated at 300 GHz with an RF amplitude of 6 V. Figures 4.24 through 4.27 show similar results with no contacts present. It is evident that the behavior of the solution of the transport equations across the active region is nearly identical in the two cases. It may be concluded that it makes little difference whether specific allowance for contact regions is made or whether the simple boundary conditions described in Chapter III are applied.

4.4 Sources of Energy Lag

The two kinds of simulation results shown in Figs. 4.8 through 4.10 diverge more rapidly with decreasing device length than with increasing frequency. This can be seen from the fact that 100-GHz results, which have been obtained for each of the three devices, diverge with decreasing length, while, for a given device, the difference between the two types of results changes little with frequency. The way in which the results behave implies that the

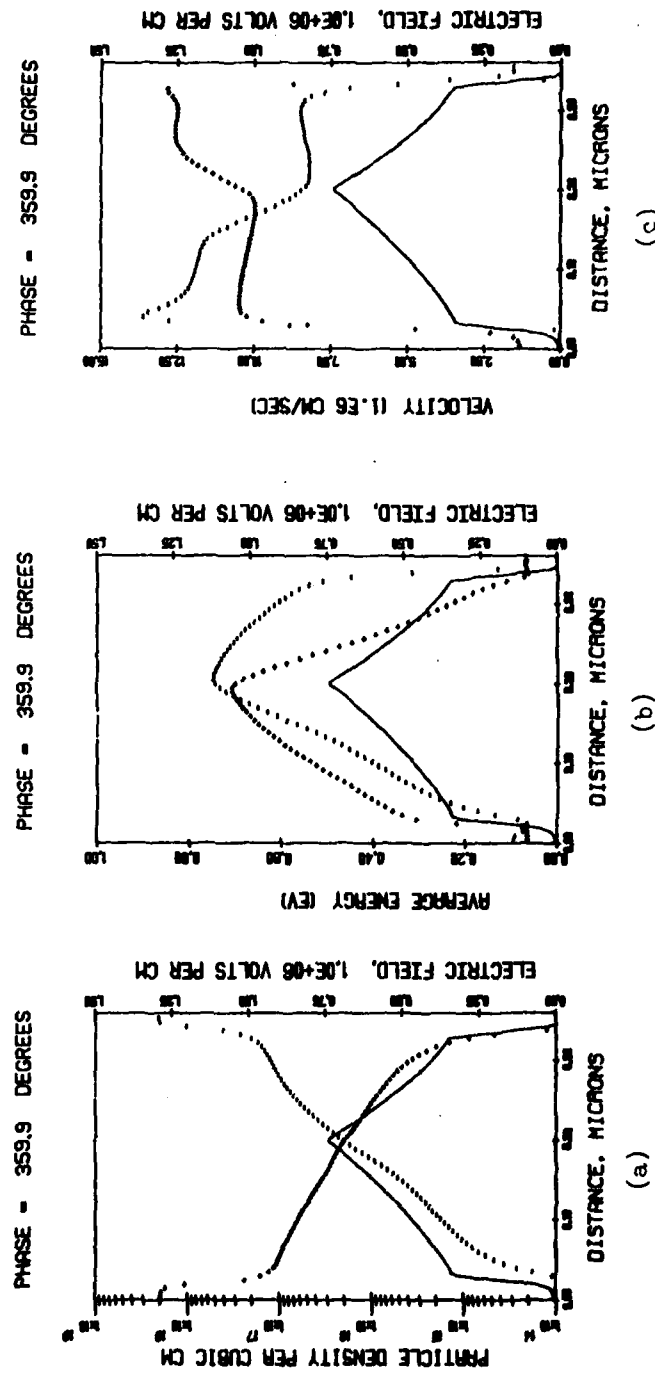


FIG. 4.20 ELECTRIC FIELD (SOLID LINES); ELECTRON DENSITY, ELECTRON ENERGY AND ELECTRON VELOCITY (MINUS SIGNS); HOLE DENSITY, HOLE ENERGY AND HOLE VELOCITY (PLUS SIGNS) VS. DISTANCE IN THE 0.3- μ m DOUBLE-DRIFT DEVICE WITH CONTACTS AT ZERO DEGREES PHASE IN THE RF CYCLE.
 $(V_{RF} = 6 \text{ V}, J_{dc} = 1.5 \times 10^5 \text{ A/cm}^2 \text{ AND } f = 300 \text{ GHz})$

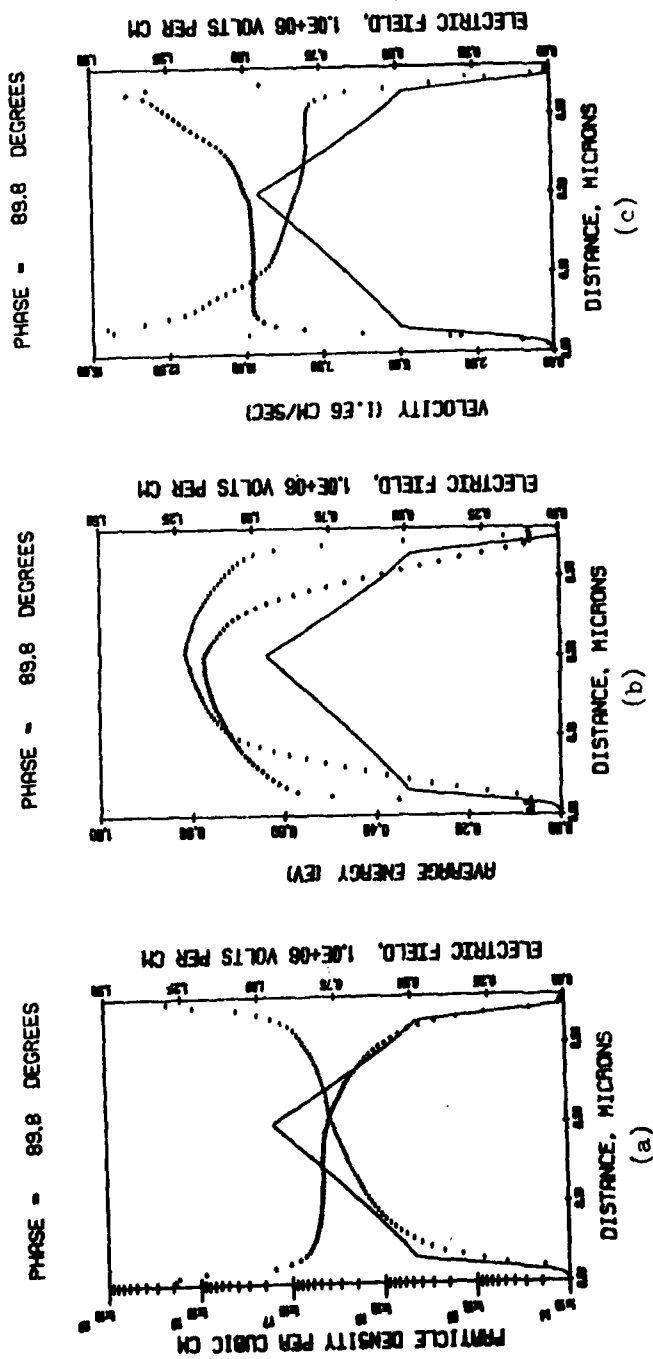


FIG. 4.21 ELECTRIC FIELD (SOLID LINES); ELECTRON DENSITY, ELECTRON ENERGY AND ELECTRON VELOCITY (MINUS SIGNS); HOLE DENSITY, HOLE ENERGY AND HOLE VELOCITY (PLUS SIGNS) VS. DISTANCE IN THE 0.3- μ m DOUBLE-DRIFT DEVICE WITH CONTACTS AT 90 DEGREES PHASE IN THE RF CYCLE.

$$(V_{RF} = 6 \text{ V}, J_{dc} = 1.5 \times 10^5 \text{ A/cm}^2 \text{ AN}; f = 300 \text{ GHz})$$

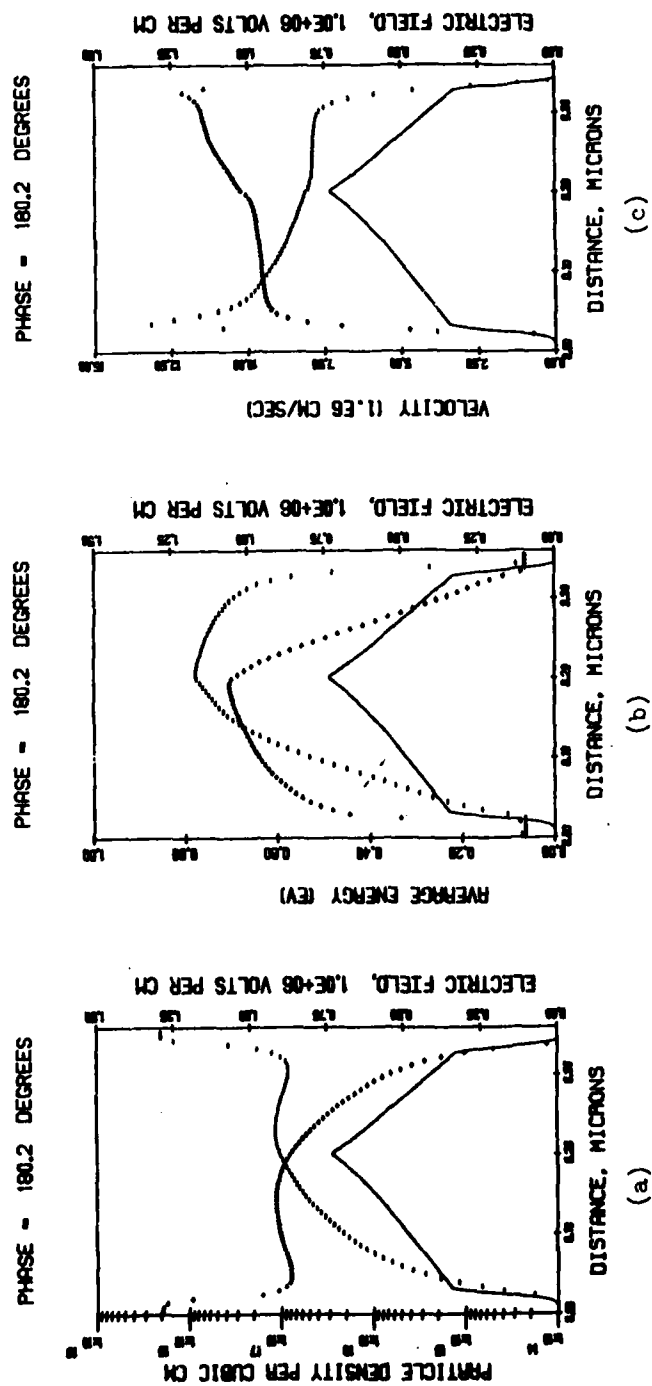


FIG. 4.22 ELECTRIC FIELD (SOLID LINES); ELECTRON DENSITY, ELECTRON ENERGY AND ELECTRON VELOCITY (MINUS SIGNS); HOLE DENSITY, HOLE ENERGY AND HOLE VELOCITY (PLUS SIGNS) VS. DISTANCE IN THE 0.3- μ m DOUBLE-DRIFT DEVICE WITH CONTACTS AT 180 DEGREES PHASE IN THE RF CYCLE.
 $(V_{RF} = 6 \text{ V}, J_{dc} = 1.5 \times 10^5 \text{ A/cm}^2 \text{ AND } f = 300 \text{ GHz})$

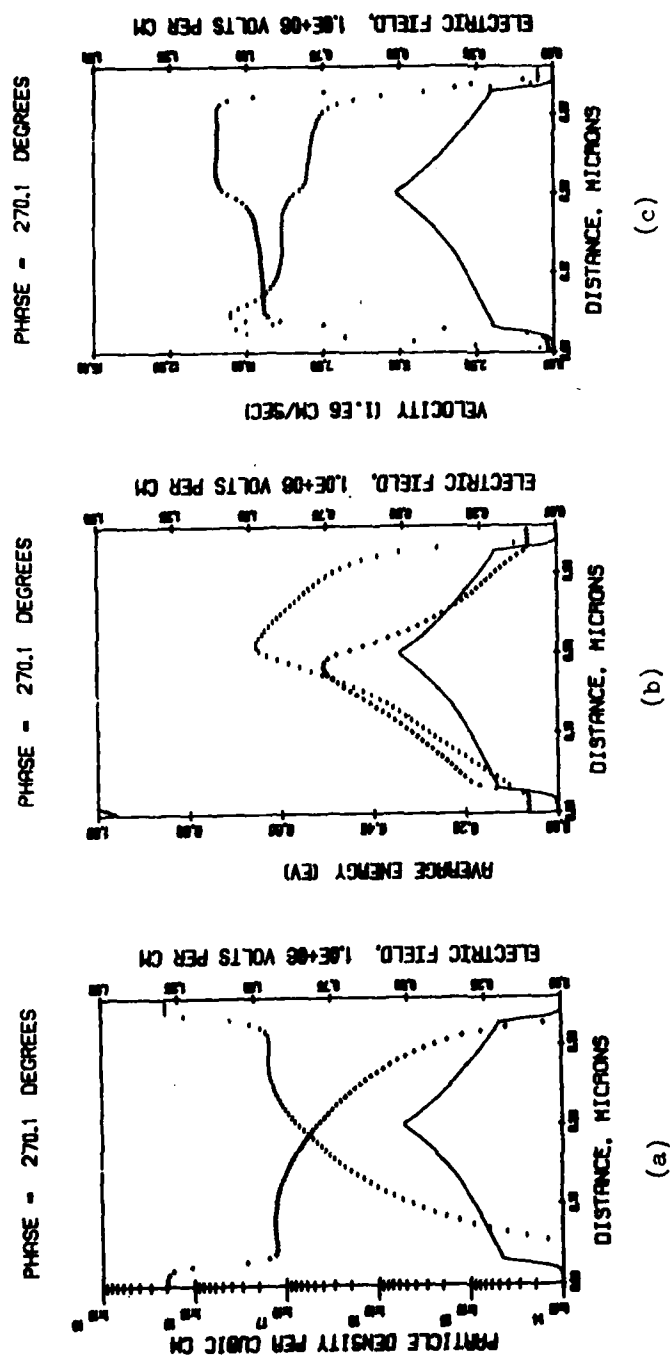


FIG. 4.23 ELECTRIC FIELD (SOLID LINES); ELECTRON DENSITY, ELECTRON ENERGY AND ELECTRON VELOCITY (MINUS SIGNS); HOLE DENSITY, HOLE ENERGY AND HOLE VELOCITY (PLUS SIGNS) VS. DISTANCE IN THE 0.3-μm DOUBLE-DRIFT DEVICE WITH CONTACTS AT 270 DEGREES PHASE IN THE RF CYCLE.
 $(V_{RF} = 6 \text{ V}, J_{dc} = 1.5 \times 10^5 \text{ A/cm}^2 \text{ AND } f = 300 \text{ GHz})$

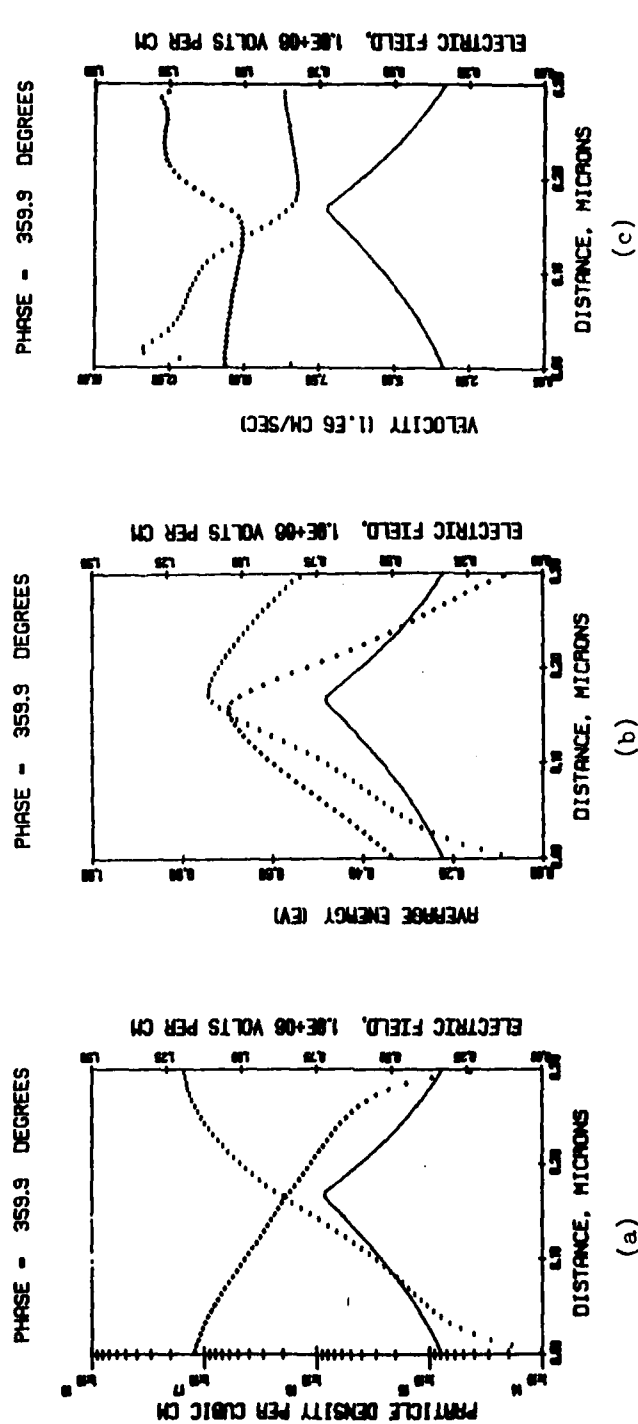


FIG. 4.24 ELECTRIC FIELD (SOLID LINES); ELECTRON DENSITY, ELECTRON ENERGY AND ELECTRON VELOCITY (MINUS SIGNS); HOLE DENSITY, HOLE ENERGY AND HOLE VELOCITY (PLUS SIGNS) VS. DISTANCE IN THE 0.3- μ m DOUBLE-DRIFT DEVICE WITHOUT CONTACTS AT ZERO DEGREES PHASE IN THE RF CYCLE.
 $(V_{RF} = 6 \text{ V}, J_{dc} = 1.5 \times 10^5 \text{ A/cm}^2 \text{ AND } f = 300 \text{ GHz})$

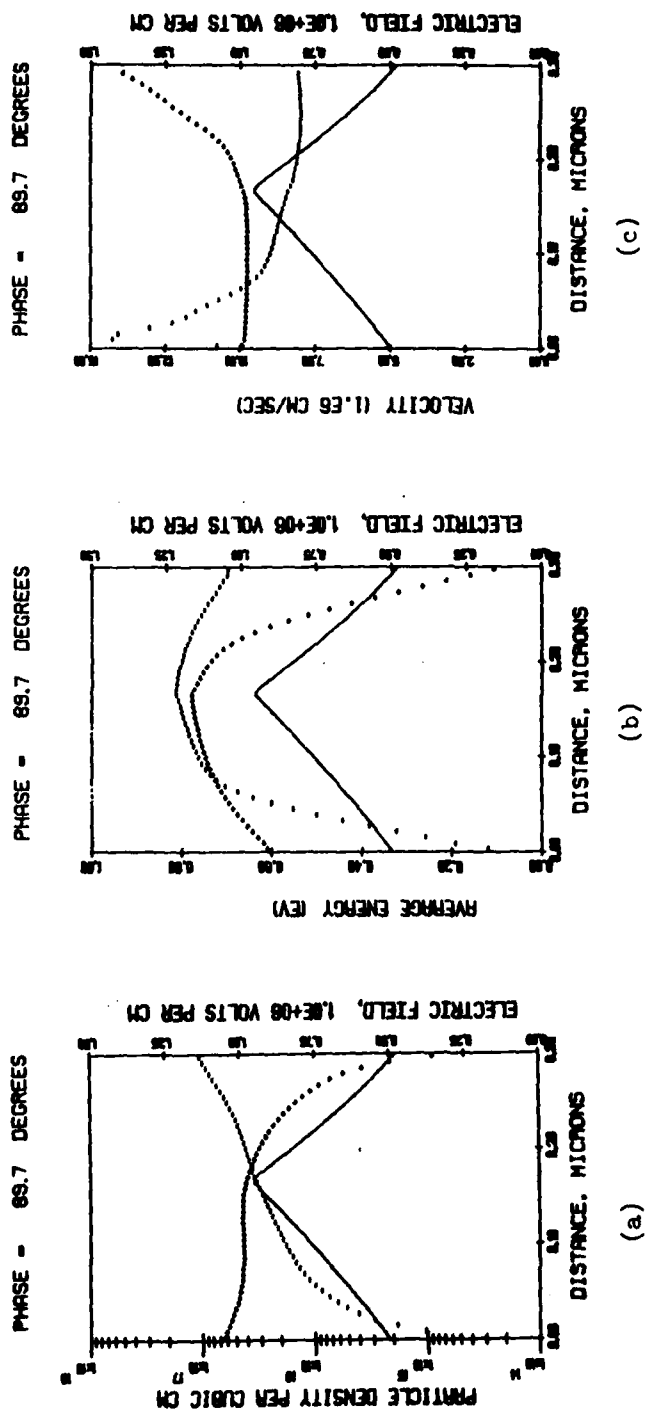


FIG. 4.25 ELECTRIC FIELD (SOLID LINES); ELECTRON DENSITY, ELECTRON ENERGY AND ELECTRON VELOCITY (MINUS SIGNS); HOLE DENSITY, HOLE ENERGY AND HOLE VELOCITY (PLUS SIGNS) VS. DISTANCE IN THE 0.3- μ m DOUBLE-DRIFT DEVICE WITHOUT CONTACTS AT 90 DEGREES PHASE IN THE RF CYCLE. ($V_{RF} = 6$ V, $J_{dc} = 1.5 \times 10^5$ A/cm² AND $f = 300$ GHz)

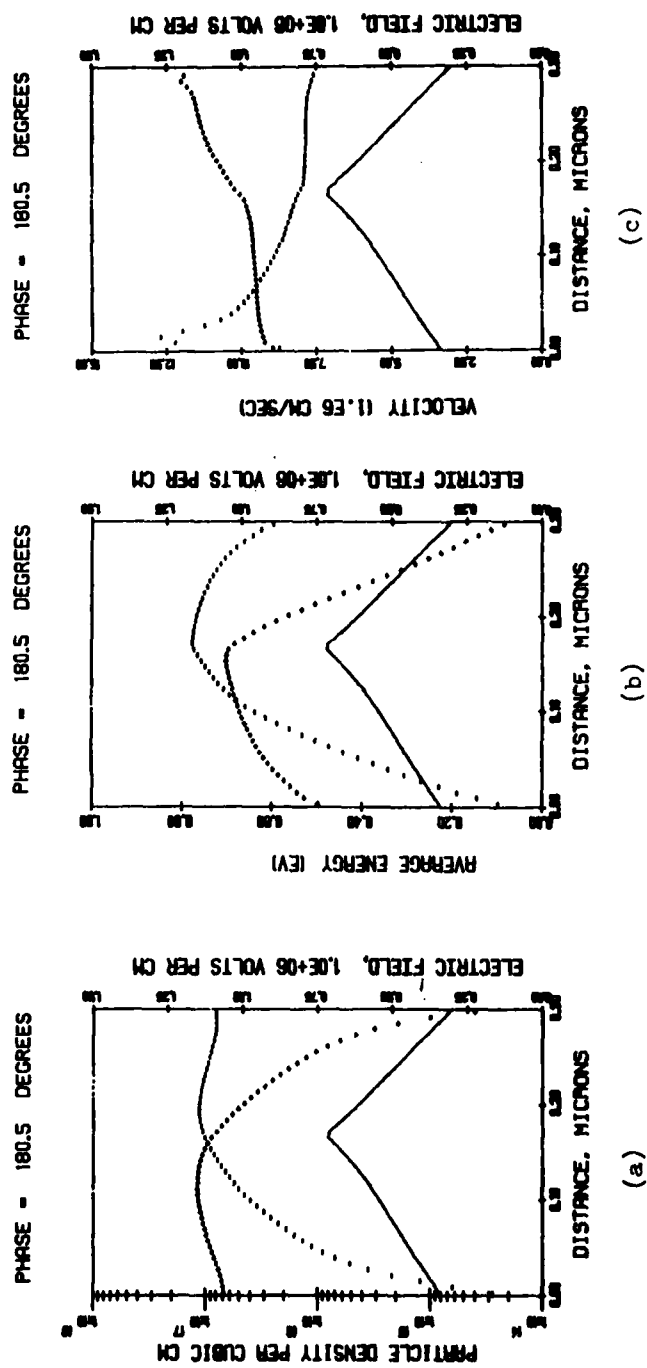


FIG. 4.26 ELECTRIC FIELD (SOLID LINES); ELECTRON DENSITY, ELECTRON ENERGY AND ELECTRON VELOCITY (MINUS SIGNS); HOLE DENSITY, HOLE ENERGY AND HOLE VELOCITY (PLUS SIGNS) VS. DISTANCE IN THE 0.3- μ m DOUBLE-DRIFT DEVICE WITHOUT CONTACTS AT 180 DEGREES PHASE IN THE RF CYCLE.
 $(V_{RF} = 6 \text{ V}, J_{dc} = 1.5 \times 10^5 \text{ A/cm}^2 \text{ AND } f = 300 \text{ GHz})$

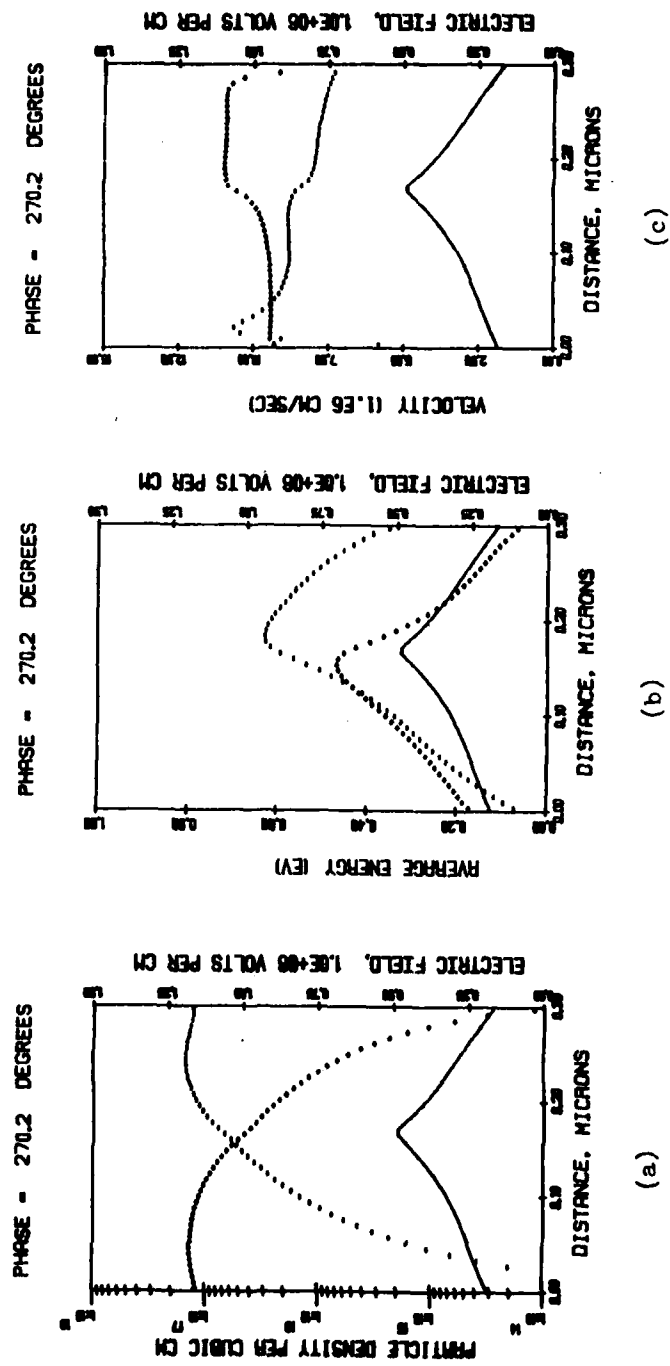


FIG. 4.27 ELECTRIC FIELD (SOLID LINES); ELECTRON DENSITY, ELECTRON ENERGY AND ELECTRON VELOCITY (MINUS SIGNS); HOLE DENSITY, HOLE ENERGY AND HOLE VELOCITY (PLUS SIGNS) VS. DISTANCE IN THE 0.3- μ m DOUBLE-DRIFT DEVICE WITHOUT CONTACTS AT 270 DEGREES PHASE IN THE RF CYCLE.
 $(V_{RF} = 6 \text{ V}, J_{dc} = 1.5 \times 10^5 \text{ A/cm}^2 \text{ AND } f = 300 \text{ GHz})$

energy lag which gives rise to increased negative conductance becomes more pronounced as device length decreases, but changes comparatively little with frequency. Factors which might contribute to the length dependence of energy lag include the inflow boundary conditions on energy, carrier cooling due to impact ionization by opposing carriers, and spatial variation of the electric field. Each of these will now be examined.

Effects of the inflow boundary conditions on spatial lag have been tested by incorporating "hot" boundaries, in which the inflowing carriers are assigned three times the thermal energy associated with the lattice temperature, in the simulation program. This might be expected to reduce the amount by which carriers are out of equilibrium with the field after crossing the field step at the inflow boundary. Figures 4.28 and 4.29 show resulting profiles of electric field, average energy, and average velocity which correspond to those shown in Figs. 4.24 through 4.27. The similarity between the corresponding profiles shows that the degree of energy lag has little to do with the inflow conditions on energy.

Energy lag might also be affected by the cooling of each carrier distribution by impact ionizations caused by the opposing carrier type. This possibility will be explained in terms of electrons. The number of electrons entering a device at the left-hand boundary is small. Just upstream of the boundary, impact ionizations initiated by holes may produce a number of electrons comparable to or greater than the number which actually cross the boundary. Consequently, the average energy of electrons near the boundary may be determined for the most part by the low average

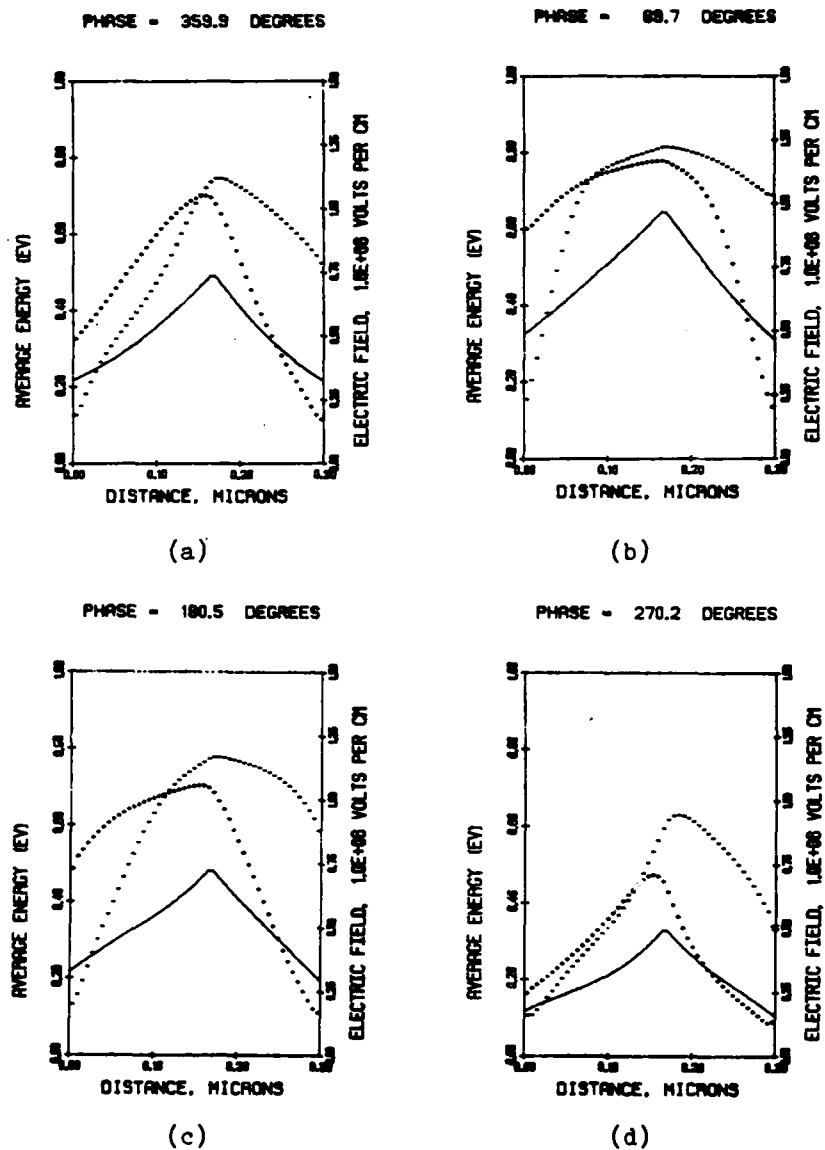


FIG. 4.28 ELECTRIC FIELD (SOLID LINES), ELECTRON ENERGY (MINUS SIGNS) AND HOLE ENERGY (PLUS SIGNS) UNDER "HOT" BOUNDARY CONDITIONS VS. DISTANCE IN THE 0.3- μ m DOUBLE-DRIFT DEVICE AT VARIOUS POINTS IN THE RF CYCLE. ($V_{RF} = 6$ V, $J_{dc} = 1.5 \times 10^5$ A/cm² AND $f = 300$ GHz)

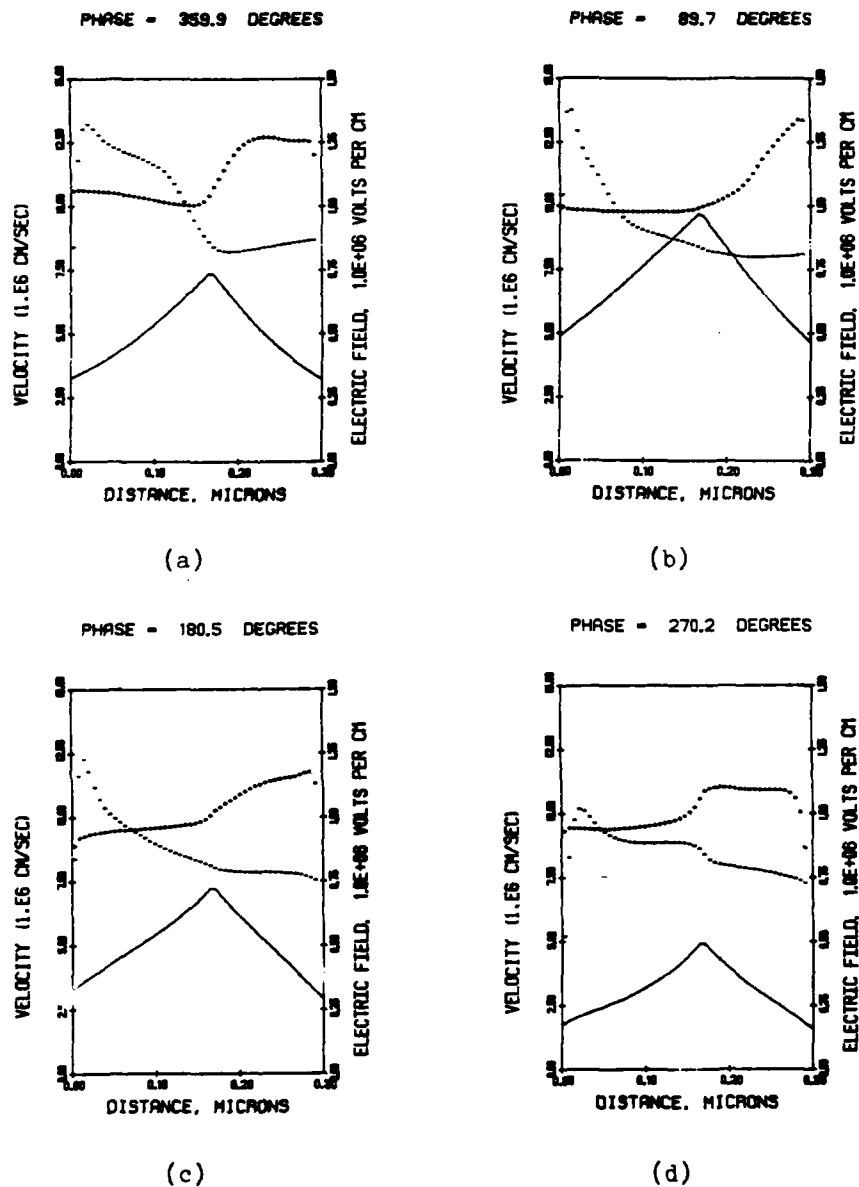


FIG. 4.29 ELECTRIC FIELD (SOLID LINES), ELECTRON VELOCITY (MINUS SIGNS) AND HOLE VELOCITY (PLUS SIGNS) UNDER "HOT" BOUNDARY CONDITIONS VS. DISTANCE IN THE 0.3-μm DOUBLE-DRIFT DEVICE AT VARIOUS POINTS IN THE RF CYCLE. ($V_{RF} = 6$ V, $J_{dc} = 1.5 \times 10^5$ A/cm² AND $f = 300$ GHz)

energy of those electrons which are produced by hole ionizations. This would depress the average energy of the electron distribution and contribute to spatial lag. The hole distribution near the right-hand boundary might be affected in a similar way.

In order to eliminate this "opposite-carrier cooling" effect, it can be assumed that carriers created by opposite-carrier ionizations have exactly the same average energy as those already present. Then Eq. 2.32 would become

$$\left(\frac{\partial w}{\partial t} \right)_{c_2} = (w - w_0) \beta \frac{D}{n} = 0 \quad (4.2)$$

Figures 4.30 and 4.31 show electric field, average energy, and average velocity profiles calculated under the same conditions as were those shown in Fig. 4.24 through 4.27, except that opposite-carrier cooling has been eliminated from the simulation program. The change clearly results in less spatial lag.

These results suggest a reason why, as seen previously, simulation results are relatively insensitive to changes in the inflow boundary conditions. The total population of each carrier near its inflow boundary conditions is dominated by carriers produced by opposite-carrier ionizations. Average energy and velocity near inflow boundaries are determined mainly by the energy and velocity of carriers produced by impact ionizations, and not by the properties of carriers which cross the inflow boundary. Thus opposite-carrier cooling has the effect of decoupling the interior of the device from its inflow boundaries.

Figures 4.32 and 4.33 show admittance results from the 1- and 0.3- μ m devices with and without opposite-carrier cooling.

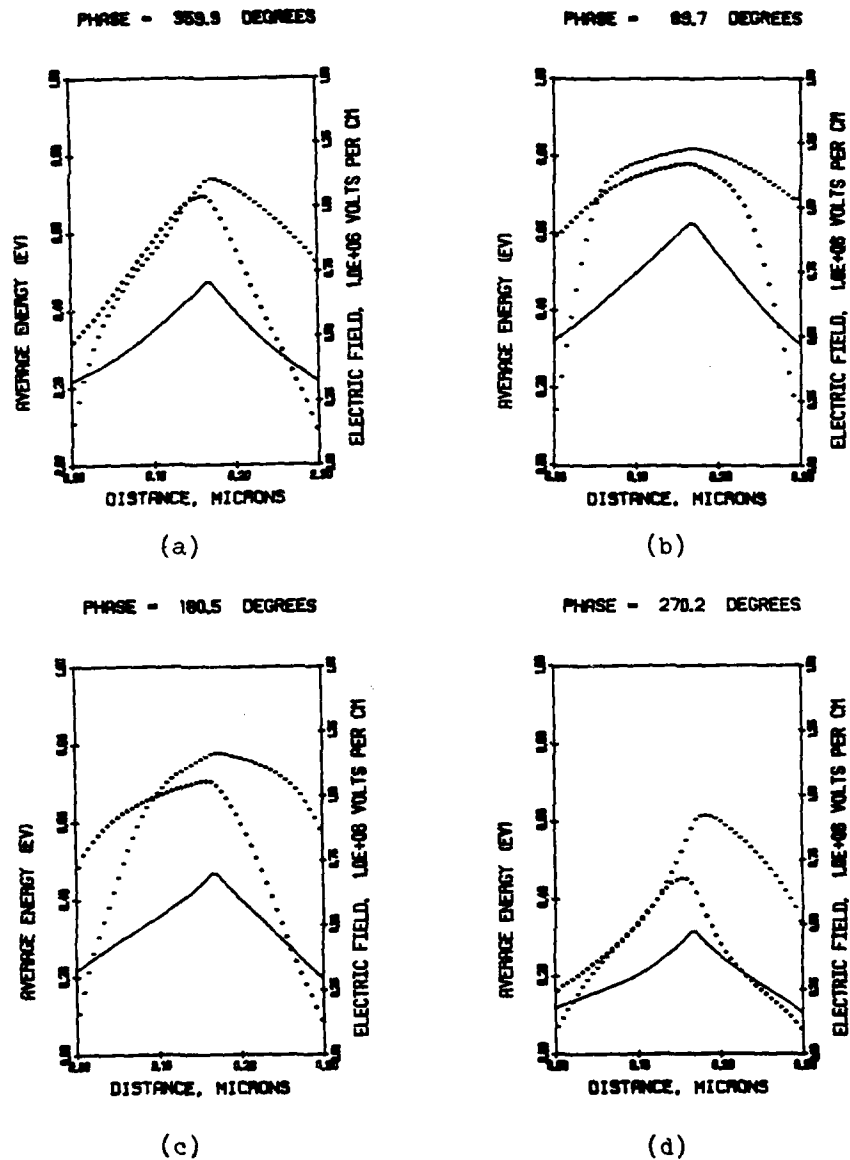


FIG. 4.30 ELECTRIC FIELD (SOLID LINES), ELECTRON ENERGY (MINUS SIGNS) AND HOLE ENERGY (PLUS SIGNS) WITHOUT OPPOSITE-CARRIER COOLING VS. DISTANCE IN THE 0.3-μm DOUBLE-DRIFT DEVICE AT VARIOUS POINTS IN THE RF CYCLE. ($V_{RF} = 6$ V, $J_{dc} = 1.5 \times 10^5$ A/cm² AND $f = 300$ GHz)

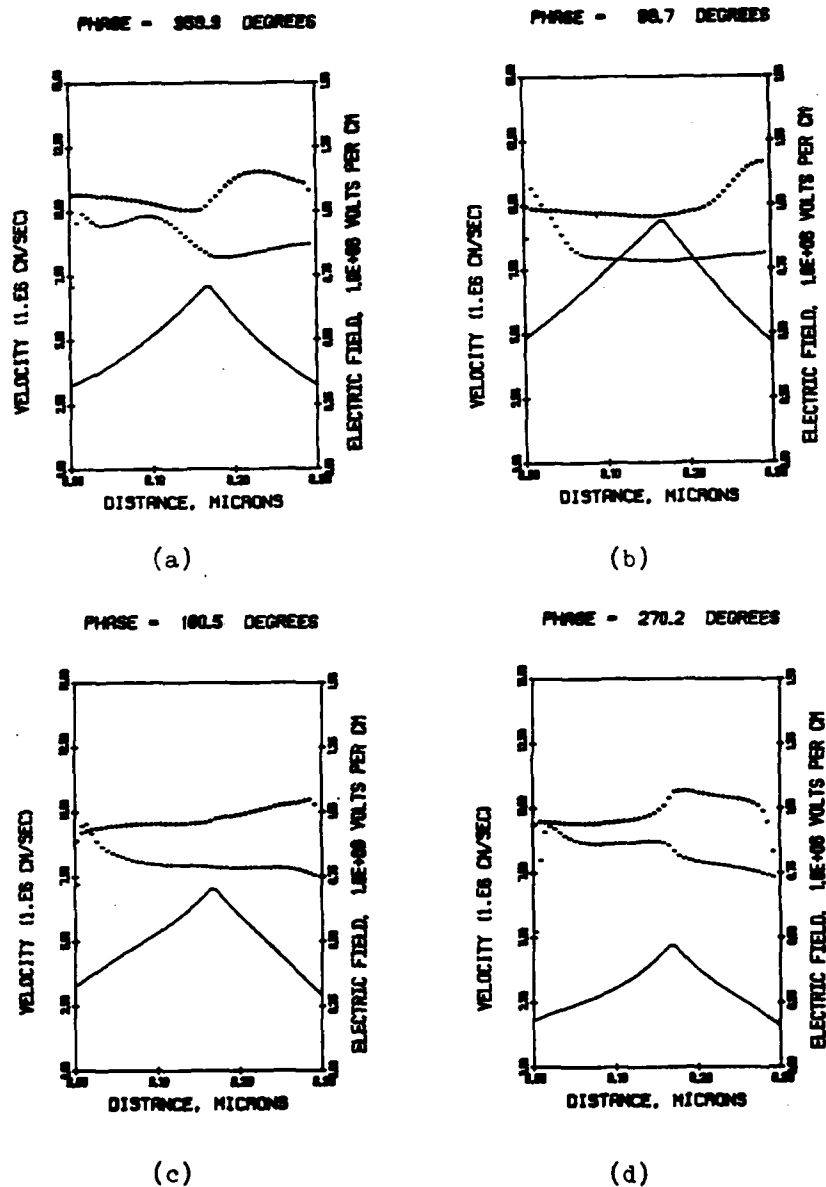


FIG. 4.31 ELECTRIC FIELD (SOLID LINES), ELECTRON VELOCITY (MINUS SIGNS) AND HOLE VELOCITY (PLUS SIGNS) WITHOUT OPPOSITE-CARRIER COOLING VS. DISTANCE IN THE 0.3- μm DOUBLE-DRIFT DEVICE AT VARIOUS POINTS IN THE RF CYCLE. ($V_{\text{RF}} = 6 \text{ V}$, $J_{\text{dc}} = 1.5 \times 10^5 \text{ A/cm}^2$ AND $f = 300 \text{ GHz}$)

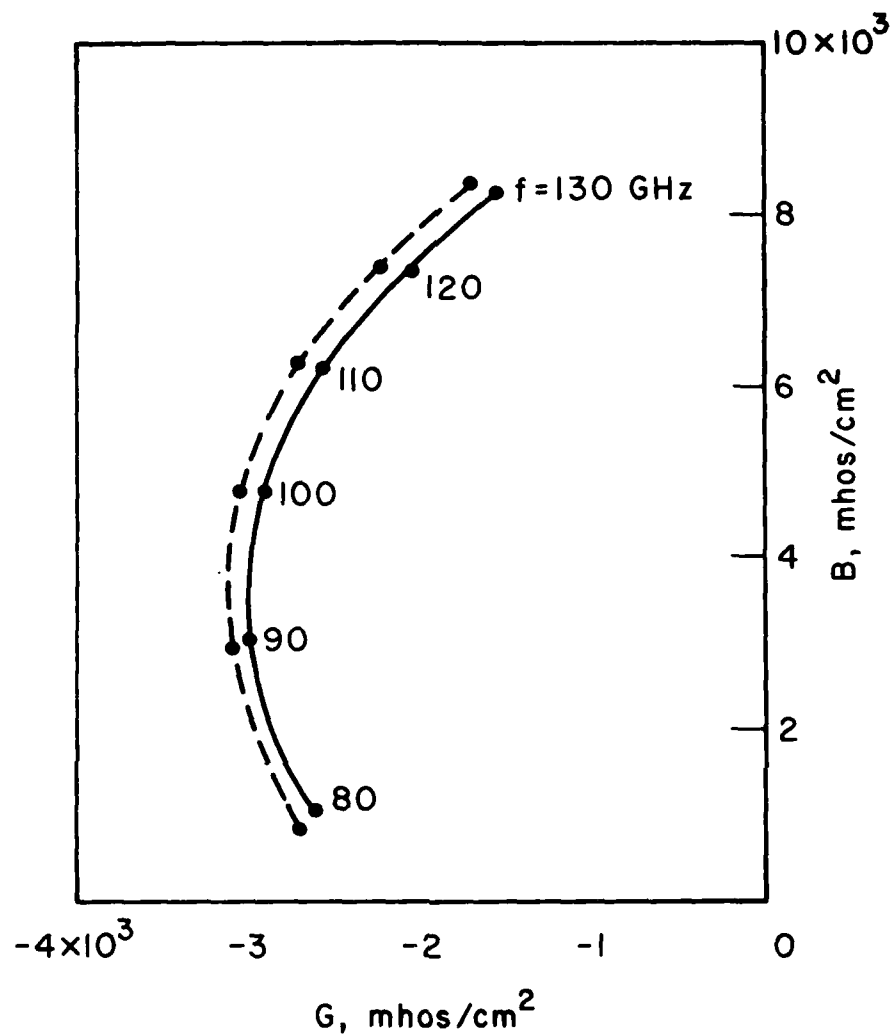


FIG. 4.32 G-B CHARACTERISTICS FOR THE 1- μm , DOUBLE-DRIFT
 DEVICE WITH (SOLID LINE) AND WITHOUT (DASHED LINE)
 OPPOSITE-CARRIER COOLING. ($V_{\text{RF}} = 10 \text{ V}$ AND
 $J_{\text{dc}} = 6 \times 10^5 \text{ A}/\text{cm}^2$)

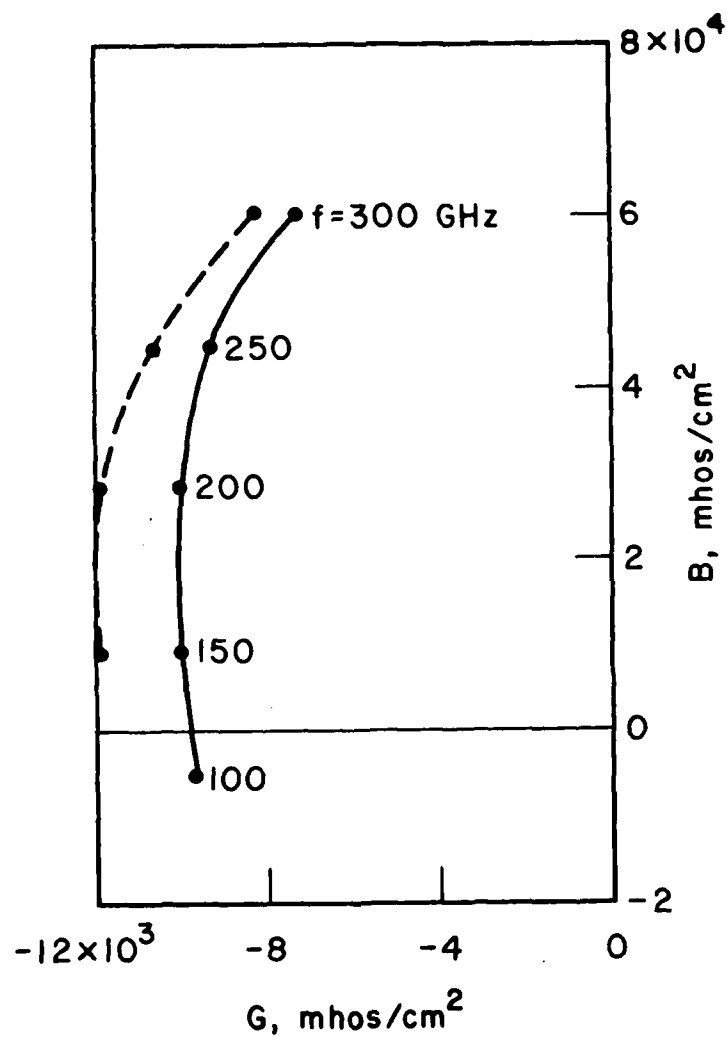


FIG. 4.33 G-B CHARACTERISTICS FOR THE $0.3\text{-}\mu\text{m}$ DOUBLE-DRIFT DEVICE WITH (SOLID LINE) AND WITHOUT (DASHED LINE) OPPOSITE-CARRIER COOLING. ($V_{\text{RF}} = 6 \text{ V}$ AND $J_{\text{dc}} = 1.5 \times 10^5 \text{ A}/\text{cm}^2$)

The removal of cooling from the simulation can be seen to result in increased negative conductance in both devices, with the increase being much more pronounced in the case of the shorter device. These results are in apparent contradiction to the idea that energy lag is what causes increased negative conductance in energy and momentum conserving simulation results. Opposite-carrier cooling increases the amount of spatial lag associated with the inflow boundaries, but it reduces negative conductance. This can be seen from comparison of Figs. 4.8 and 4.10 with Figs. 4.32 and 4.33. Spatial lag associated with opposite-carrier cooling clearly does not cause the observed divergence between simulation results. Instead, it tends to counteract the effects of whatever does give rise to the divergence.

The mechanism which does cause the two types of results to diverge is probably associated with the spatial gradient of electric field strength inside the double-drift devices. In contrast to the flat-field structures considered in Section 4.1, the double-drift structures described in Section 4.2 are doped heavily enough to give considerable slope to the field strength. The slope in field gives rise to a kind of distributed energy lag whose degree increases with the steepness of the slope, hence with increasing doping concentration. This will now be described in more detail.

The total time rate of change in field strength seen by a moving carrier consists not only of the time rate of change of field at the current position of the carrier, but also of the change seen by the carrier as it moves through spatial variations in the field. The total rate of change is given by

$$\frac{dE}{dt} = \frac{\partial E}{\partial t} + u \frac{\partial E}{\partial x} . \quad (4.3)$$

During much of the buildup of the injected pulse, the carrier current densities are small, and the time partial of the electric field is approximately equal to the time partial of the terminal voltage divided by the device length. When the voltage is sinusoidal, the maximum of the time partial of the field at angular frequency ω is given by

$$\frac{\partial E}{\partial t} = \frac{\omega V_{RF}}{L} \quad (4.4)$$

and occurs at 0-degree phase. When the carrier density is small, the space partial of the field is related to the doping density by Poisson's equation:

$$\frac{\partial E}{\partial x} = \frac{qN_i}{\epsilon} . \quad (4.5)$$

For electrons in the p layer of the 1- μ m double-drift device at a frequency of 100 GHz and an RF amplitude of 10 V, Eq. 4.3 becomes

$$\frac{dE}{dt} = 6.3 \times 10^{16} \text{ V/cm}\cdot\text{s} + 1.2 \times 10^{17} \text{ V/cm}\cdot\text{s} , \quad (4.6)$$

where it is assumed that u is 8.5×10^6 cm/s. Similarly, in the 0.3- μ m device at an amplitude of 6 V, the equation becomes

$$\frac{dE}{dt} = 1.3 \times 10^{17} \text{ V/cm}\cdot\text{s} + 2.9 \times 10^{17} \text{ V/cm}\cdot\text{s} . \quad (4.7)$$

Equations 4.6 and 4.7 show that the total time rate of change of field seen by a moving carrier at a given frequency is much larger in the 0.3- μ m device than in the 1- μ m device. The equations also show that, even at the moment when the time partial of the field is

at its maximum, the spatial gradient of field contributes the majority of the total rate of change seen by a moving carrier. The greater the total rate of change, the greater the lag between carrier energy and field, so that at the center of the 0.3- μm device the ionization rates peak later in the RF cycle than in the 1- μm device, giving rise to more injection delay and a larger increase in negative conductance relative to the conventional result.

4.5 Limitations on IMPATT Performance

The simulation results presented in this chapter indicate that Si diodes will support operation of the IMPATT mode at frequencies up to at least 300 GHz. It will be shown in this section that the material properties do eventually impose a fundamental upper frequency limit on IMPATT operation. The frequency at which this limit lies can be estimated for any material by use of the energy balance relation and is in the submillimeter-wave region for Si devices. This section also discusses why the simulation predicts millimeter-wave device efficiencies which are in excess of those which are obtained in experiment. It is shown that this can be fully explained by the presence of parasitic series resistance external to the active IMPATT layer.

The existence of an upper frequency limit for IMPATT operation is a result of the way in which carrier energy responds to the time variation of the electric field. The simple energy balance relation, which accounts for energy gain from the field and loss to lattice collisions, provides an approximate description of the energy response:

$$\frac{dw}{dt} = quE - \frac{w - w_0}{\tau_w} \quad (4.8)$$

If u is constant and the time-varying component of the field is given by the real part of $E_0 e^{i\omega t}$, the solution for the time-varying component of energy is

$$w = \text{Re} \left[\frac{\tau_w}{1 + i\omega\tau_w} qE_0 u e^{i\omega t} \right] \quad (4.9)$$

The energy response given by Eq. 4.9 follows the familiar single-pole transfer function. A Bode plot⁷⁵ for the normalized response is shown in Fig. 4.34. The plot shows that the amplitude of the response is down by a factor of two at a frequency of $1/2\pi\tau_w$. In view of the rapid variation of the ionization rates with energy which is shown in Fig. 2.3, it appears that IMPATT mode operation will be seriously degraded at this frequency because of reduced particle current modulation. The response begins to roll off an octave lower, implying that material properties (specifically the energy relaxation time) will impose an upper frequency limit of approximately $1/4\pi\tau_w$ for substantially undegraded IMPATT operation.

Figure 4.34 also shows the increasing phase lag between energy and field as frequency increases. Lippens and Constant⁴⁰ have used the energy balance relation to support previously published findings from this work which pointed to energy lag as the reason for predictions of increased negative conductance in energy and momentum conserving simulation results. Lippens and Constant suggested that the findings could be explained in terms of the phase lag shown in the figure. While their conclusion that the phase lag in itself tends to make IMPATT operation more efficient is valid,

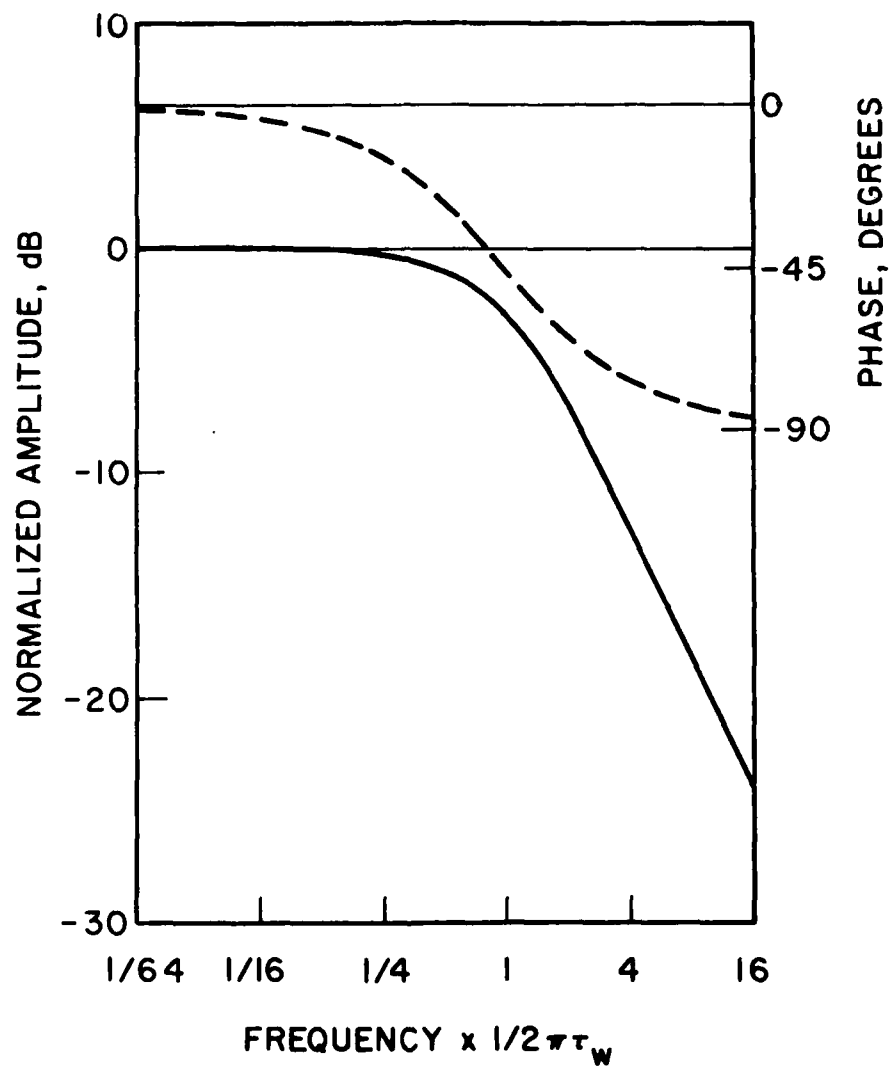


FIG. 4.34 NORMALIZED AMPLITUDE AND PHASE OF THE CARRIER
ENERGY RESPONSE VS. FREQUENCY.

they overlooked the roll off in the energy response which is predicted by the energy balance relation. It should be noted that the simple balance relation fails to allow for spatial inhomogeneities. In fact, as previously noted, spatial field gradients are apparently the principal reason for differences between conventional and energy and momentum conserving simulation results for submicron IMPATT devices.

While analysis involving the energy balance relation is approximate, a more detailed analysis would not invalidate the conclusion that the energy response will roll off at high frequencies. Equation 4.9 predicts that the frequency at which roll off begins is approximately $1/4\pi\tau_w$. The energy relaxation time for electrons in Si was estimated in Chapter II to be approximately 0.15 ps over a broad range of energy, implying that IMPATT mode operation in Si will deteriorate substantially at frequencies above 500 GHz. This roll off in the energy response may be the reason why the two admittance curves in Fig. 4.10 cross just below 500 GHz.

The best reported experimental efficiencies for millimeter-wave Si IMPATTs are 1 percent or less at frequencies above 150 GHz.⁷⁶ This is much lower than the efficiencies routinely obtained from microwave devices. The results of this study suggest that this is not due to an intrinsic failure of the IMPATT mode in Si at millimeter-wave frequencies. An alternative explanation is that parasitic losses are responsible for low millimeter-wave efficiencies and constitute the major limitation on the experimental performance of millimeter-wave IMPATT diodes. Sources of parasitic loss include undepleted substrate layers in diode structures,

ohmic contact resistance, series resistance of bond wires, and other circuit losses. Loss mechanisms which are unimportant at lower frequencies may become important in the millimeter-wave range because of skin effects, surface scattering effects, and reductions in carrier mobility due to velocity relaxation.

A detailed analysis of parasitic loss is outside the scope of this study, but the effect of loss can be estimated by placing an equivalent parasitic resistance in series with the "intrinsic" diode. Figure 4.34 shows both "intrinsic" negative resistance and efficiency in the presence of various values of series resistance as functions of RF amplitude for the 0.3 μm device operating at 300 GHz. A device diameter of 0.5 mil is assumed. "Intrinsic" efficiency as predicted by conventional simulation is also shown. The peak efficiency predicted by energy and momentum conserving simulation is much greater than that predicted by conventional simulation, and both efficiencies are large enough to indicate little deterioration in the operation of the IMPATT mode in Si at frequencies up to 300 GHz. The presence of parasitic resistance can be seen to reduce efficiency drastically.

4.6 Summary and Conclusions

Simulation results show that the additional physical effects allowed for in the energy and momentum conserving transport model cause the average energy of carriers to lag behind the local electric field. Energy lag can occur in space, downstream of abrupt changes in field, or it can occur in time, in the presence of rapid time variation of field. Energy lag gives rise to overshoots and undershoots in carrier velocity as compared to conventional field-dependent

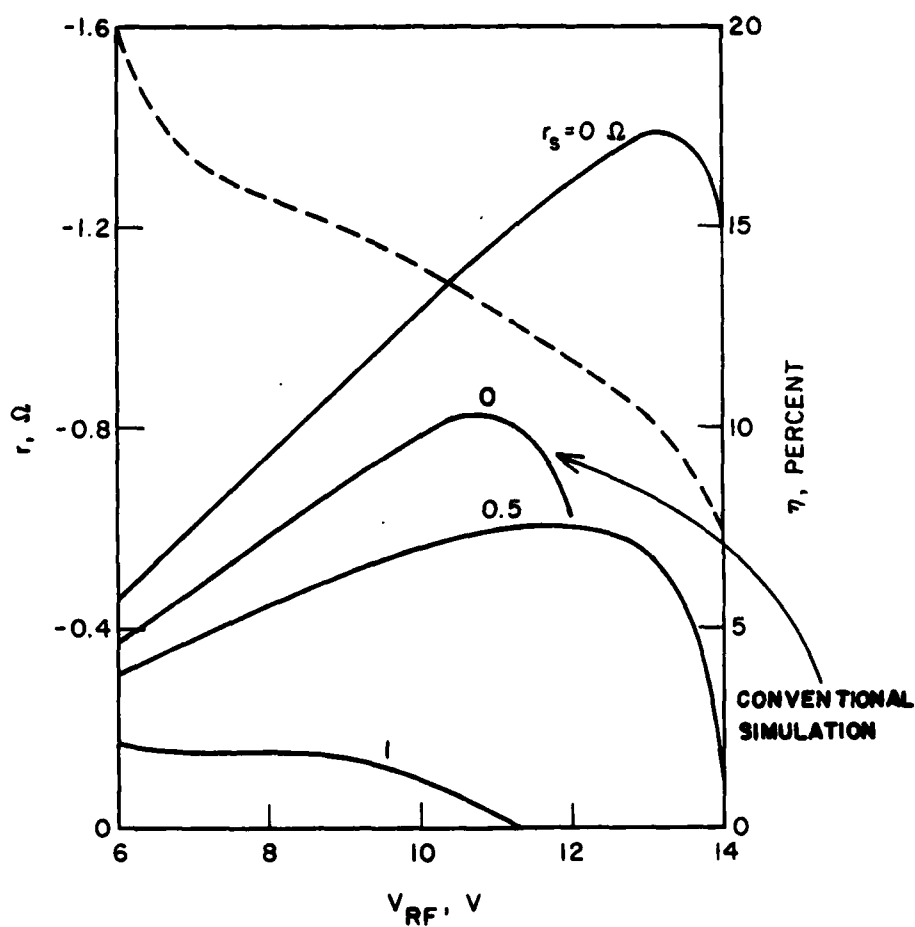


FIG. 4.35 "INTRINSIC" NEGATIVE RESISTANCE (DASHED LINE)
AND EFFICIENCY IN THE PRESENCE OF VARIOUS VALUES
OF SERIES RESISTANCE (SOLID LINES) VS. RF AMPLITUDE
FOR THE 0.3- μ m DOUBLE-DRIFT DEVICE. ($f = 300$ GHz
AND $J_{dc} = 1.5 \times 10^5$ A/cm²)

drift velocity. Local departures from the conventional velocity can be large, but tend to affect minority carriers rather than majority carriers in IMPATTs, so their effect on device terminal admittance is generally small.

As the double-drift device length becomes less than $0.5 \mu\text{m}$, energy and momentum conserving simulation predicts substantially better IMPATT performance than does conventional simulation. A 70-percent difference in predicted optimum efficiency at 300 GHz has been observed. Differences in predicted performance appear to be due to injection delay caused by the lag between the carrier energy and the electric field. This lag appears to be caused by spatial field gradients.

Simulation results are relatively insensitive to boundary conditions on carrier energy, and the boundary conditions described in Chapter II have been found to give results consistent with those obtained incorporating realistic contact regions. The degree of carrier cooling which results from impact ionization by opposing carriers is of more importance to device behavior than boundary conditions. This cooling increases the amount of spatial energy lag and reduces negative conductance.

Simulation results predict greater millimeter-wave device efficiencies than are observed in experiment. This can be accounted for by the presence of modest amounts of parasitic series resistance. It is apparently such resistance, rather than a deterioration of IMPATT mode operation at high millimeter-wave frequencies, that limits the performance of experimental devices. In the absence of parasitic loss, the upper frequency of operation of the IMPATT

mode would be subject to a fundamental limit which is set by material properties. This limit is estimated to be approximately 500 GHz for Si devices.

CHAPTER V. SUMMARY, CONCLUSIONS,
AND SUGGESTIONS FOR FURTHER RESEARCH

5.1 Summary and Conclusions

The purpose of this study was to develop and apply a new class of semiconductor device simulation which is more general than existing drift-diffusion based simulations, and to use the simulation to investigate the "intrinsic" properties of millimeter-wave Si IMPATTs. A self-consistent bipolar energy and momentum conserving simulation has been developed for this purpose. The work that was performed falls into three categories: model definition, model implementation, and model utilization. The overall effort is believed to be the first reported application of a self-consistent bipolar energy and momentum conserving transport model to semiconductor device simulation.

Work performed in the category of model definition was described in Chapter II of this dissertation. The charge-transport model developed consists of transport equations for electron and hole concentration, average velocity, and average energy as functions of time and space. It provides a second-order description of the carrier-velocity distributions, and allows the distributions to evolve in space and time in a self-consistent manner. This is in contrast to the conventional model based on drift and diffusion, which implicitly assumes that the distributions are always in equilibrium with the local electric field.

The transport equations themselves are the zeroth, first, and second velocity moments of the phase-space transport equation. Except for the terms describing the effects of collisions, the equations were obtained by application of the method of moments. The collision terms were not obtained in this way because the form of the phase-space collision term for carriers in Si is not sufficiently well known to permit the taking of velocity moments. Instead, forms for the collision terms were chosen in such a way as to allow for their dependence on the concentration, average energy, and average velocity. The collision parameters used in the model are energy-dependent relaxation times for energy and velocity, and energy-dependent, per-unit-time impact ionization rates. The latter are more fundamental than the conventional per-unit-distance ionization rates because they do not assume any correlation between the average carrier energy, which determines the number of ionizations taking place per unit time, and the average velocity, which determines the distance traveled in the average time between ionizations.

The parameters were given numerical values by simplifying the transport equations to describe the situation of a spatially uniform, dc electric field, and requiring that results from the simplified equations be consistent with experimentally known values of electron and hole drift velocities and ionization rates. Mapping the parameters onto the carrier energies was accomplished through use of a theoretically determined equilibrium relationship between the carrier energies and the electric field. The hole and electron energy relaxation times determined in this way were approximately 0.075 and 0.15 ps, respectively, over much of the carrier energy

range considered. The velocity relaxation times were found to range from twice the energy relaxation times at low energies to less than 0.02 ps at high energies.

A correspondence between the energy and momentum conserving transport model and the conventional drift-diffusion model was established. This showed that, under the conditions of slow space and time variation of the electric field, the conventional diffusion coefficient can be written in terms of the velocity relaxation time and the temperature of the carrier distribution. The resulting estimates for the electron and hole diffusion coefficients as functions of the electric field drop off considerably from their low-field values as field strength increases. The energy and momentum conserving model was also compared to other nonconventional models which have been applied to modeling of IMPATTs. The latter were shown to be less complete and less self-consistent than the energy and momentum conserving model.

Computer implementation of the transport model using finite-difference techniques was described in Chapter III. A set of normalizations was developed which (for constant time and space step) eliminates the time step, the space step, and several physical constants from the finite-difference equations. Stability analysis of various finite-difference schemes showed that many explicit forms of the energy and momentum conserving transport equations are unstable when the time step is short in comparison to the relaxation times, and other stable forms may exhibit undesirably large amounts of numerical diffusion. A scheme of the Lax-Wendroff type was found to be capable of giving stability

and minimal numerical diffusion for all time-step lengths. It was further shown that, when the time step is sufficiently long, certain more efficient schemes which are otherwise unstable can be made stable by the use of an advanced-time form of the energy and velocity relaxation terms.

Chapter IV presented results of computer simulation of millimeter-wave Si avalanche diode structures. Simulation of low-doped diodes with spatially uniform electric field shows that rapid field changes in space (such as at the boundaries of depletion regions) and time (as in the presence of large-signal RF terminal voltages) can give rise to nonequilibrium between the carrier velocity distribution and the electric field. Such nonequilibrium manifests itself in the form of lag between the carrier energy and local electric field, and gives rise to velocity overshoot or undershoot. The length of the distance over which the minority carrier distribution adjusts itself to a field step in space was shown to be strongly affected by the initial temperature assigned to carriers generated by impact ionization by carriers of the "opposing" type.

Energy and momentum conserving simulation results were found to diverge significantly from conventional results as device length becomes less than 1 μm . Energy and momentum conserving results predict greater negative conductance than conventional results, apparently because of increased injection delay caused by lag between the carrier energies and the electric field. The amount by which the two types of results diverge depends more strongly on device length than upon operating frequency. This is apparently

due to the increased field gradients which occur as device length decreases. Differences between predicted performances at optimum RF amplitude are particularly large.

Simulation results showed no degradation in operation of the IMPATT mode in Si at frequencies up to 300 GHz. Calculations based on the energy balance relation predicted that the IMPATT mode in Si will begin to degrade as frequency exceeds 500 GHz because the carrier energies will cease to respond to time variation of the electric field. The millimeter-wave efficiencies predicted by simulation results are well in excess of those which have been obtained in experiment. This strongly suggests that parasitic loss, rather than failure of the intrinsic IMPATT mode, is the factor which presently limits the performance of the current state-of-the-art devices.

5.2 Suggestions for Further Research

The present investigation has laid a foundation for a variety of further work. Suggestions for further research can be considered in three categories: transport modeling, numerical methods, and device simulation.

The most obvious extension in the category of transport modeling is to incorporate nonequivalent conduction band valleys. This would extend the applicability of the simulation to III-V compounds such as GaAs and InP, which are widely used to fabricate high-performance semiconductor devices. It is known that certain relaxation times in GaAs and InP are much longer than those encountered in Si,⁷⁷ and so "transient" effects will probably be of importance at lower frequencies and in larger devices than is the case for Si.

The forms of the equations for the multi-valley case have been presented by Blotekjaer.⁴⁷ However, compared to the single-valley situation, additional relaxation times are needed to characterize intervalley transfer. These cannot be determined by the method used in Chapter II (i.e., requiring consistency with experimental measurements), and, as discussed below, will have to be obtained in some other way. Work on extending the energy and momentum conserving model to transport in GaAs is currently underway within the Electron Physics Laboratory.

Under low-field conditions calculation of the required additional relaxation times is reasonably straightforward, using statistical Monte Carlo simulation or the Rees iterative technique.⁴⁴ Existing theoretical calculations seem to be inconsistent with experimental observations for intermediate and high fields--typically above 20 kV/cm. (One example is the calculation by Jacoboni et al.⁷⁸ of mean carrier energies of the order of 0.5 eV at a field of 100 kV/cm. This implies significant impact ionization at this field, something which is not observed in practice.) The discrepancy between theory and experiment may be due to neglect of the intra-collisional field effect.⁷⁹ A major priority for future transport modeling should be transport characterization including impact ionization and the intra-collisional field effect. The deterministic Rees iterative technique is probably best suited for transport characterization and parameter evaluation, since it avoids the large statistical variance associated with Monte Carlo characterization of "rare" events such as impact ionization, and

is also well suited to describing nonlinear effects such as transport in degenerate semiconductors and Auger recombination.

Additional work in the area of numerical methods should include the extension to two spatial dimensions. This will probably not present fundamental problems; the stability criteria for finite-difference approximations to the two-dimensional transport equations should be similar to those established in this work for the one-dimensional case, and techniques for the rapid solution of the two-dimensional Poisson's equation are now well established.⁸⁰ The extension to two dimensions would permit energy and momentum conserving simulation of transistor structures. Another extension of the simulation would be incorporation of a nonzero heat flow vector. It does not appear that this would be difficult, although stability of proposed finite-difference equations incorporating a description of heat flow should be examined using the techniques applied in Chapter III. Finally, renewed attention could be given to the prospects of obtaining an implicit or semi-implicit numerical scheme whose stability would permit use of longer time steps. The advantage of such a scheme is not certain, however, since time-step size is limited by accuracy requirements even for unconditionally stable schemes.

The application of energy and momentum conserving simulation to semiconductor device modeling is in its infancy. Advances in technology have only recently made possible the fabrication of devices so small that traditional drift-diffusion simulation provides a generally inappropriate description. The overshoot effects in small devices can be described using parameterized

distributions as in the present work, or using "exact" distributions. The former approach is much less expensive. Only when a case can be made that the "fine structure" of the distribution is significant (as in the Jones-Rees effect¹¹ in Gunn diodes) does it seem worthwhile attempting to use "exact" distribution models. The previously mentioned extensions to the present work would yield an energy and momentum conserving simulation applicable to a wide range of semiconductor devices, and could provide answers to many questions of current interest in the field of sub-micron electronics. Possible one-dimensional simulation investigations include simulation of other transit-time devices (including TUNNETTs and transferred electron devices) and investigation of the large-signal RF properties of nn^+ junctions. A two-dimensional simulation could be used to model short-channel effects in MESFETs and MOSFETs, and to examine the feasibility of proposed "novel" transistors such as the ballistic transistor¹² and planar doped barrier transistor.¹³ Overall, energy and momentum conserving simulation seems likely to become the standard approach of sub-micron semiconductor device modelers.

The most significant means of comparison between conventional and energy and momentum conserving IMPATT simulation results may be to compare on the basis of maximum obtainable efficiency. A logical extension of the work presented in this study would be to use the two types of simulation to search for optimum IMPATT structures and large-signal operating points as functions of frequency over the millimeter-wave range.

APPENDIX A. MATERIAL PARAMETERS

The material parameters used throughout this study pertain to Si at a lattice temperature of 500°K. The diffusion coefficients used in all drift-diffusion simulation are those given in Fig. 2.4. Static ionization rates⁸⁴ are given in Table A.1. Table A.2 gives static drift velocities, and Table A.3 lists a number of other parameters.

Table A.1

Static Ionization Rates⁸⁴

$$\alpha(E) = A \exp(-b/E) \text{ cm}^{-1}$$

Quantity	Holes	Electrons	E (kV/cm)
A (cm ⁻¹)	2.0 x 10 ⁶	2.6 x 10 ⁶	0 < E < 240
	2.0 x 10 ⁶	6.2 x 10 ⁵	240 ≤ E < 530
	5.6 x 10 ⁵	5.0 x 10 ⁵	E ≥ 530
b (kV/cm)	2.17 x 10 ³	1.69 x 10 ³	0 < E < 240
	2.17 x 10 ³	1.31 x 10 ³	240 ≤ E < 530
	1.54 x 10 ³	1.25 x 10 ³	E ≥ 530

Table A.2

Static Drift Velocity³

$$V_d(E) = v_{\text{sat}} [1 - \exp(-\mu|E|/v_{\text{sat}})] \text{ cm/s}$$

Quantity	Holes	Electrons
v _{sat} (cm/s)	1.02 x 10 ⁷	8.5 x 10 ⁶
μ (cm ² /V·s)	250	550

Table A.3

Other Parameters

Quantity	Symbol	Value
Dielectric constant	ϵ	1.04×10^{-12} F/cm
Ionization threshold energy	E_c	2.0 eV
Optical phonon energy	$\hbar\omega$	0.056 eV
Effective mass	m	4.55×10^{-31} kg (holes) 8.84×10^{-31} kg (electrons)
Mean free path	λ	60 Å (holes) 80 Å (electrons)

LIST OF REFERENCES

1. Shockley, W., "Negative Resistance Arising from Transit Time in Semiconductor Diodes," Bell System Tech. J., vol. 33, No. 4, pp. 799-826, July 1954.
2. Read, W. J., "A Proposed High Frequency Negative Resistance Diode," Bell System Tech. J., vol. 37, No. 2, pp. 401-446, March 1958.
3. Bauhahn, P. E., "Properties of Semiconductor Materials and Microwave Transit-Time Devices," Technical Report No. 140, Electron Physics Laboratory, The University of Michigan, Ann Arbor, October 1977.
4. Lee, C. A., Batdorf, R. L., Wiegmann, W. and Kaminsky, G., "The Read Diode--An Avalanching, Transit-Time, Negative-Resistance Oscillator," Appl. Phys. Letters, vol. 6, No. 5, pp. 89-91, 1 March 1965.
5. Johnston, R. L., De Loach, B. C., Jr. and Cohen, B. G., "A Silicon Diode Microwave Oscillator," Bell System Tech. J., vol. 44, No. 2, pp. 369-372, February 1965.
6. Milford, T. A. and Bernick, R. L., "Millimeter Wave CW IMPATT Diodes and Oscillators," IEEE Trans. on Microwave Theory and Techniques, vol. MTT-27, No. 5, pp. 483-492, May 1979.
7. Edwards, R., Ciccolella, D. F., Misawa, T., Iglesias, D. E. and Decker, V., "Millimeter-Wave Silicon IMPATT Diodes," Presented at the 1969 IEEE Int. Electron Devices Meeting, Washington, DC, October 1969.
8. Gelden, M. and Moroney, W., "High-Power Pulsed Avalanche Diode Oscillators for Microwave Frequencies," Proc. IEEE (Correspondence), vol. 55, No. 1, pp. 1227-1228, July 1967.
9. Ying, R. S., English, D. L., Weller, K. P., Nakaji, E. M., Lee, D. H. and Bernick, R. L., "Millimeter-Wave Pulsed IMPATT Diode Oscillators," Proc. Fifth Biennial Cornell Electrical Engineering Conf., Ithaca, NY, pp. 337-388, August 1975.
10. Bowman, L. S. and Burrus, C. A., Jr., "Pulsed-Driven Silicon p-n Junction Avalanche Oscillators for the 0.9 to 20 mm Band," IEEE Trans. on Electron Devices, vol. ED-14, No. 8, pp. 411-418, August 1967.
11. Seidel, T. E., Niehaus, W. C. and Iglesias, D. E., "Double-Drift Silicon IMPATT's at X-Band," IEEE Trans. on Electron Devices, vol. ED-21, No. 8, pp. 523-531, August 1974.

12. Pfund, G., Snapp, C. and Podell, A., "Pulsed and CW Double-Drift Silicon IMPATTs," Presented at the 1974 IEEE/GMTT Int. Microwave Symp., Atlanta, GA, June 1974.
13. Ohmori, M., Ishibashi, T. and Ono, S., "Dependence of Highest Harmonic Oscillation Frequency on Junction Diameter of IMPATT Diodes," IEEE Trans. on Electron Devices, vol. ED-24, No. 12, pp. 1323-1329, December 1977.
14. Fong, T. T. and Kuno, H. J., "Millimeter-Wave Pulsed IMPATT Sources," IEEE Trans. on Microwave Theory and Techniques, vol. MTT-27, No. 5, pp. 492-499, May 1979.
15. Brook, P., "Active Microwave Devices--IMPATTs," Microwave Solid State Devices and Applications, Peter Peregrinus Ltd., New York, 1980.
16. Dilozenzo, J. V. and Wisseman, W. R., "GaAs Power MESFETs: Design, Fabrication, and Performance," IEEE Trans. on Microwave Theory and Techniques, vol. MTT-27, No. 5, pp. 367-378, May 1979.
17. Allison, R., "Silicon Bipolar Microwave Power Transistors," IEEE Trans. on Microwave Theory and Techniques, vol. MTT-27, No. 5, pp. 415-422, May 1979.
18. Oakes, J. G., Wickstrom, R. A., Tremere, D. A. and Heng, M.T.S., "A Power Silicon Microwave MOS Transistor," IEEE Trans. on Microwave Theory and Techniques, vol. MTT-24, No. 6, pp. 305-311, June, 1976.
19. Uchiazki, I., Hori, S., Oda, Y. and Tomita, N., "3-GHz 15-W Silicon Bipolar Transistors," IEEE Trans. on Microwave Theory and Techniques, vol. MTT-27, No. 12, pp. 1038-1042, December 1979.
20. Schellenberg, J. M., Yamasaki, H. and Maki, D. W., "A 69 GHz FET Oscillator," Presented at the 1981 MTT-S International Microwave Symposium, Los Angeles, CA, June 1981.
21. Wallace, R. N., Stelle, S. R. and Alderstein, M. G., "Performance of GaAs Double-Drift Avalanche Diodes," Proc. Sixth Biennial Cornell Electrical Engineering Conf., Ithaca, NY, pp. 195-202, August 1977.
22. Hierl, T. L., Berenz, J. J. and Long, S. I., "GaAs Pulsed Read IMPATT Diodes," Proc. Sixth Biennial Cornell Electrical Engineering Conf., Ithaca, NY, pp. 211-219, August 1977.

23. Brook, P., Smith, J. G., Clough, L. D., Tearle, C. A., Ball, G. and Birbeck, J. H., "Design, Fabrication and Performance of GaAs High-Efficiency IMPATT Diodes in J-Band (Ka Band)," Proc. Sixth Biennial Cornell Electrical Engineering Conf., Ithaca, NY, pp. 221-231, August 1977.
24. Sun, C., Benko, E. and Tully, J. W., "A Tunable High-Power V-Band Gunn Oscillator," IEEE Trans. on Microwave Theory and Techniques, vol. MTT-27, No. 5, pp. 512-514, May 1979.
25. Talwar, A. K., "A Dual-Diode 73-GHz Gunn Oscillator," IEEE Trans. on Microwave Theory and Techniques, vol. MTT-27, No. 5, pp. 510-512, May 1979.
26. Ondria, J., "Wide-Band Mechanically Tunable W-Band (75-110 GHz) CW GaAs Gunn Diode Oscillator," Proc. Seventh Biennial Cornell Electrical Engineering Conf., Ithaca, NY, pp. 309-320, August 1979.
27. Crowley, J. D., Fank, F. B., Hyder, S. B., Sowers, J. J. and Tringate, D., "Millimeter Wave InP Transferred Electron Devices," Proc. Seventh Biennial Cornell Electrical Engineering Conf., Ithaca, NY, pp. 331-340, August 1979.
28. Takada, T., Makimura, T. and Ohmori, M., "Hybrid Integrated Frequency Doublers and Triplers to 300 and 450 GHz," IEEE Trans. on Microwave Theory and Techniques, vol. MTT-28, No. 9, pp. 966-973, September 1980.
29. Scharfetter, D. L., "Power-Impedance-Frequency Limitations of IMPATT Oscillators Calculated from a Scaling Approximation," IEEE Trans. on Electrical Devices, vol. ED-18, No. 8, pp. 536-543, August 1971.
30. Fisher, S. T., "Small-Signal Impedance of Avalanching Junctions with Unequal Electron and Hole Ionization Rates," IEEE Trans. on Electron Devices, vol. ED-14, No. 6, pp. 313-322, June 1967.
31. Misawa, T., "Negative Resistance in p-n Junctions Under Avalanche Breakdown Conditions, Parts I and II," IEEE Trans. on Electron Devices, vol. ED-13, No. 1, pp. 137-151, January 1966.
32. Schroeder, W. E. and Haddad, G. I., "Nonlinear Properties of IMPATT Devices" (Invited Paper), Proc. IEEE, vol. 61, No. 2, pp. 153-182, February 1973.
33. Lee, C. M., Lomax, R. J. and Haddad, G. I., "Semiconductor Device Simulation" (Invited Paper), IEEE Trans. on Microwave Theory and Techniques, vol. MTT-22, No. 3, pp. 160-177, March 1974.

34. Gilden, M. and Hines, M. E., "Electronic Tuning Effects in the Read Microwave Avalanche Diode," IEEE Trans. on Electron Devices, vol. ED-13, No. 1, pp. 169-175, January 1966.
35. Evans, W. J. and Haddad, G. I., "A Large-Signal Analysis of IMPATT Diodes," IEEE Trans. on Electron Devices, vol. ED-15, No. 10, pp. 708-717, October 1968.
36. Greiling, P. T. and Haddad, G. I., "Effect of Nonsaturated Drift Velocity on Avalanche-Diode Performance," Presented at the 1968 IEEE Int. Electron Devices Meeting, Washington, DC, October 1968.
37. Scharfetter, D. L. and Gummel, H. K., "Large-Signal Analysis of a Silicon Read Diode Oscillator," IEEE Trans. on Electron Devices, vol. ED-16, No. 1, pp. 64-77, January 1969.
38. Blakey, P. A., Giblin, R. A. and Seeds, A. J., "Large-Signal Time Domain Modeling of Avalanche Diodes," IEEE Trans. on Electron Devices, vol. ED-26, No. 11, pp. 1718-1728, November 1979.
39. Dombia, I., Salmer, G. and Constant, E., "High-Frequency Limitation on Silicon IMPATT Diode: Velocity Modulation," J. of Applied Physics, vol. 46, No. 4, pp. 1831-1833, April 1975.
40. Lippens, D. and Constant, E., "Effect of Energy Relaxation on Injected Current Pulse in High Frequency IMPATT Diodes," Electronics Letters, vol. 17, No. 23, pp. 878-879, 12 November 1981.
41. Kafka, H. J. and Hess, K., "A Carrier Temperature Model Simulation of a Double-Drift IMPATT Diode," IEEE Trans. on Electron Devices, vol. ED-28, No. 7, pp. 831-834, July 1981.
42. Blakey, P. A., East, J. R. and Haddad, G. I., VLSI Electronics: Microstructure Science, Einspruch, N. G. (Ed.), Academic Press, Inc., New York, 1981.
43. Butcher, P. N., "Basic Electron Transport Theory," Electrons in Crystalline Solids, International Atomic Energy Agency, Vienna, 1973.
44. Rees, H. D., "Calculation of Distribution Functions by Exploiting the Stability of the Steady State," J. of Physics and Chemistry of Solids, vol. 30, pp. 643-655, 1969.
45. Duderstadt, J. J. and Martin W. R., Transport Theory, John Wiley and Sons, Inc., New York, 1979.
46. Blakey, P. A. and East, J. R., "Improved Modeling of GaAs IMPATTs," Proc. Seventh Biennial Cornell Electrical Engineering Conf., Ithaca, NY, pp. 423-428, August 1979.

47. Blotekjaer, K., "Transport Equations for Electrons in Two-Valley Semiconductors," IEEE Trans. on Electron Devices, vol. ED-17, No. 1, pp. 38-47, January 1970.
48. Huang, K., Statistical Mechanics, John Wiley and Sons, Inc., New York, 1963.
49. Roache, P. J., Computational Fluid Dynamics, Hermosa Publishers, Albuquerque, NM, 1972.
50. Potter, D., Computational Physics, John Wiley and Sons, Inc., New York, 1973.
51. Bosch, R. and Thim, H. W., "Computer Simulation of Transferred Electron Devices Using the Displaced Maxwellian Approach," IEEE Trans. on Electron Devices, vol. ED-21, No. 1, pp. 16-25, January 1974.
52. Robbins, D. J., "Aspects of the Theory of IMPACT Ionization in Semiconductors (I)," Physica Status Solidi(b), vol. 97, No. 1, pp. 9-50, January 1980.
53. Robbins, D. J., "Aspects of the Theory of IMPACT Ionization in Semiconductors (II)," Physica Status Solidi (b), vol. 97, No. 2, pp. 387-407, February 1980.
54. Robbins, D. J., "Aspects of the Theory of IMPACT Ionization in Semiconductors (III)," Physica Status Solidi (b), vol. 98, No. 1, pp. 11-36, March 1980.
55. Nag, B. R., Theory of Electrical Transport in Semiconductors, Pergamon Press, New York, 1972.
56. Blotekjaer, K. and Lunde, E. B., "Collision Integrals for Displaced Maxwellian Distributions," Physica Status Solidi, vol. 35, pp. 581-592, 1969.
57. Wolff, P. A., "Theory of Electron Multiplication in Silicon and Germanium," Physical Review, vol. 95, No. 6, pp. 1415-1420, 15 September 1954.
58. Sze, S. M., Physics of Semiconductor Devices, John Wiley and Sons, Inc., New York 1969.
59. Baraff, G. A., "Distribution Functions and Ionization Rates for Hot Electrons in Semiconductors," Phys. Rev., vol. 128, No. 6, pp. 2507-2517, 15 December 1962.
60. Keldysh, L. V., "Concerning the Theory of Impact Ionization in Semiconductors," Soviet Physics JETP, vol. 21, No. 6, pp. 1135-1144, December 1965.

61. Froelich, R. K. and Blakey, P. A., "Energy and Momentum Conserving Simulation of Millimeter-Wave IMPATT Diodes," Proc. NASECODE II Conf., pp. 208-212, Boole Press, Dublin, 1981.
62. Blakey, P. A., Froelich, R. K., Grondin, R. O., Mains, R. K. and Haddad, G. I., "Millimeter-Wave IMPATT Diode Modeling," Proc. Eighth Biennial Cornell Electrical Engineering Conf., Ithaca, NY, pp. 361-370, August 1981.
63. Shur, M., "Influence of Nonuniform Field Distribution on Frequency Limits of GaAs Field Effect Transistors," Electronics Letters, vol. 12, No. 23, pp. 615-616, 11 November 1976.
64. Bauhahn, P. E. and Haddad, G. I., "IMPATT Device Simulation and Properties," IEEE Trans. on Electron Devices, vol. ED-24, No. 6, pp. 634-642, June 1977.
65. Lax, P. D., "Weak Solutions of Nonlinear Hyperbolic Equations and Their Numerical Computation," Communications on Pure and Applied Mathematics, vol. 7, pp. 159-193, 1954.
66. Lax, P. D. and Wendroff, B., "Difference Schemes with High Order Accuracy for Solving Hyperbolic Equations," Communications on Pure and Applied Mathematics, vol. 17, pp. 381-398, August 1964.
67. Richtmyer, R. D., "A Survey of Difference Methods for Nonsteady Fluid Dynamics," NCAR Technical Note 63-2, Boulder, CO, 1963.
68. Burstein, S. Z., "Finite Difference Calculations for Hydrodynamic Flows Containing Discontinuities," J. of Computational Physics, vol. 2, pp. 198-222, 1967.
69. Richtmyer, R. D., Difference Methods for Initial-Value Problems, Interscience Publishers, New York, 1957.
70. Polezhaev, V. I., "Numerical Solution of the System of One-Dimensional Unsteady Navier-Stokes Equations for a Compressible Gas," Izv. AN SSSR. Mekhanika Zhidkosti i Gaza, vol. 1, No. 6, pp. 34-44, 1966.
71. Evans, W. J. and Scharfetter, D. L., "Characterization of Avalanche Diode TRAPATT Oscillators," IEEE Trans. on Electron Devices, vol. ED-17, No. 5, pp. 397-404, May 1970.
72. Brazil, T. J. and Scanlon, S. O., "Self-Consistent Solutions for IMPATT Diode Networks," IEEE Trans. on Microwave Theory and Techniques, vol. MTT-29, No. 1, pp. 26-32, January 1981.

73. Brackett, C. A., "The Elimination of Tuning-Induced Burnout and Bias Circuit Oscillations in IMPATT Oscillators," Bell System Tech. J., vol. 52, No. 2, pp. 271-306, March 1973.
74. Carroll, J. E., Physical Models for Semiconductor Devices, Crane, Russack and Co., New York, 1974.
75. Millman, J. and Halkias, C., Integrated Electronics: Analog and Digital Circuits and Systems, McGraw-Hill Book Co., Inc., New York, 1972.
76. Rosen, A., Caulton, M., Stabile, P., Gombar, A., Janton, W., Wu, C., Corboy, J. and Magee, C., "Millimeter-Wave Device Technology," IEEE Trans. on Microwave Theory and Techniques, vol. MTT-30, No. 47, pp. 47-55, January 1982.
77. Grondin, R. O., Blakey, P. A., East, J. R. and Rothman, E. D., "Monte Carlo Estimation of Hot Carrier Noise at Millimeter- and Submillimeter-Wave Frequencies," IEEE Trans. on Electron Devices, vol. ED-28, No. 8, pp. 914-923, August 1981.
78. Jacoboni, C., Canali, C., Ottaviani, G. and Quaranta, A., "A Review of Some Charge Transport Properties of Silicon," Solid State Electronics, vol. 20, No. 2, pp. 77-89, February 1977.
79. Barker, J. R., "Quantum Transport Theory," Physics of Nonlinear Transport in Semiconductors, Plenum Press, New York, 1979.
80. Hockney, R. W. and Eastwood, J. W., Computer Simulation Using Particles, McGraw-Hill Book Co., Inc., New York, 1981.
81. Jones, D. and Rees, H. D., "A Reappraisal of Instabilities Due to the Transferred Electron Effect," J. of Physics C., vol. 6, p. 1781-1793, 24 May 1973.
82. Shur, M. S. and Eastman, L. F., "Ballistic Transport in Semiconductor at Low Temperatures for Low-Power High-Speed Logic," IEEE Trans. on Electron Devices, vol. ED-26, No. 11, pp. 1677-1683, November 1979.
83. Board, K., Chandra, A., Wood, C., Judaprawa, S. and Eastman, L., "Characteristics of Planar Doped FET Structures," IEEE Trans. on Electron Devices, vol. ED-28, No. 5, pp. 505-510, May 1981.
84. Grant, W. N., "Electron and Hole Ionization Rates in Silicon at High Electric Fields," Solid State Electronics, vol. 16, No. 10, pp. 1189-1203, October 1973.

DATE
ILMEI